STRANGE PARTICLE PRODUCTION IN PROTON-ANTIPROTON COLLISIONS AT CENTER-OF-MASS ENERGIES OF 630 GeV AND 1800 GeV

A Thesis

Submitted to the Faculty

of

Purdue University

by

Martin Henry Schub

In Partial Fulfillment of the

Requirements for the Degree

of

Doctor of Philosophy

August 1989

ACKNOWLEDGEMENTS

This study involved the resources of the world's highest-energy accelerator and one of the most advanced particle detectors in the world, and was supported in part by the U.S. Department of Energy under contract DE-AC02-76ER01428. It took the hard work of the rest of the CDF Collaboration and the staff of the Fermilab Accelerator Division to make the 1987 Tevatron Collider run a success. I personally am heavily indebted to many CDF collaborators for advice and education, and if I have left anybody's name out (CDF Collaborator or otherwise), I am deeply sorry. Virgil Barnes, Franco Bedeschi, and Adam Para spent many hours reviewing the analysis at every stage, taught me a lot, and kept me from making a fool of myself more than once. Aesook Byon graciously contributed useful advice and software, as well as her laboriously-prepared data summary tapes. Larry Gladney and Tim Rohaly, as well as Franco Bedeschi, were in large part responsible for the development of the vertex-finding software. Andy Beretvas, Peter Berge, Dino Goulianos, Bob Kephart, Jim Bensinger, and Jimmy Proudfoot reviewed the analysis and kept me honest. Charlie Allen gave me the LATEX document format that minimized the hassle of typesetting this thing. Carol Picciolo and Florence Sherter at Fermilab and Sandy Formica and Russ Coverdale at Purdue were of great help in administrative matters. Thanks are also due to Anne Bertram, the sanity-maintenance comittee, for helping me to keep it all in perspective.

TABLE OF CONTENTS

Page

Page

LIST OF TABLES

Table Page

LIST OF FIGURES

Figure | Page

Figure Page

Appendix
Figure **Page**

ABSTRACT

Schub, Martin Henry. Ph.D., Purdue University, August 1989. Strange Particle Production in Proton-Antiproton Collisions at Center-of-Mass Energies of 630 GeV and 1800 GeV. Major Professor: Virgil Barnes.

The inclusive production of the strange particles K_s^0 and Λ has been studied in proton-antiproton collisions at $\sqrt{s} = 630$ GeV and $\sqrt{s} = 1800$ GeV. The inclusive invariant cross-sections, as functions of transverse momentum (p_T), are presented for their production in minimum-bias events. The ratio, as a function of p_T, of the cross-section for K_s^0 to that for charged hadrons is very similar to what is observed at lower energies. At 1800 GeV, we estimate the strangeness-suppression factor $\lambda = 0.38 \pm 0.06$.

1. INTRODUCTION

In our present understanding of nature, matter is made up of elementary particles, which interact via four fundamental forces. Two of these forces, the gravitational and electromagnetic forces, are familiar from everyday experience. The other two, known as the "strong force" and the "weak force", are less familiar. Unlike the gravitational and electromagnetic forces, which can affect matter separated by any distance, the strong and weak forces are important only when particles are separated by extremely small distances–the strong force acts over distances of the order of the size of an atomic nucleus, while the weak force acts over distances a thousand times smaller than that. It is a law of nature that the energies required to study a given interaction become higher as the distance scale over which the interaction occurs becomes smaller. The easiest way to generate large numbers of high-energy interactions for study is to accelerate particles to high energies and collide them with either a stationary target or another beam of high energy particles. This work is a study of head-on collisions of protons with antiprotons.

In most proton-antiproton ($p\bar{p}$) collisions, most of what happens is governed by the strong force. Unfortunately, the theory of the strong force, Quantum Chromodynamics (QCD), is easy to apply only for the most violent collisions, which are also the rarest. In this work, on the other hand, we are concerned with the production of particles in all events, not just the dramatic rare ones. In later chapters,

we compare our measurements to the simplest "perturbative" QCD calculations, in order to get an interesting indication of how well perturbative QCD does near the limits of its applicable range.

Protons and antiprotons belong to a class of particles called "hadrons", the only class of particles that feels the strong force. In the present "Standard Model" of particles and forces, hadrons are made of smaller particles called quarks and gluons. There are six "flavors" of quarks. "Strange" particles are hadrons that contain quarks of the so-called "strange" flavor, while protons are made primarily of quarks with the "up" and "down" flavors. Up and down quarks are the lightest quarks, and strange quarks are considerably heavier. In $p\bar{p}$ collisions at comparatively low energies, say, a few Giga-electron-Volts (GeV), strange particles are produced only rarely, because the masses of even the lightest strange particles are of order 0.5 GeV, so there's not very much energy available to produce them. On the other hand, in the collisions studied for this work, the protons and antiprotons each have an energy of 900 GeV, which is far larger than the masses of any known strange or non-strange particles. With so much energy available, we might naively expect that the suppression due to the extra mass of the strange quark would hardly matter, and therefore that strange particles would be produced about as often as non-strange particles. As we shall see, however, we find that strange particles are in fact produced only around 1/10 as often as non-strange ones. In QCD, this effect is not so surprising, since protons are thought to be complex composite objects, made up of quarks and gluons, so that collisions between protons and anti-protons are treated as collisions between quarks and gluons, where each individual quark

or gluon carries only a fraction of the energy of the proton or antiproton. The outgoing quarks and gluons must then convert into physically observable hadrons, in a process called "fragmentation" or "hadronization". The color field of the quarks and gluons produces quark-antiquark and diquark-antidiquark pairs from the vacuum by a quantum-mechanical tunelling process. The extra mass of the strange quark makes it less probable for strange-antistrange pairs to materialize from the vacuum than for up-anti-up pairs, so the extra mass of the strange quark is still capable of suppressing the production of strange particles relative to non-strange ones.

In the following chapters, we first discuss in more detail the Standard Model view of proton-antiproton collisions, then describe the experimental techniques used to detect K_s^0 and Λ particles, the two strange particles that were studied. Finally, we compare our results to the predictions of perturbative QCD and several QCD-based models.

2. THE EXPERIMENTAL APPARATUS

2.1 The Fermilab Tevatron Collider

At the time of this writing, the highest-energy proton-antiproton collisions in the world, with a center-of-mass energy of 1.8 TeV, are produced at the Tevatron Collider at the Fermi National Accelerator Laboratory in Batavia, Illinois, USA. To create $p\bar{p}$ collisions, the Fermilab facility must be able not only to accelerate protons, but also to use high-energy protons to create antiprotons and to collect, store, and accelerate the antiprotons. All this requires a complex of accelerator apparatus, a schematic diagram of which is shown in Fig. 2.1.

$p\bar{p}$ collisions take place inside the Tevatron ring, the last stage of the accelerator. To set up the Tevatron for collisions, it must be filled with a beam of protons and a beam of antiprotons and ramped to an energy of 900 GeV per beam for 1800 GeV c.m. collisions or 315 GeV for 630 GeV collisions. When the Tevatron his reached the operating energy, so-called low-β quadrupole magnets at either end of the CDF detector (and at several other points around the ring) squeeze both beams to a very small transverse size to enhance the probability of collisions. The beams are then left to circulate and collide in the Tevatron for a day or so, by which time the beams in the Tevatron have become somewhat weaker and larger in size, such that the collision rate is low enough to warrant filling the machine again. While the beams are circulating in the Tevatron, other components of the accelerator

complex are making and storing antiprotons for the next day's collisions.

The acceleration of protons begins in a 750 keV Cockroft-Walton electostatic accelerator and continues in a 200 MeV linear accelerator, neither of which are shown in the figure. The protons are then accelerated to 8 GeV in the "Booster" synchrotron ring, part of which is visible at the left of the figure, and are then injected into a 1-km-radius conventional-magnet synchrotron known (for historical reasons) as the Main Ring. The final stage of acceleration is provided by the superconducting-magnet Tevatron ring, which has the same radius as the Main Ring and is located just below the Main Ring in the same tunnel. When the Tevatron is being filled with protons before the start of collisions, the Main Ring accelerates protons to 150 GeV and injects them into the Tevatron, which then accelerates them to the final energy of 900 GeV. During $\bar{p}$ production, however, the Main Ring accelerates protons to 120 GeV, and this beam is extracted from the Main Ring and directed onto a tungsten $\bar{p}$ production target.

A small fraction of the particles produced when the protons hit the $\bar{p}$ production target are antiprotons. A lithium "lens" with high electrical currents passing through it serves as a magnetic lens to focus the $\bar{p}$s and select only the ones with momentum of 8.9 GeV. The focussed $\bar{p}$ beam is fed into the Debuncher ring, where the short $\bar{p}$ bunches are lengthened and stochastic cooling is used to reduce the emittance. Further stochastic cooling is done in the Accumulator, where a large number of antiprotons is accumulated for later use in $p\bar{p}$ collisions. More details of the antiproton production and cooling process may be found in [1].

2.2 The CDF Detector

The Collider Detector at Fermilab (CDF) is a large, azimuthally-symmetric, general-purpose detector. As shown in the isometric view in Fig. 2.2, the axis of symmetry is the Tevatron beam pipe, in which the proton beam and the antiproton beam collide near the center of the central detector.

CDF follows a pattern common in large spectrometers. Particles emerge from the collision into a 1.515 Tesla solenoidal magetic field parallel to the beam axis, which makes the charged particles curve, the radius of curvature being proportional to their momenta transverse to the beam axis, and this curvature is measured by tracking chambers. Particles then hit two layers of calorimeters; electromagnetic shower calorimeters first, then hadronic cascade calorimeters. The calorimeters are stacks of metal (lead for the electromagnetic calorimeters, steel for the hadronic ones) and active material (plastic scintillator in the central calorimeter, gas-filled chambers in the forward/backward calorimeters) that measure the energies of particles by causing them to dump their energy via a shower of secondaries, tertiaries, etc., some of which are seen by the scintillator or chambers. Electons and photons will tend to dump most of their energy in the EM calorimeters, hadrons in the hadron calorimeters. Muons, on the other hand, will usually lose only a little energy (minimum ionization) in the calorimeters and thus pass clear through a calorimeter, something which other types of particles do only rarely. At the back of the central calorimeter there are chambers to detect muons, and beyond the forward calorimeters there are magnetized iron toroids, also designed to detect muons and to measure their momenta. CDF also includes small-angle silicon de-

tectors mounted in the beam pipe some distance from the central detector; these are designed to measure elastic and diffractive $p\bar{p}$ scattering.

A standard coordinate system has been established for CDF. The origin of CDF coordinates is the center of the Central Detector, and the z-axis is the center of the Tevatron beam pipe, with the positive z direction being defined as the direction that protons travel in the Tevatron. The polar angle θ is of course measured from the positive z axis, and we will often have occasion to refer to the pseudo-rapidity $\eta \equiv -\ln\tan(\theta/2)$, an angular variable which approximates the true rapidity y. y is defined in terms of the energy E and longitudinal momentum p_z of a particle, as follows: $y \equiv \frac{1}{2}\ln(E+p_z)/(E-p_z)$, and thus requires that the particle species be know, which is not always possible.

Our study of K^0_s uses only a few of the detector components—two of the tracking chambers (the Vertex Time-Projection Chamber (VTPC) and the Central Tracking Chamber (CTC)) and the Beam-Beam counters (BBC). These components are described below, and we refer the reader to [2] for details of the rest of the detector and further technical information on the components we describe.

2.2.1 The Beam-Beam Counters

The layout of one of the beam-beam counter planes is shown in Fig. 2.3. The BBCs are located at ± 5.82 m from the nominal interaction point, and they cover the pseudorapidity range $3.2 \lesssim |\eta| \lesssim 5.9$. The BBCs are used in the trigger system to quickly decide whether a collision took place, so that the data aquisition system can be told to read out the data from the collision. The trigger for minimum-bias events requires that at least one scintillator in each array be hit by a charged

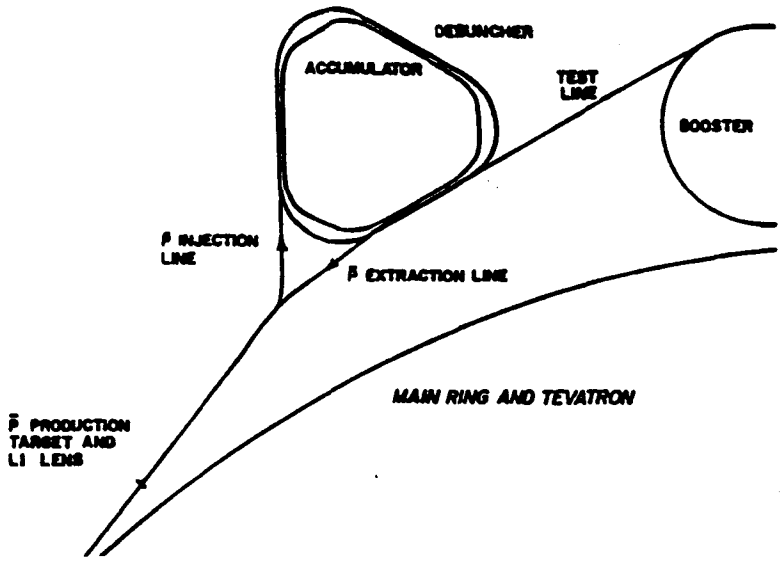

Figure 2.1

The Fermilab Tevatron Collider complex.

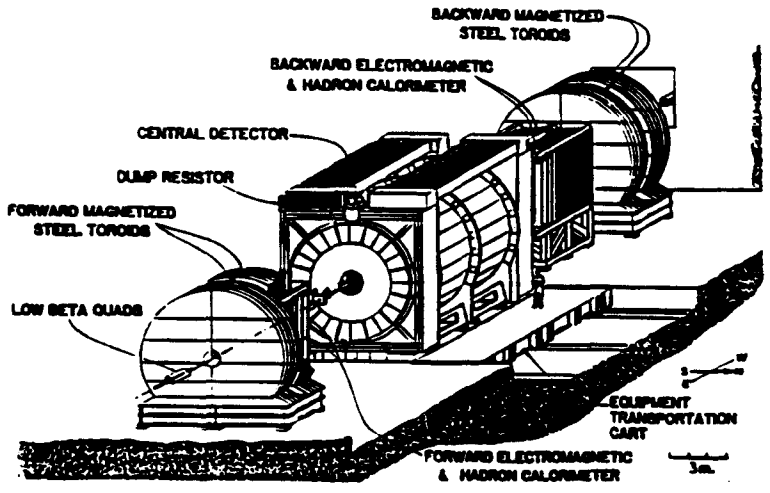

Figure 2.2

Isometric view of CDF.

particle within a 15 ns window centered on the beam crossing time.

2.2.2 The Vertex Time-Projection Chamber

The VTPC system [3] is the innermost CDF tracking device. It consists of eight small time projection chambers mounted end-to-end along the beam pipe. An isometric drawing of two of the modules is shown in Fig. 2.4. Particles emerging from a collision leave trails of ionization in the argon-ethane gas in the VTPC, and the ionization electrons drift under the influence of an electric field toward the ends of the module, where they cause a cascade of further ionization that is collected on the sense wires. Charge is induced on pads on printed circuit material located behind the sense wires, making it possible to tell where along a wire the charge was collected, but during the 1987 run, the pads were read out only on two modules, and this information was not used in our analysis. The sense wires are read out by time-to-digital converters (TDCs), and the timing information, coupled with knowlege of the drift speed of electrons in the gas, tells us, for each wire that was hit, the z coordinate of the track that generated the ionization. These measurements give us a 2-dimensional picture of the track trajectory—one dimension is R, the radial distance from the beam axis, and the other dimension is z. Adjacent modules are rotated with respect to each other by arctan(0.2), so that for tracks which pass through more than one module, we have two projections of the track, allowing us to determine the ϕ (azimuth) of the track as well. However, without the pad information, the VTPC cannot measure the curvatures of tracks and hence the momenta of particles. The VTPC can measure tracks in the range $3 \lesssim \eta \lesssim 3$.

2.2.3 The Central Tracking Chamber

The CTC [4] is a large cylindrical axial-wire drift chamber, with a cylindrical hole in its center that holds the VTPC. The CTC volume is also filled with argon-ethane gas which is ionized by the passage of charged particles, but in this case the wires are arranged such that the chamber volume is divided into a large number of small drift cells arranged in concentric "superlayers". Again, the sense wires are read out by TDCs, and since we know the drift speed of electrons in the gas, the time at which charge reaches reach each wire tell us where a charged particle intersected the drift trajectory, giving us a set of points or "hits" along the track. Because electrons may drift to a sense-wire plane from either side, each hit may be interpreted in two ways. A computer program must resolve this ambiguity and find the sets of hits that belong together to form tracks.

Fig. 2.5 is drawing of one endplate of the CTC. As we proceed radially outward, we see eight concentric rings of oblong holes, one for each superlayer, which hold feedthrough blocks for the wires. The rings containing the longer holes are for axial superlayers, where the wires run parallel to the beam axis, and the others are for "stereo" superlayers, where the wires are tilted 3° with respect to the beam axis. As we see from Fig. 2.5, there are 5 axial superlayers and 4 stereo superlayers. Combining the information from the axial and stereo wires allows us to measure z coordinates along tracks, so tracks can be reconstructed in 3 dimensions. The cells are tilted 45° from radial so that the combination of the electric field in the cell and the magnetic field from the solenoid makes the drift electrons travel roughly azimuthally.

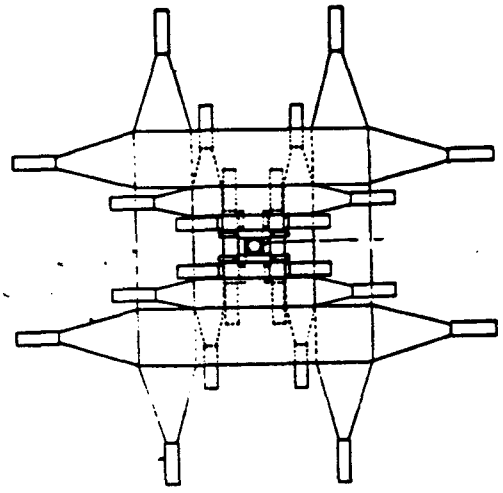

Figure 2.3

A beam's-eye view of one of the beam-beam counter planes.

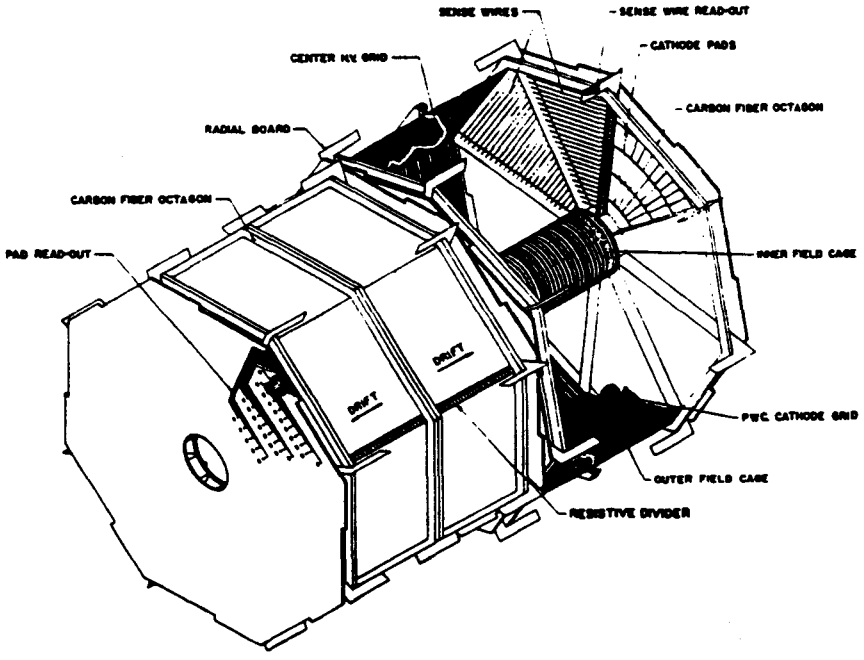

Figure 2.4

Two of the eight VTPC modules.

The arrangement of wires in an axial cell is shown in Fig. 2.6, where the directions of the magnetic field ($\vec{B}$), electric field ($\vec{E}$), and drift velocity ($\vec{v}$) are also shown. Only the 12 sense wires in an axial cell are read out; the rest of the wires are used to shape the electric field to make the drift trajectories as uniform as possible. Stereo cells have only 6 sense wires. The resolution of each wire measurement was 300μm in the 1987 run. The z resolution of each stereo-wire measurement is therefore $300\mu\text{m}/\sin 3^\circ = 5.7$ mm.

Particles will undergo multiple Coulomb scattering in the beam pipe, the Faraday cage surrounding the beam pipe, and the carbon-fiber tube that forms the inner bore of the CTC, and also in the gas and wires in the CTC. The deviations in the track parameters due to multiple scattering depend on the amount of material the particle traverses and the radiation length of the material. The material before the CTC active volume is shown in Fig. 2.7 in fractions of a radiation length vs. θ. In the region of interest, $0 \leq \theta \lesssim 3$, a particle passes through between 5 and 10% of a radiation length before entering the active volume of the CTC.

During the 1987 run, a number of the cells in one of the axial superlayers (superlayer 4, where the innermost superlayer is 0 and the outermost is 8) were dead due to loose wires. Tracks passing through the dead regions were not used in our analysis.

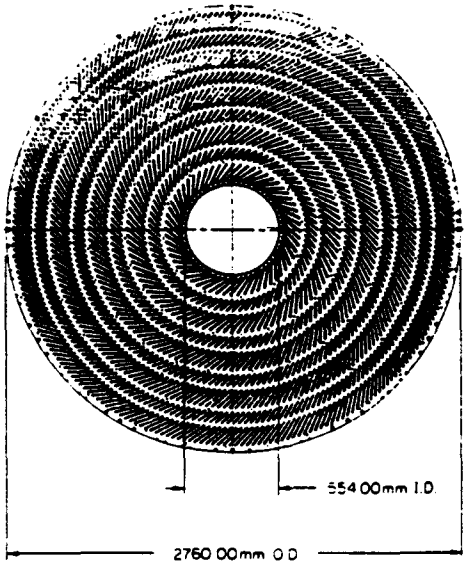

Figure 2.5

One endplate of the CTC.

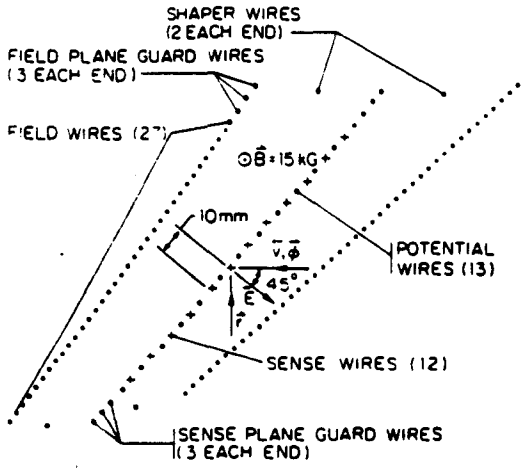

Figure 2.6

Arrangement of wires in an axial cell.

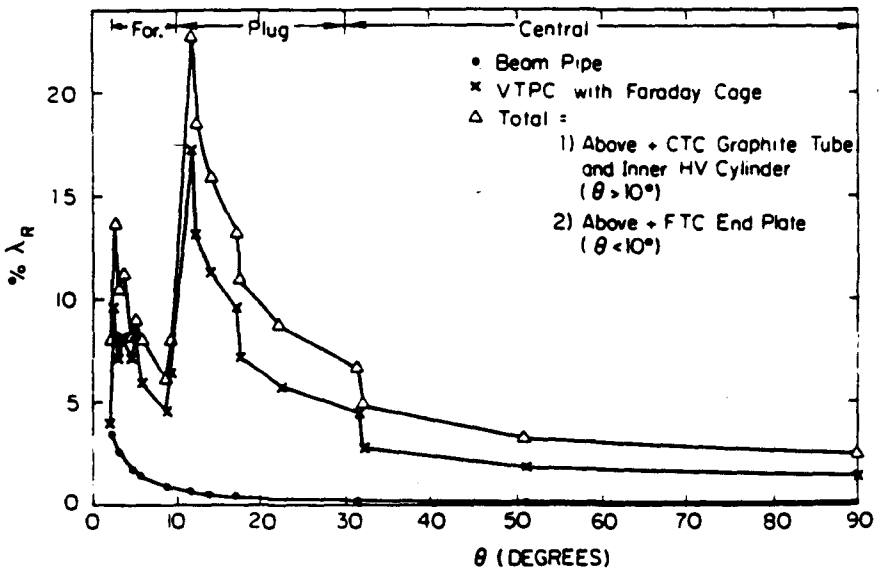

Figure 2.7

Total amount of material between the beam and the CTC vs angle.

3. THE DATA SAMPLES

One would like to be able to study the production of K_s^0 and Λ for all types of $p\bar{p}$ collisions, but this is unfortunately not possible. When a bunch of protons meets a bunch of antiprotons, a proton and and antiproton may collide, or a proton or antiproton may collide with an atom of residual gas in the beam pipe, or both, or neither. Furthermore, $p\bar{p}$ collisions may be divided into several classes, some of which may be unobserved by our detector. The trigger system must decide whether a real collision actually occured.

The classes into which $p\bar{p}$ collisions are conventionally divided are:

1. Elastic Scattering, in which both the proton and the antiproton survive the collision intact, but are scattered through some (typically very small) angle.
2. Single Diffractive, in which either the proton or the antiproton (but not both) survives the collision intact, and a narrow spray of particles is produced opposite the surviving particle.
3. Double Diffractive, which is similar to single diffractive, except that neither beam particle survives, and two narrow sprays of particles are produced in opposite directions near the beam axis
4. Non-Diffractive, where the collision involves substantial momentum transfer, usually resulting in some particles being emitted with substantial momentum transverse to the beam axis (p_T).

Elastic collisions are of no interest to us here because they produce no strange particles. Single and double-diffractive collisions are difficult to detect because it is difficult to reliably distinguish the emitted particles, which are usually quite close to the beam, from the fringes or "halo" of beam particles that surround the dense central portion of the beam. On the other hand, non-diffractive interactions are comparatively easy to detect and have only beam-gas interactions as a background. Because the gas particles in the beam pipe are nearly at rest, the particles produced in a beam-gas collision usually have a lot of momentum in the direction of the beam particle, so usually they are one-sided; that is, almost all the particles come out in one hemisphere ($0 < \theta < 90°$, or $90° < \theta < 180°$). Non-diffractive collisions are typically more isotropic.

The data samples we use here are events that passed a beam-beam counter trigger, that is, events with at least one particle hitting each scintillator array. Requiring that both counters be hit rejects some beam-gas events, because particles from beam-gas collisions typically hit only one set of scintillators. Some beam-gas collisions do in fact generate particles in both hemispheres, so there is still some beam-gas background. At 1800 GeV, we collected 55700 triggers, and at 630 GeV, 9400.

In order to reject beam-gas interactions, additional event selection criteria were imposed in addition to the trigger criteria. These additional cuts use information from the the VTPC track reconstruction and primary vertex finding algorithms, which are described in detail in [5] and [6]. The VTPC acceptance depends on the positions of the $p\bar{p}$ interactions, which follow a Gaussian distribution in z,

centered near the center of the CDF detector, so in order to insure full acceptance of the VTPC in $|\eta| < 3$, we demand that the z coordinate of the primary vertex be within 65 cm of the nominal interaction point. We also demand that the z coordinate of the primary event vertex as calculated using VTPC tracks match the z obtained from BBC timing information to within 16 cm, and that there be at least 4 tracks in the VTPC in $|\eta| < 3$, at least one of which must be in the forward hemisphere and one in the backward hemisphere. A sample of events passing these cuts were inspected by physicists, and the contamination of non-beam-beam events was estimated to be less than 2.5% in the 630 GeV data and less than 0.5% in the 1800 GeV data.

To estimate our acceptances for various components of the total cross-section, studies were done using the Rockefeller Monte-Carlo [7], and the results are shown in Table 3.1. With all of the above cuts applied, we are still 96% (93%) efficient for the non-diffractive portion of the cross-section at 1800 (630) GeV. Our samples are in effect "non-single-diffractive". The estimated effective cross-sections seen by our trigger also appear in Table 3.1.

A problem in the CTC electronics in the 1987 run caused the CTC readout to occasionally be swamped by noise hits at random times, and events where this happened were also rejected. After all event-selection cuts have been performed, our sample contains about 44000 events at 1800 GeV and 3800 at 630 GeV.

Table 3.1

Monte Carlo estimates of our accepted cross sections from various components of the total cross section.

	630 GeV	1800 GeV
Non-diffractive	31.6 ± 3.4 mb	38.6 ± 6.6 mb
Double-diffractive	1.4 ± 0.3 mb	3.4 ± 0.6 mb
Single-diffractive	1.1 ± 0.1 mb	2.4 ± 0.8 mb
σ_{eff}	34 ± 3 mb	43 ± 6 mb

4. RECONSTRUCTION ALGORITHMS

We find K^0_s, Λ and $\bar{\Lambda}$ through the decays $K^0_s \rightarrow \pi^+\pi^-$, $\Lambda \rightarrow p\pi^-$, and $\bar{\Lambda} \rightarrow \bar{p}\pi^+$. These decays are known as "neutral Vees" or "V^0s" because in cloud- and bubble-chamber experiments, the neutral parent particle is invisible and the tracks left by the daughter particles emerge from the decay point in a pattern similar to the letter V. In our experiment, most of the decays occur between the beam-pipe and the inner bore of the CTC. We could in principle look for the decay vertices (the point of the V) in the VTPC, but decays would be difficult to distinguish from Vees formed by tracks that cross near the inner wire layers of the VTPC, pieces of spiralling tracks, etc. Instead, we rely entirely on CTC tracks, extrapolating them to radii smaller than the CTC inner bore to find the decay vertex.

The first step in the analysis, then, is to reconstruct tracks from wire hits in the CTC. We then try to find the decay vertices among pairs of tracks with opposite signs that appear to come from decays; that is, tracks that don't appear to come from the primary event vertex, where most tracks in the event meet. To do this, we must be able to find the transverse position of the beam relative to the center of the CTC, which can be done by reconstructing the primary vertices of a large number of events, and we must be able to find the positions of the decay vertices. The algorithms by which tracks are reconstructed and primary and secondary vertices are found are discussed below.

4.1 CTC Track Finding

Figure 4.1 is an end view of the CTC, showing the positions of CTC hits (dots) from a typical 1800 GeV minimum-bias event. The CTC track-finding algorithm is designed to associate sets of these hits to form tracks. In the figure, the arcs drawn on top of the dots are the xy projections of tracks found in this event by Version 4.3 of the CTC tracking algorithm, the version used for this analysis. There are many places in the figure where X-shaped patterns of hits may be seen—these are places where tracks cross sense-wire planes in the centers of drift cells, and only one of the crossed lines corresponds to the actual path of the track, while the other is caused by the ambiguity of drift sign discussed above. The tracking algorithm begins by looking for these X-shaped patterns in the outermost superlayers, and uses them to define "roads" in which to look for additional hits. We will describe the algorithm in more detail shortly, but first we will introduce some necessary nomenclature.

4.1.1 Helix Parameters

The trajectory of a charged particle in a uniform magnetic field is in general a helix whose axis is along the field direction, which in CDF is parallel to the beam axis. Projected on a plan transverse to the magnetic field, then, a CTC track looks like an arc or a circle, while projected in a plane containing the beam axis, it looks like a sinusoid. In the absence of measurement or pattern-recognition errors, the circle will pass through the beam axis for tracks that come directly from the $p\bar{p}$ collision, while tracks coming from decays will in general miss the beam axis.

In order to completely specify a helix, we need five parameters. These are

conventionally taken as follows:

1. c, the signed half-curvature. The sign of c is the sign of the charge of the particle, and the magnitude of c is $1/(2R)$, where R is the radius of the projected circle.
2. d, the impact parameter, or distance of closest approach. There is a sign convention for d also—when the origin is inside the projected circle d has the same sign as c, while when the origin is outside d and c have opposite signs.
3. ϕ_0, the angle, in the xy (transverse) projection, that the track makes with respect to the positive x axis at its point of closest approach to the beam axis.
4. z_0, the z coordinate of the track at closest approach to the beam axis.
5. $\cot\theta$, the cotangent of the dip angle of the track.

4.1.2 The Pattern-Recognition Algorithm

The program that finds CTC tracks begins by finding circles in the transverse plane using information from the axial wires, then uses the circles that it finds to find corresponding hits in the stereo layers to complete the 3-dimensional track. Because tracks are generally well-spaced at the outermost superlayer, the program begins by searching for track segments in individual drift cells in this superlayer. The program requires that cell segments consist of at least 5 hits and must pass through the sense-wire plane of the cell (which means, incidentally, that the track can have turned only $30 - 40°$ between the time it left the primary vertex and the time it created the hits in the segment). The program then attempts to extend the segment into neighboring cells, by comparing hits in the neighbor cells with the

position where hits ought to be on each wire, based on the original cell segment. If a total of eight hits can be found whose residuals from a straight-line fit are all less than 500 μm, the segment is used as a seed to search for other hits on the track. Otherwise, the program moves on to looking for segments in other cells, and eventually, the next superlayer. The program gives up trying to find tracks when it reaches superlayer zero, the innermost superlayer.

A circle, constrained to pass through the beam position, is now fit to the straight-line segment. A search is performed for additional hits on the track, proceeding inward toward the beam (and outward also, if the starting segment was found in some other superlayer than 8). In each layer, we add to the track the closest hit to the fitted circle within a 2 mm "road" about the circle. The program stops trying to add hits to the track when it encounters 3 wire layers between the original segment and the beam in which it was unable to find acceptable hits. When the hit search is finished, another circle fit is performed, using all the hits. The circle is then refined by rejecting some of the hits— the fit residuals of the best 3/4 of the hits are averaged, and remaining hits are removed from the track if their residuals are worse than about 3 times this average, and a circle fit, again with the beam constraint, is performed on all surviving hits. If, after hit rejection, the program was able to find at least 20 acceptable hits, but it not able to find any hits below superlayer 3, another fit is performed without the beam constraint and is used to define another road, the search for additional hits is performed again using the new road, and fitting and hit rejection are done again.

Now that the program has a good transverse view of the track from the axial

hits, it looks for hits in the stereo layers. First, a road must be defined in which to search. The stereo hits that in $R - \phi$ projection are closest to the previously fitted circle are used, along with the z of the primary vertex as found by the VTPC vertex-finder [6] [5] are used to find trial values of z_0 and $\cot\theta$, which define the road. Stereo hits lying within 1.5 mm of the trial track trajectory are added to the track, a 3-dimensional helix fit is performed, and again hits with large residuals are rejected. The final helix fit gives us the five helix parameters and their complete covariance matrix.

4.2 Primary and Secondary Vertex-Finding Algorithms

We have at our disposal two vertex-fitting algorithms (described in the next subsection), which are used both in finding the primary vertices of events and in finding the decay vertices of K^0_s and Λ candidates. Each algorithm takes as input a starting approximation of the vertex position, plus the helix parameters and errors for some set of CTC tracks, and produces a better approximation of the vertex position. We will first describe the two fitting algorithms, then the algorithm we use to find the primary event vertex.

4.2.1 Vertexing Fitting Algorithms

The simpler of the two vertex-fitting algorithms, which we'll call VSFIT0, estimates the point of intersection based on the track parameters and their errors, and does not change or "steer" the parameters to force the tracks to actually intersect in space. Tracks are approximated by straight lines near the supposed vertex, and the algorithm attempts to find the point which has the smallest r.m.s. weighted

distance from the lines. This algorithm is described in [8], details of the software specification for the routine that implements it are found in [9], and details of the track-expansion calculations which form the input to this algorithm are discussed in [10].

In the second algorithm, called VSFIT1, the track helix parameters are allowed to vary about their measured values. This algorithm produces an improved estimate of the vertex point and also a set of helix parameters for each track which have been adjusted ("steered") such that the track passes through the improved vertex point exactly. The algorithm used is described in [11], the specification in [9], and the expansion calculations in [10]. Both algorithms return a χ^2which may be used to test the quality of the fit.

4.2.2 Primary Vertex Finding Algorithm

To find the primary vertex of an event, we select all CTC tracks with impact parameters less than 3 mm and $p_T > 0.4$ GeV, and we use the VSFIT0 algorithm to improve the vertex position. The improved vertex position is then used as a starting point for the VSFIT1 algorithm, which again fits the vertex with the same set of tracks. At this point, any tracks that contribute extremely anamolously high fractions ($> 40\%$) of the χ^2 of the fit are subtracted from the fit. If the final χ^2 of the fit is less than 5 per degree of freedom, the fit is accepted and the final vertex coordinates are taken as the coordinates of the primary vertex of the event.

Figures 4.2 and 4.3 are distributions of the x and y positions of primary event vertices for around 7500 minimum-bias events. The mean values of $< x >= -0.03845$ cm and $< y >= -0.01246$ cm are consistent with values obtained by

Adam Para based on the azimuthal variation of the mean impact parameter of CTC tracks. The standard deviations are about 0.0750 cm. For comparison, the transverse size of the beam is around 75 μm. Figure 4.4 is a distribution of difference between the z of the primary vertex as found by the CTC primary vertex algorithm and the z found by the VTPC primary vertex algorithm. The mean is -0.12 cm, indicating a slight misalignment between the VTPC and CTC, and the standard deviation is 0.68 cm, which is of the order of the z resolutions of both the CTC and the VTPC.

Since our transverse position resolution on the primary vertex is the better part of a millimeter, and since not all events have enough well-measured tracks for the algorithm to successfully find a primary vertex, in the K^0_s and Λ analysis we assume that the vertex position remains fixed in xy at the positions noted above, and we take the z coordinate for each event to be the VTPC vertex z minus the 0.12 cm offset between the VTPC and CTC noted above.

4.2.3 Secondary Vertex Finding Algorithm

In finding the position of the primary vertex, the origin of the coordinate system is fairly close to the final answer and therefore is a fairly good starting point for the fits, and two iterations of fitting are usually sufficient. For secondary vertices, however, the primary event vertex usually is not such a good starting point, so several iterations are required to converge on the vertex position. Protections must be applied to prevent the process from diverging, oscillating, or, for that matter, infinite-looping. We will first describe the vertex-finding algorithm, and then present some results on the performance of the algorithm on simluated K^0_s.

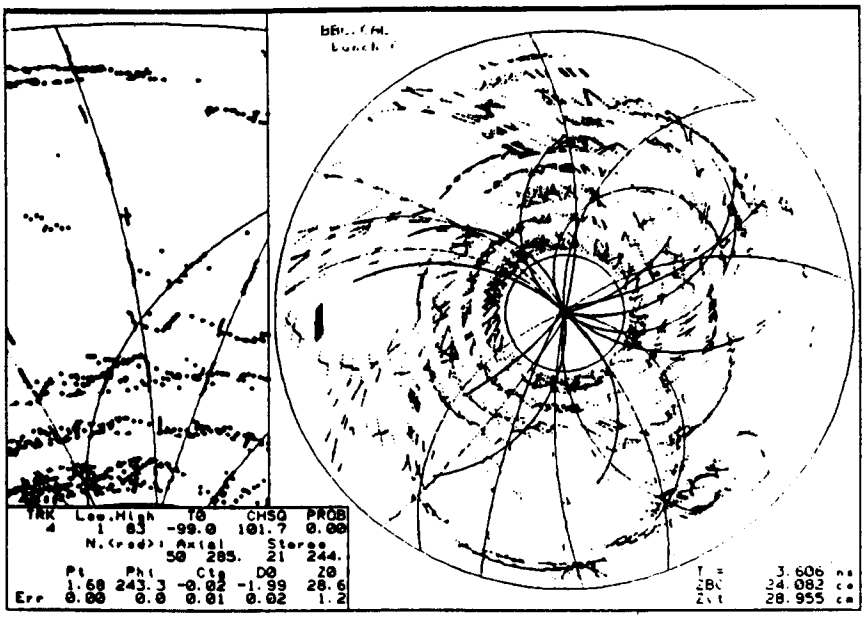

Figure 4.1

End view of CTC showing hits and tracks for a typical min-bias event.

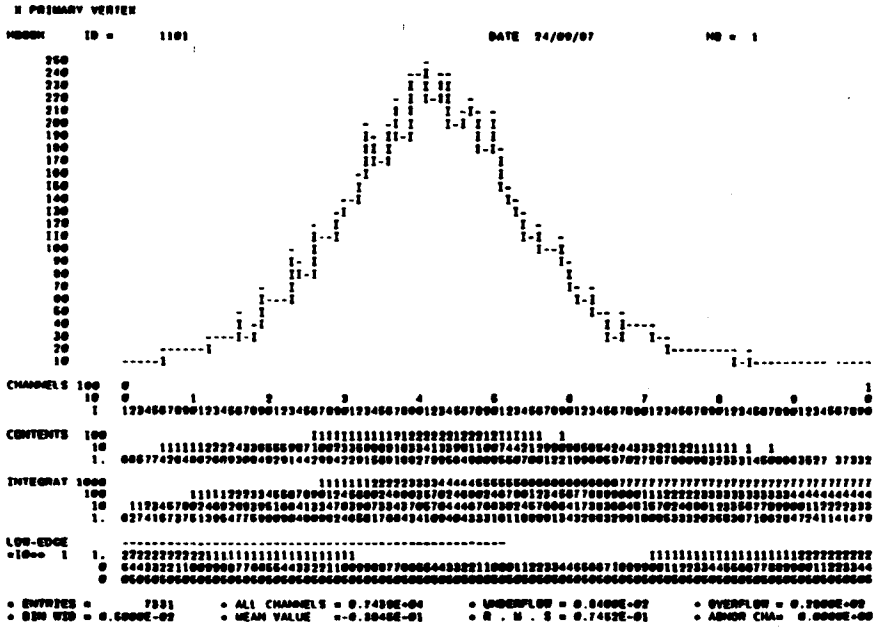

Figure 4.2

Distribution of x of primary event vertex for about 7500 min-bias events.

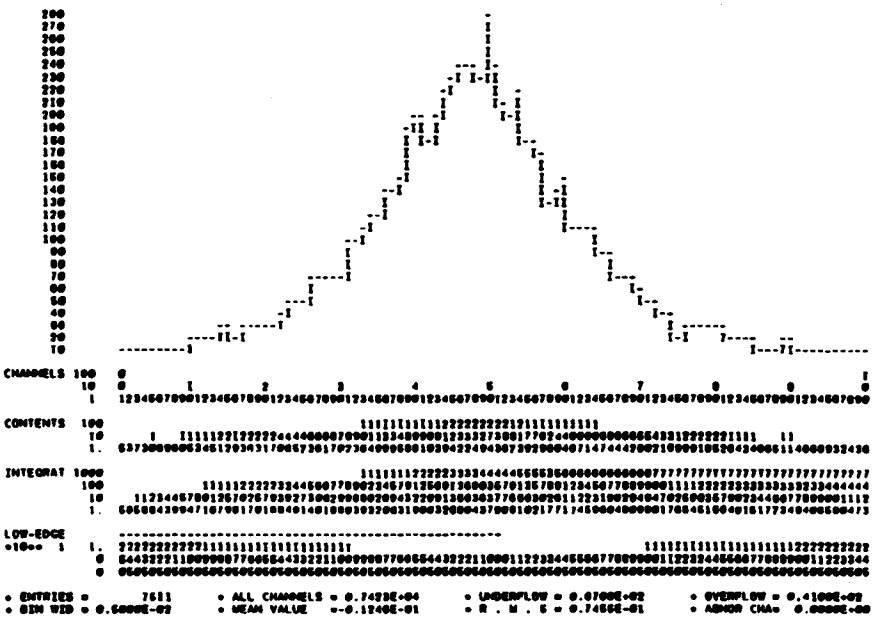

Figure 4.3

Distribution of y of primary event vertex for about 7500 min-bias events.

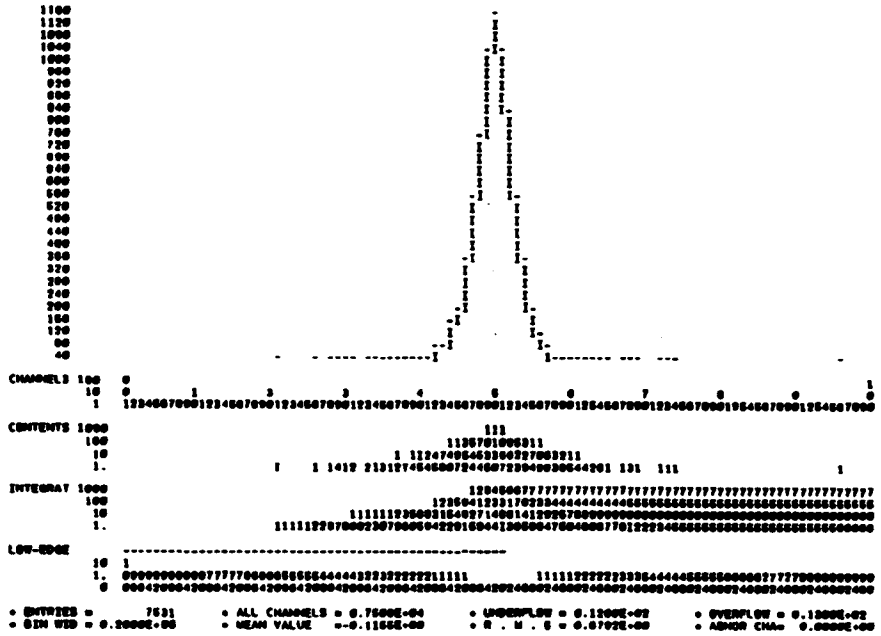

Figure 4.4

z of the primary vertex from VTPC algorithm minus z from CTC algorithm.

The actual flow of control in the vertex-finding algorithm is somewhat complicated, because numerous checks are performed during the iteration process to insure that the fit isn't diverging or oscillating, and that the number of iterations is finite. The full structure is perhaps best presented in pseudo-code, which appears in Appendix A. In general terms, the technique used is to iterate over the simple non-steering fit (VSFIT0), refining the vertex point with each iteration, and then, if the process has converged and the fit quality is sufficiently good, a steering fit (VSFIT1) is performed and its quality checked. If the quality of this final fit is good enough (χ^2/degree of freedom less than 5.0), the vertex is considered acceptable.

4.2.4 Performance of the Secondary Vertex Finding Algorithm

In order to gauge the performance of the vertexing algorithm on K^0_s, a sample of K^0_s was generated with a spectrum matching that of the (at the time) latest version of the CDF K^0_s spectrum, and reconstructed with version 4.3 CTC tracking and the vertexing algorithm described. The found vertex radius for each K^0_s was compared with the "true" radius obtained from internal simulation information and the difference was histogrammed (see figure 4.5), and the distance between tracks at the vertex (ideally 0) was also histogrammed (see figure 4.6). The bin width in the radius-of-vertex plot is 0.4 cm; in the distance-of-closest-approach plot it's 0.1 cm. The r.m.s. deviation from the true vertex radius is 0.78 cm, and the average distance between tracks at the vertex is 0.82 cm, which is of the same order as the assumed z resolution of the CTC.

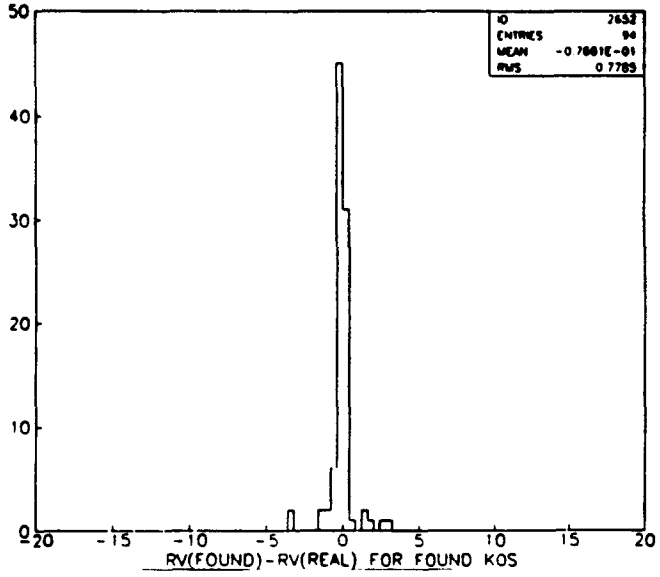

Figure 4.5

Found Vertex Radius Minus True Vertex Radius (in cm) for simulated K_s^0 decays.

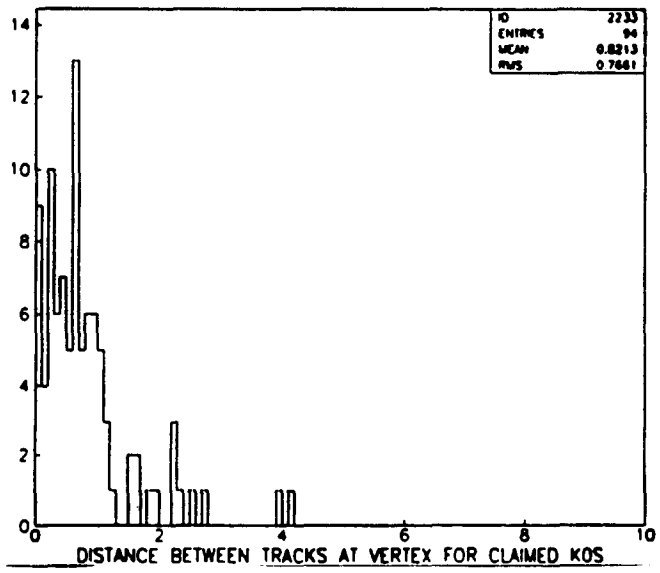

Figure 4.6

Distance of closest approach (in cm) between tracks at the vertex for simulated K_s^0 decays.

5. FINDING K_s^0, Λ, AND $\bar{\Lambda}$ CANDIDATES

In the last chapter, we described the beginnings of the data reduction process—CTC track finding and the location of the primary vertex. The remaining steps in the process of generating and fitting p_T spectra for K_s^0 and $\Lambda/\bar{\Lambda}$ are described in this chapter, including finding the decay vertices, imposing and tuning cuts to purify the samples of decays, evaluating efficiencies, and subtracting the contribution of the background. Comparison of the spectra with QCD predictions and Monte-Carlo models and extrapolations of the spectra are described in later chapters.

5.1 Finding K_s^0 and Λ Decay Vertices

As we have mentioned, the decay daughters of the charged decay modes of K_s^0 and $\Lambda/\bar{\Lambda}$ typically have finite impact parameters, which allows us to distinguish them from well-measured primary tracks, and the daughter particles always have oppositely-signed charges. Furthermore, the efficiency of the CTC track-finding algorithm is very low below $p_T = 250$ MeV. In order to ensure that the tracks are of good quality, it is also useful to require that at least half of the number of hits that could be used on each track, given its measured helix parameters, must have been used in the final fit done by the CTC tracking algorithm. Therefore, to find decays of K_s^0 and $\Lambda/\bar{\Lambda}$, we used our secondary-vertex-finding algorithm to look for vertices among all pairs of tracks having opposite signs, p_T for each track greater than 250 MeV, impact parameter (with respect to the primary vertex) of

greater than 0.2 cm, and at least half the possible hits used. Vertices were deemed acceptable if the χ^2 per degree of freedom (N_{dof}) of the final vertex fit was less than 5.

In Figure 5.1, we have assigned pion masses to each track of all such pairs in the 1800 GeV data for which acceptable vertices were found, and histogrammed the invariant mass. There is an obvious peak at the K_s^0 mass, but there is also a very substantial background, which is very likely composed of pairs of primary tracks whose impact parameters were badly mismeasured. Mismeasurement may be due either to pattern-recognition errors (mis-associated hits) or to imperfections in the relatively primitive drift model and drift constants used in Version 4.3 of the tracking algorithm. Clearly, in order to get a reasonable signal-to-noise ratio, we must impose some cuts.

A number of possibilities suggested themselves. First, we could demand that the tracks have even larger impact parameters than the 0.2 cm cut we had already applied, or demand that they have greater p_T than we were already demanding. Second, it was found that most of the background pairs seemed to have vertices close to the beam axis, constistent with the hypothesis that they were in fact composed of primary tracks—this suggested a cut on the transverse radius of the vertex point. Further, one would expect that real K_s^0 would have momenta that pointed back to the primary vertex, while random background in general would not.

A program was written to optimize the cut values. Using the real data as input, this program looped over a large number of combinations of cut values, covering the

entire reasonable range of values for each cut. For each combination, the program counted the total number of pairs whose invariant mass was near the K^0_s mass, and counted the number of pairs whose invariant mass fell in two background windows flanking the K^0_s peak. It then calculated the statistical significance of the net background-subtracted K^0_s signal, which was found to vary rather little over the range of cuts considered.

The number of K^0_s candidates above background varied between about 100 and 500, while the signal-to-noise ratio varied from around 10-to-1 to around 3-to-1. We finally settled on a set of cuts that had neither the best signal-to-noise ratio nor the best net signal, but had reasonably good values of both, and, for reasons discussed below, did not lie in regions where one has to worry about the effects of differences between the CDF simulation and the real data. K^0_S and $\Lambda/\bar{\Lambda}$ candidates were now required to have decay vertices at least 2 cm from the beam axis, and impact parameters of each candidate track pair were required to have impact parameters of at most 2 cm, where this impact parameter is defined as the distance of closest approach to the primary vertex of a line passing through the decay vertex in a direction opposite to the total 3-momentum of the pair (this is the "pointing" cut).

In summary, the cuts used to define K^0_s and Λ candidates are:

- The impact parameter of each track must be greater than 2 mm.
- The transverse momentum of each track must be at least 250 MeV.
- At least half of the number of hits that could be used on each track, given its measured helix parameters, must have been used in the final fit done by

the CTC tracking algorithm.

- The vertex-fit χ^2 must be less than 5.
- The transverse radius of the vertex formed by the tracks must be at least 2.0 cm.
- The total momentum of the pair must point back to the primary vertex to within 2.0 cm in 3-space.
- For simulated K^0_s, the reconstructed invariant mass calculated with a $\pi - \pi$ mass hypothesis must be between 0.470071 and 0.525271 GeV/c^2. For simulated Λ and $\bar{\Lambda}$, the reconstructed $p\pi$-hypothesis mass must be between 1.1072 and 1.124 GeV/c^2.
- The rapidity of the K^0_s, Λ and $\bar{\Lambda}$ candidates must be between -1 and 1.

Figure 5.2 shows the $\pi - \pi$-assignment mass distribution near the K^0_s mass for all track pairs in the 1800 GeV data which passed all the cuts. The solid curve is the result of a fit to a Gaussian plus a linear background. The fitted mean of the Gaussian is 0.4986 GeVc^2 (compared to the handbook K^0_s mass [12] of 0.497671 GeV/c^2), and the σ is 0.0092 GeV/c^2. If we look within 3σ of the handbook K^0_s mass, there are about 450 track pairs in the peak above a background of about 100. In the 630 GeV data, there are 27 K^0_s candidates and about 11 background pairs under the peak.

Fig. 5.3 shows the mass distribution near the Λ mass, where a proton mass has been assigned to one track and a charged-pion mass to the other. The solid line is again a fit to a Gaussian plus a linear background, and this time the mean is 1.1146 GeV/c^2 (compared to the handbook mass of 1.11563 GeV/c^2), and the σ is 0.0028

GeV/c^2. If we look within 3σ of the handbook mass, there are 68 track pairs in the peak above a background of 8. Of the 76 track pairs in the peak, including both the signal and the background, 39 are consistent with being $\bar{\Lambda}$ and 37 are consistent with being Λ. If there were any $\Lambda/\bar{\Lambda}$ ambiguity, it would be possible for some track pairs to enter the histogram twice, but we have checked that all pairs that fall anywhere near the Λ mass with the first particle being assigned the proton mass will fall very far from the Λ mass if the first particle is assigned a pion mass, and vice-versa. There is too little 630 GeV data to find enough Λ candidates to do physics with.

We impose cuts on the reconstructed invariant mass in order to determine which events are treated as K^0_s or Λ candidates and which are to be used for background-estimation. K^0_s and $\Lambda/\bar{\Lambda}$ candidates must lie within 3σ of their respective handbook mass values, and for background estimation, we use track pairs whose reconstructed masses lie between 5 and 8 σ above or 5 to 8 σ below the handbook mass.

To find out how much our K^0_s sample could be contaminated by Λ and $\bar{\Lambda}$, and vice-verse, we have made a scatter-plot (Figure 5.4) where the x of each point is the mass with a $\pi\pi$ hypothesis and the y of each point is the mass with a $p\pi$ hypothesis, and each track pair enters twice: once with each possible proton-pion assigment. The dashed vertical line shows the handbook K^0_s mass, the dashed horizontal line the Λ mass, and the pairs of solid vertical and horizontal lines show our K^0_s- and Λ-candidate mass cuts, respectively. Any track pairs that can be interpreted either as a K^0_s or as a Λ or $\bar{\Lambda}$ will fall in the region where the regions bounded by the solid lines overlap. There are 4 points in the overlap region, so at most 1% of the

K^0s sample can be Λ or $\bar{\Lambda}$, and at most 6% of the $\Lambda/\bar{\Lambda}$ sample can be K^0_s. We say "at most" because the background-subtraction process will remove a certain amount of the contamination in each sample from the final physis distributions.

Another way to check for K^0_s/Λ ambiguity, which is also revealing of some of the kinematic biases of our efficiencies, is shown in Figs. 5.5 and 5.6. In Fig. 5.5, we plot for each K^0_s candidate the momentum transverse to the parent direction, $p_\perp$, versus the decay-asymmetry parameter $(p^+_L - p^-_L)/(p^+_L + p^-_L)$, where p^+_L is the lab-frame momentum longitudinal with respect to the parent direction of the positive daughter, and p^-_L is the lab-frame longitudinal momentum of the negative daughter. In Fig. 5.6, we plot the same things for $\Lambda/\bar{\Lambda}$ candidates. The overlap between the clusters of points is clearly small. Also, interestingly, it is clear that we fail to reconstruct the most asymmetric K^0_s decays and the Λ decays where the pion is emitted backward in the center-of-mass. These failures are probably due primarily to the limited ability of the CTC tracking algorithm to find tracks with p_T below about 300 MeV.

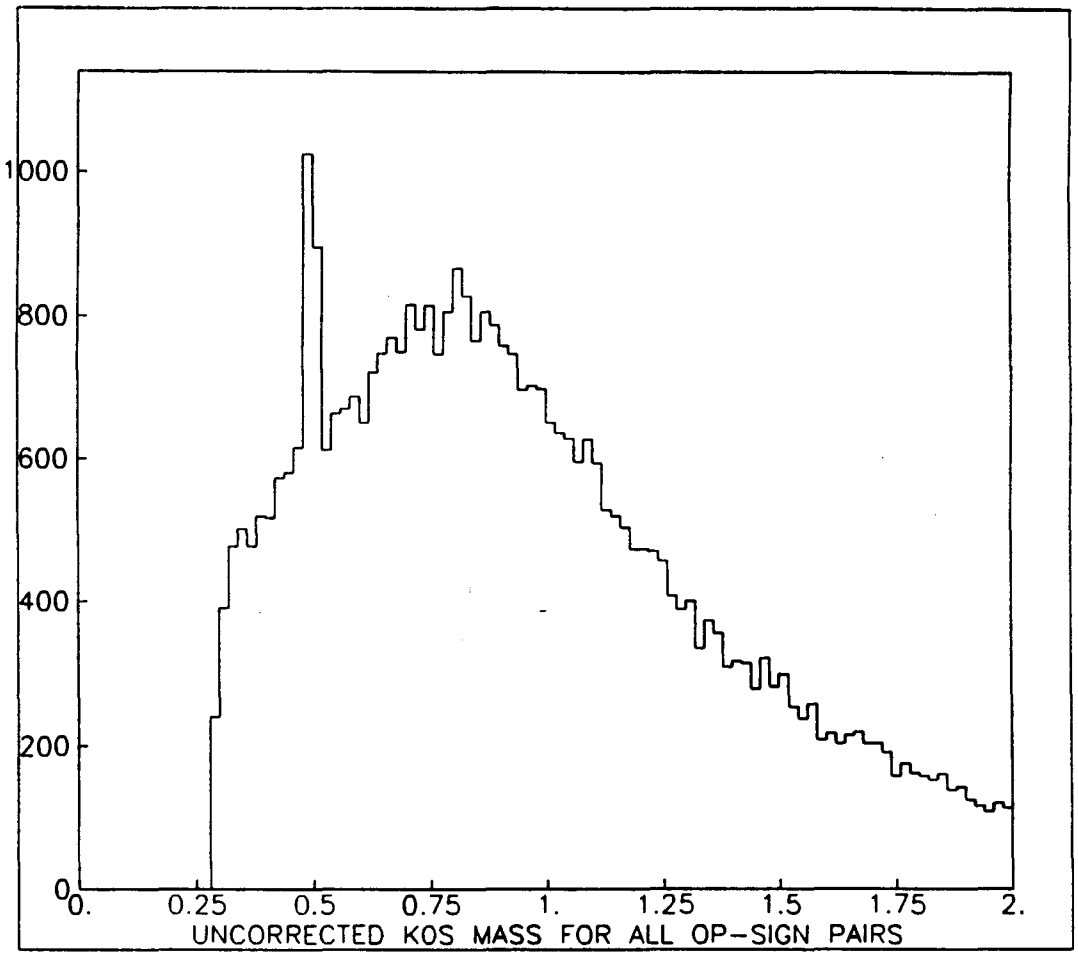

Figure 5.1

Invariant mass (in GeV) with a π-π mass assignment for all oppositely signed track pairs with acceptable vertices in the 1800 GeV data.

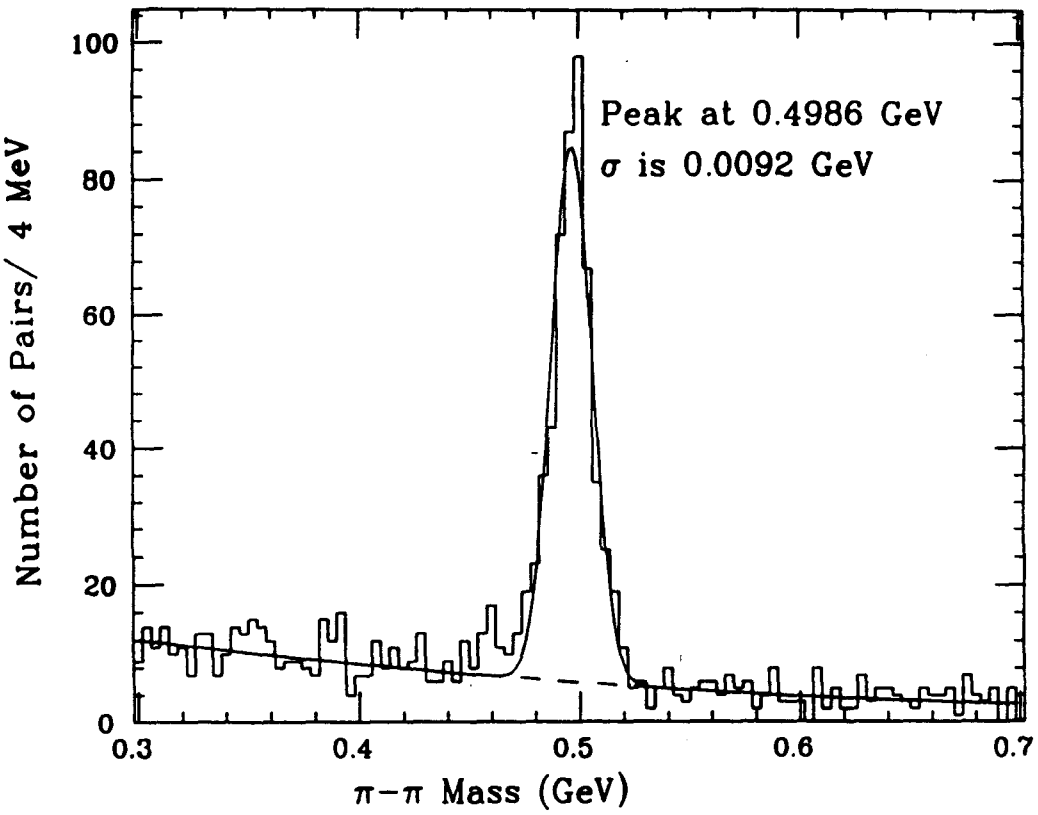

Figure 5.2

Invariant mass with a π-π mass assignment for oppositely signed track pairs passing all geometrical cuts in the 1800 GeV data.

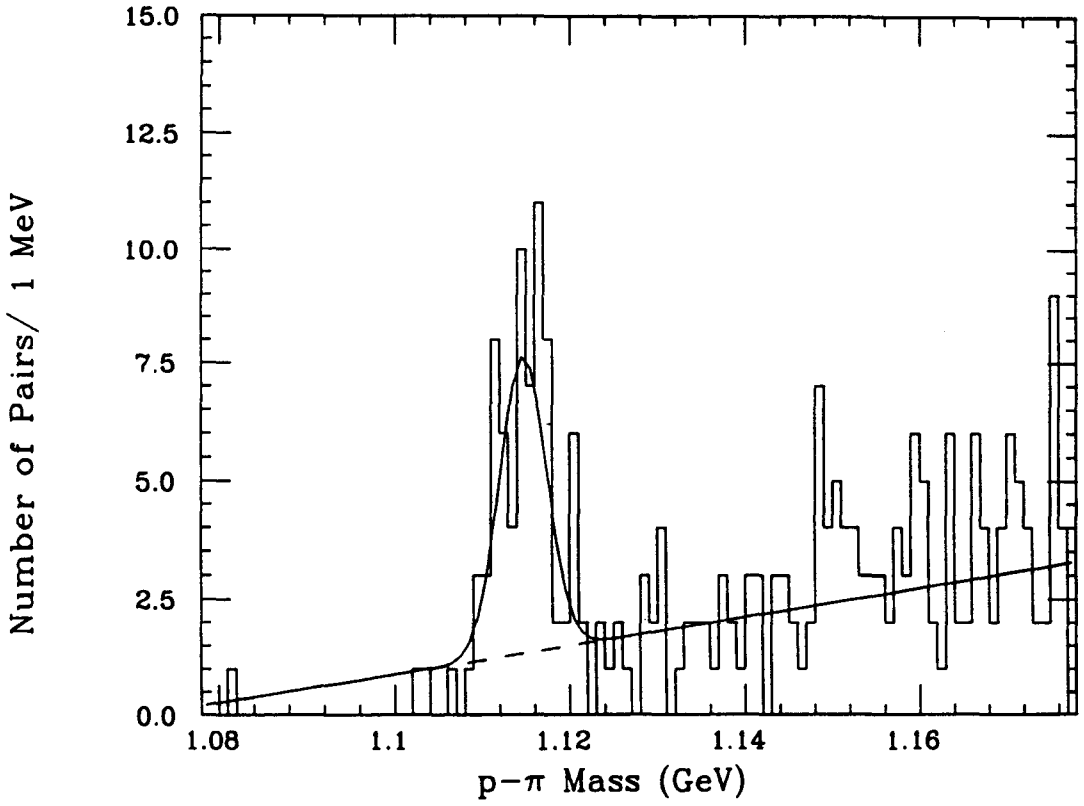

Figure 5.3

Invariant mass with a $p - \pi$ mass assignment for oppositely signed track pairs passing all geometrical cuts in the 1800 GeV data.

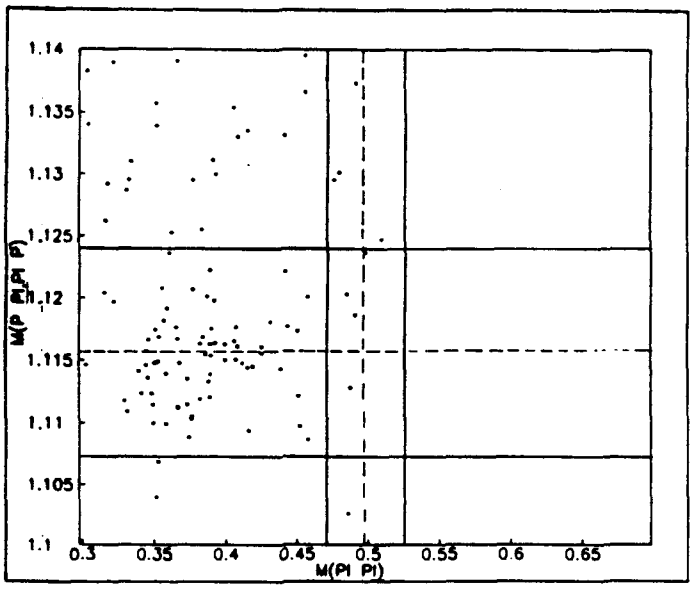

Figure 5.4

Mass with a $p\pi$ or πp mass hypothesis versus mass with a $\pi\pi$ hypothesis. Both masses are in GeV.

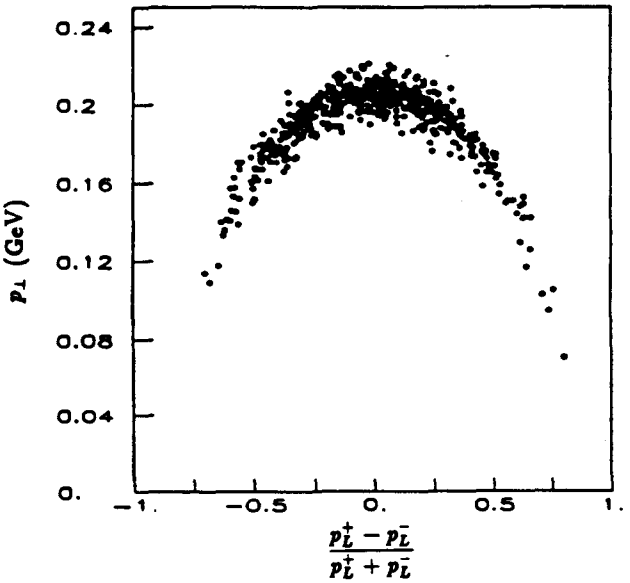

Figure 5.5

$p_\perp$ versus $(p_L^+ - p_L^-)/(p_L^+ + p_L^-)$ for pairs meeting the K_s^0-candidate cuts.

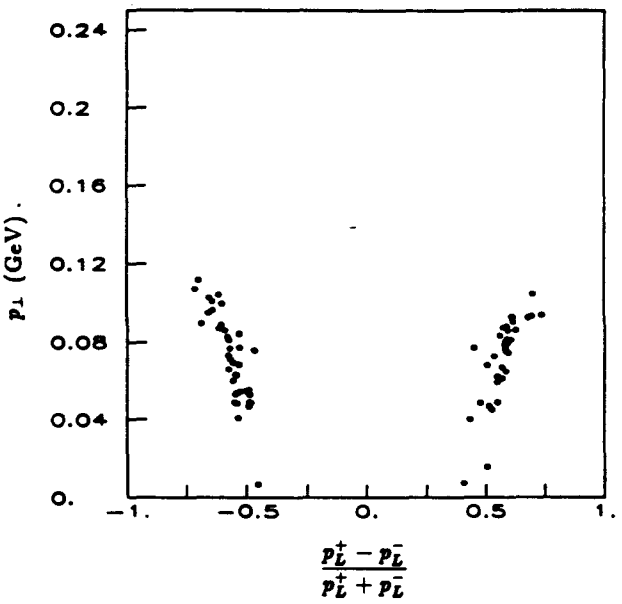

Figure 5.6

$p_\perp$ versus $(p_L^+ - p_L^-)/(p_L^+ + p_L^-)$ for pairs meeting the $\Lambda/\bar{\Lambda}$-candidate cuts.

6. EFFICIENCY CORRECTIONS

The p_T distributions for K_s^0 and $\Lambda + \bar{\Lambda}$ must be corrected for the efficiency with which the K_s^0 and Λ are found. The efficiency for finding K_s^0 and Λ is affected by many things, including the efficiency for finding the daughter tracks, the efficiency for finding an acceptable vertex where the daughter tracks meet, and the fractions of real K_s^0 and Λ which are eliminated by imposing cuts on K_s^0 and Λ candidates. All these effects will in general depend on the kinematics of the K_s^0 and Λ decays.

6.1 Efficiency Studies for K_s^0

The chances of finding a given K_s^0 depend not only on its p_T, but also on the kinematics of its decay—certain values of the center-of-mass decay angle ($\cos(\theta^*)$), number of proper lifetimes lived (t/τ), rapidities, etc. may be favored. We must average over all such variables in evaluating the efficiency at each p_T value. Also, the K_s^0 efficiency may be affected by confusion in the CTC— the CTC tracking algorithm may fail to find a given track when there are many hits near the track that do not belong on the track, or the track may be poorly reconstructed when the pattern recognition code becomes confused by hits not belonging to that track. We must model all these effects.

There is no practical way to gauge the corrections from the real data. Scanning events by eye is impractical, because K_s^0 that meet all our cuts are relatively rare in the minimum-bias data, and because the K_s^0-finding process involves finding

vertices of pairs of tracks in three dimensions, which is fairly difficult to do by eye.

Since there is no practical way to gauge the corrections from the real data, one must resort to simulation studies. The CDF simulation [13] allows us to easily average out the dependence on the kinematic variables, since it models K^0_s decays according to the proper kinematic distributions. The CTC confusion effect, however, is best modeled by the real data itself. The solution is to simulate a number of ensembles of K^0_s at fixed p_T, overlay the CTC hits from their daughter tracks on top of CTC hits from a real minimum-bias event, and pass the resulting CTC hit banks through exactly the same code that was used to find K^0_s in the real minimum-bias data sample. In order to measure the CTC-confusion effect, we then divide each fixed-p_T ensemble up according to the number of primary CTC tracks (N^{CTC}_{ch}) that were found in the event on which each simulated K^0_s was overlayed. We count the number of K^0_s found in each p_T-N^{CTC}_{ch} bin and divide by the number that were simulated in that bin to get the efficiency in that bin, thereby obtaining a 2-dimensional grid of efficiency values. In order to smooth out statistical fluctuations, we fit a function of p_T and N^{CTC}_{ch} over the 2-dimensional grid. When we generate the K^0_s p_T distribution from the real min-bias data, each K^0_s candidate and each background candidate is assigned a weight, based on this fitted efficiency function, according to the p_T of the candidate and the N^{CTC}_{ch} of the event in which the candidate was found.

6.1.1 Details of the Simulated K^0_s Samples

Samples of simulated events were prepared where each event contained nothing but a pair of back-to-back K^0_s, with the Pt of the K^0_s fixed throughout each sample.

All effects were turned on in the simulation, including decays, Molière multiple scattering, nuclear interactions, delta rays, etc. The B-field was set to 1.515 kG. the same value that was used in analysing the simulated events. The z coordinate from which each pair of K_s^0 came was forced to be the same as the VTPC vertex of the event on which the pair was superimposed, so that the $z_{\rm vertex}$ distribution was automatically taken into account and so that the CTC stereo reconstruction used the proper z starting point.

These pairs of K_s^0 were superimposed on a set of 500 events from a minimum bias run (CDF run number 7777). The events were required to pass the same selection criteria used on the real min-bias data sample. For runs where large statistics were necessary, we used these 500 events several times, superimposing a different random set of K_s^0 each time.

The "primary" CTC tracks that were counted were required to pass the same set of cuts used in the CDF single-charged-particle-spectrum paper [14].

The tracking algorithm used on both the real and simulated K_s^0 was Version 4.3.

The p_T values at which the efficiency is evaluated were chosen to ensure that there were enough points on the sharply-changing parts of the efficiency-vs-p_T curve to adequately determine its shape. The p_T values chosen were 0.6, 0.8, 1.0, 1.2, 1.5, 2.0, 2.5, 3.0, 3.5, 4.0, 6.0, and 10.0 GeV. The N_{ch}^{CTC} bins were chosen to divide the simulated samples roughly into fourths; the bins are as follows: N_{ch}^{CTC} = 0 through 3, 4 through 6, 7 through 11, and 12 and up. In the plots in the Results section, and in fitting the efficiency surface, weighted averages of N_{ch}^{CTC} are used.

They are: $N_{ch}^{CTC} = 2.13$, 5.01, 8.61, and 15.86, respectively.

The total sample sizes for each p_T value were as follows: for $p_T = 0.6$, 0.8, and 1.0 GeV, we simulated 4000 K_s^0 for each p_T value; for $p_T = 1.2$, 4.0, and 10.0, we simulated 1000 K_s^0, and for all other values of p_T, 2000 K_s^0 were simulated.

6.1.2 Results

The cuts used in the results that follow are the same as those used in the real data.

The efficiency for K_s^0, as a function of p_T, for fixed values of N_{ch}^{CTC}, is shown in Fig. 6.1. The efficiency for K_s^0 as a function of N_{ch}^{CTC} for fixed values of p_T is shown in Fig. 6.2. In both figures, the curves drawn in are the results of a fit to the "non-factorizing" form described below.

Note that in Fig. 6.1, the efficiency rises sharply at small p_T, due to the R_{vertex} cut and the sharp turn-on of the track-finding efficiency, and then falls gradually, due to the fact that high-p_T K_s^0 are more likely to decay at sufficiently high radii so that they do not leave hits in the innermost wire layers. Also, the efficiency is seen to drop with increasing N_{ch}^{CTC}. Fig. 6.3, the efficiency as a function of the number of proper lifetimes lived (see "Cross-Checks" below for more information on this plot), shows an increase in efficiency at small t/τ, due primarily to the effects of the R_{vertex} cut, and a gradual drop-off at large t/τ due again to the fact that tracks from decays at large radii are more difficult to reconstruct.

For each fixed-p_T sample, we have counted the number of simulated K_s^0 that survive each analysis step and each cut. The largest losses of K_s^0 occur in the CTC

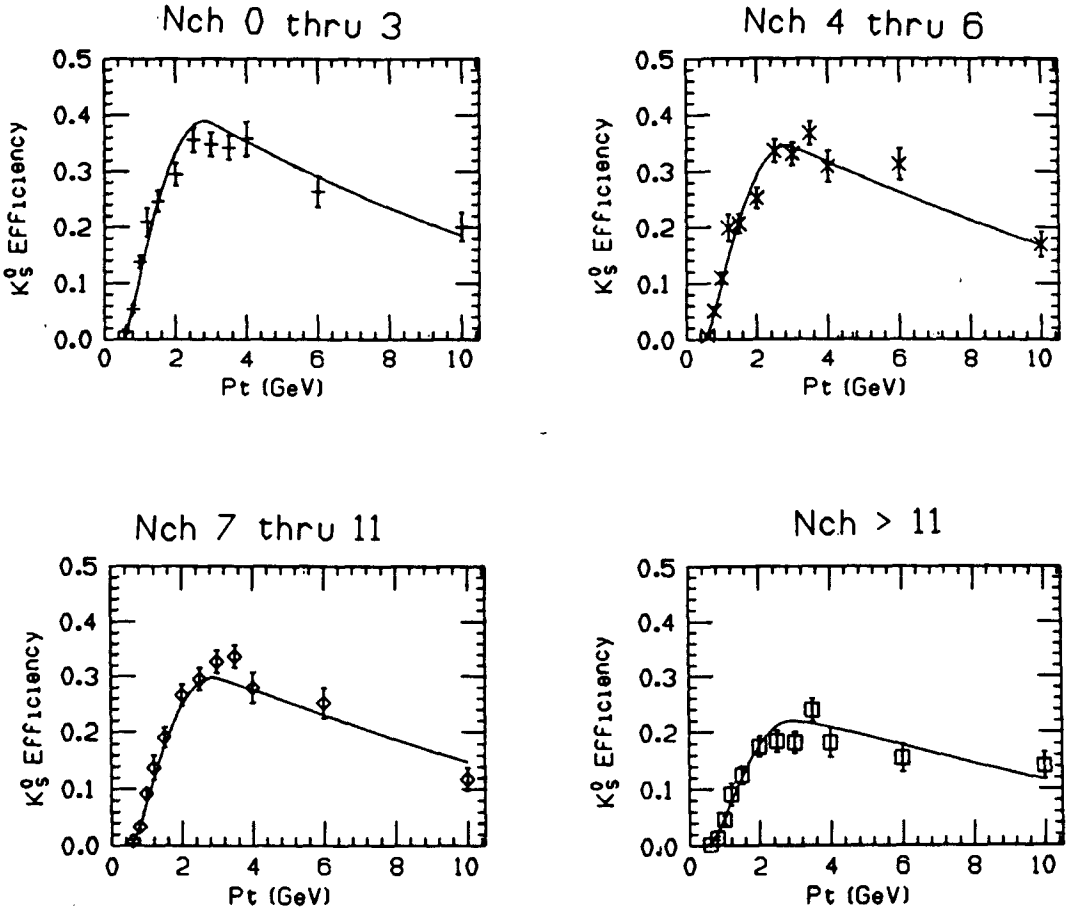

Figure 6.1

Efficiency for K^0_s as a function of p_T, for fixed values of N^{CTC}_{ch}.

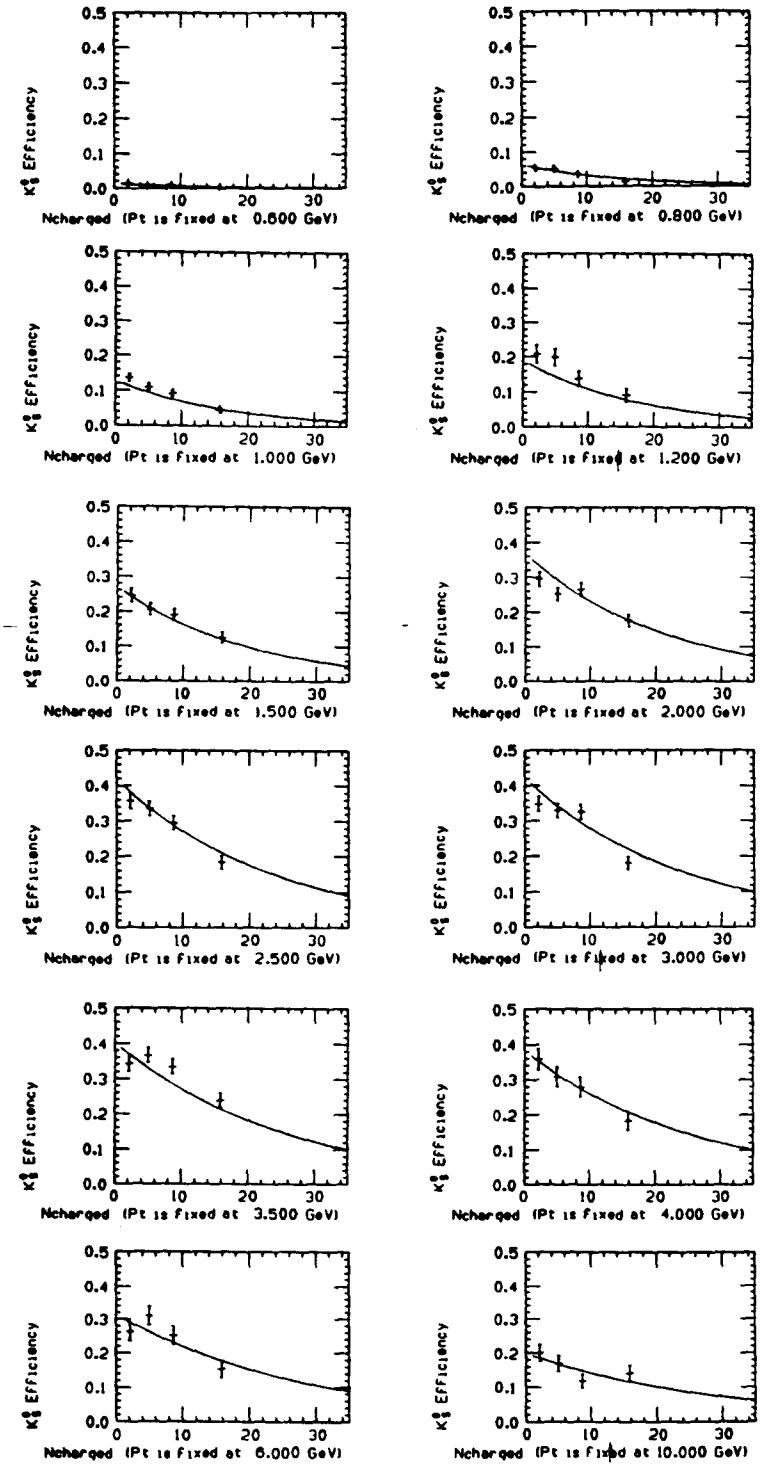

Figure 6.2

Efficiency for K_s^0 as a function of N_{ch}^{CTC}, for fixed values of p_T.

track-finding process and in the verticizing process.

6.1.3 Fitting the Efficiency Function

In correcting the K_s^0 physics distributions, we assign a weight to each K_s^0 candidate individually according to its p_T and the N_{ch}^{CTC} of the event in which it was found. Of course, real K_s^0 seldom fall exactly on one of the grid points, so we must somehow interpolate. Fitting the efficiency as a function of p_T and the N_{ch}^{CTC} allows us to do this interpolation, and also reduces the effects of fluctuations in the efficiency due to the limited statistics of the simulated samples.

There is no "theoretical guidance" available on the choice of functional forms to fit. The similarity in the shapes of the curves of Figs. 6.1 and 6.11 suggests that the p_T and N_{ch}^{CTC} dependence are independent (i.e., they "factorize"). Choosing a factorizing form also makes it easier for us to ensure that the efficiency is positive over the whole space of interest, that is, the space occupied by the real data. We have tried several such forms, and we find that the shape of the efficiency-vs-p_T plot at low p_T is actually significantly different for the high values of N_{ch}^{CTC}. To account for this, we have finally settled on the following non-factorizing form for the K_s^0 efficiency:

$$\epsilon(p_T, N_{ch}^{CTC}) = f(p_T)g(N_{ch}^{CTC}, p_T),$$

where $f(p_T)$ is a quadratic spline with 3 knots, at $p_T = x_1$, x_2, and x_3:

$$f(p_T) = \begin{cases} a_1 {p_T}^2 + b_1 p_T + c_1, & p_T \leq x_1 \\ a_2 {p_T}^2 + b_2 p_T + c_2, & x_1 \leq p_T \leq x_2 \\ a_3 {p_T}^2 + b_3 p_T + c_3, & x_2 \leq p_T \leq x_3 \\ a_4 {p_T}^2 + b_4 p_T + c_4, & x_3 \leq p_T, \end{cases}$$

where a_1, b_1, c_1, c_2, c_3, and c_4 are parameters of the fit, the remaining coefficients being fixed by continuity of function and slope at the knots, and

$$g(N_{ch}^{CTC}) = e^{-dN_{ch}^{CTC} - h\frac{1}{p_T}N_{ch}^{CTC}},$$

where d and h are parameters of the fit. The fit results are plotted on top of the efficiency points in Figs. 6.1 and 6.10. The χ^2 for this fit is 74.2, and the number of degrees of freedom is 40.

A histogram of the weights applied to the real K_s^0 candidates is shown in Fig. 6.4. The mean value is 10.7, and the r.m.s is 11.9.

6.1.4 Cross-Checks

6.1.4.1 Spectrum for Regular Cuts vs. Narrow Cuts One other check on the consistency of the efficiency calculation is a comparison of the K_s^0 spectrum that we get with the cuts listed above to the spectrum that we get if we choose a set of cuts that accept far fewer K_s^0 candidates. If the efficiencies are calculated correctly, the lower efficiencies (and thus larger weights) for the tighter cuts will correctly balance the reduced number of real K_s^0 passing these cuts, and the spectrum will come out the same as for our usual cuts. The "tight" cuts are the same as those above except that:

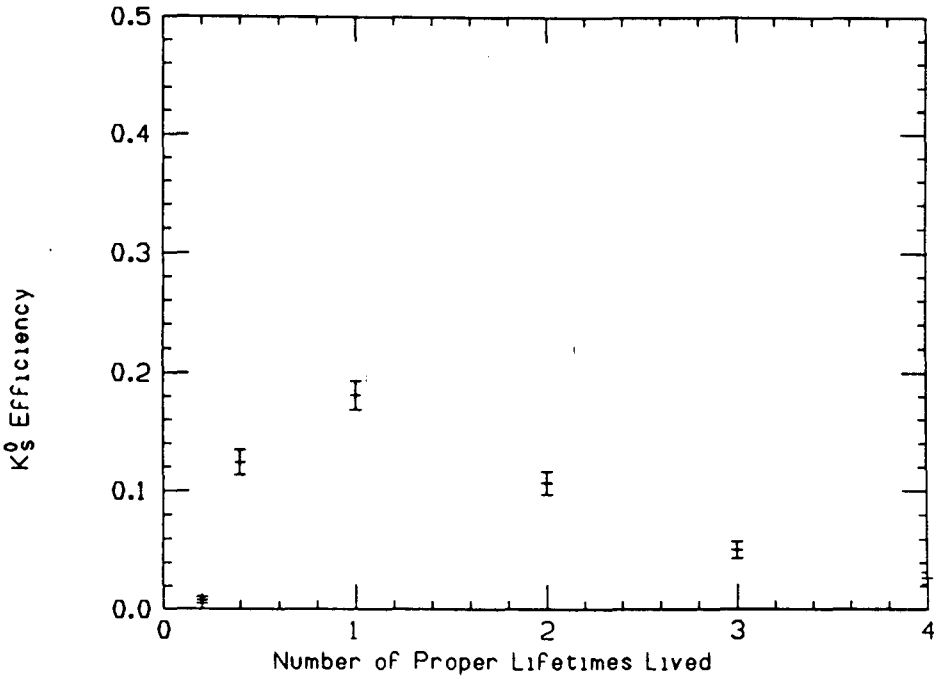

Figure 6.3

Efficiency for K^0_s as a function of t/τ.

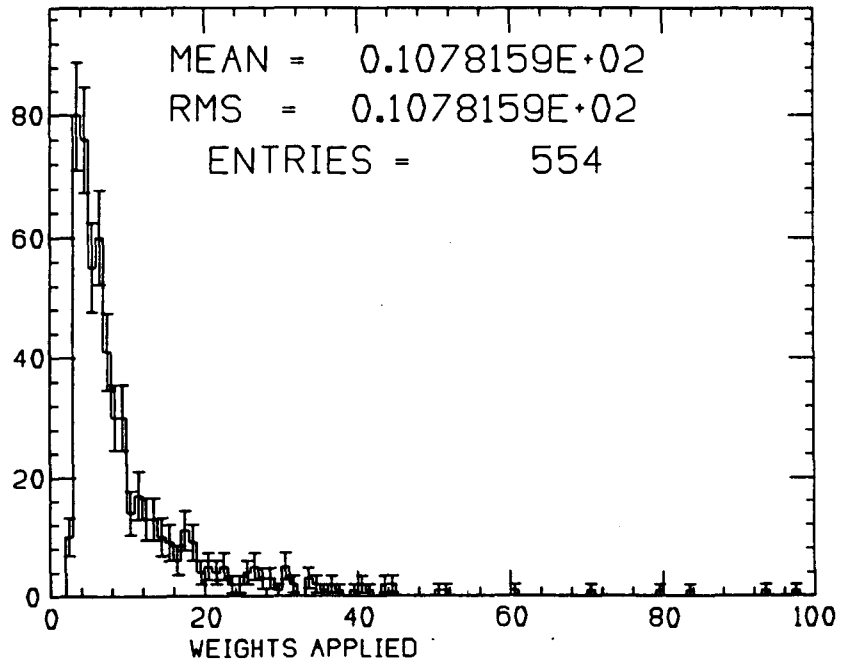

Figure 6.4

Weights for K^0_s candidates.

- The impact parameter of each track must be greater than 4 mm, and
- The transverse radius of the vertex formed by the tracks must be at least 4.0 cm.

There are 451 K^0_s above 105 background pairs when the usual cuts are applied, while there are only 365 K^0_s and 55 background when the tight cuts are imposed. The spectra for the two sets of cuts are plotted in Fig. 6.5. Note that though the number of K^0_s is different by about 20%, the spectra are consistent within statistical errors, and that tightening the cuts does not appear to introduce any appreciable systematic effect.

6.1.4.2 Corrected Lifetime Distribution- One may correct the lifetime distribution for K^0_s using a single large sample of simulated K^0_s with p_T distributed randomly according to our measured spectrum, and this forms another interesting cross-check on the efficiency calculation. After pattern-recognition and cuts have been applied to these simulated K^0_s, the number in each t/τ bin is, apart from a normalization factor, the efficiency for finding K^0_s that fall in that bin (more details on this correction technique are given in Appendix C). The corrected lifetime plot is shown in Figure 6.6. The less steeply-falling line has the expected slope of -1 and a fitted normalization. It will be seen that the points are reasonably consistent with this line. The steeper line was fitted with both the slope and the normalization as free parameters. The fit yields a slope of -1.3 ± 0.2.

6.1.4.3 Differences Between Real and Simulated K^0_s To make sure that the simulation really models the decay kinematics correctly, and has reasonable resolution and multiple-scattering effects, and has no hitherto unnoticed bugs, we have gen-

erated a small sample of simulated/superimposed K_s^0 according to a p_T spectrum similar to the result we will present in a later chapter, and we have compared the K_s^0 that the analysis code finds in this sample to the K_s^0 candidates in the real data. We have generated a number of histograms for the each sample, including kinematical quantities and parameters that we cut on, some of which are highly resolution-dependent. These histograms, normalized and plotted with error bars, appear in Appendix B. In the real data, background contributions have been subtracted (except for the mass plot); in the simulation, no background subtraction is necessary, because the program that calculates the efficiencies ignores candidates that come from the event on which the fake K_s^0 were overlayed.

It will be seen that the simulation plots are very similar to those for the real data, with three notable exceptions: the χ^2 of the vertex fit, the K_s^0 impact parameter, and the mass distribution. In each case, the distributions for the simulated K_s^0 are somewhat narrower than those in the real data. One can estimate by inspection the half-width-at-half-maximum for the impact parameter, and one can fit the σ of the mass peak. We find that the HWHM of the impact-parameter distribution is around 0.8 cm in the real data, and about 0.6 cm in the simulation, and the σ of the mass peak is 9.4 MeV for the real data, and 6.8 MeV for the simulation. We must insure that these differences have as little effect as possible on the final physics distributions.

While the shapes of the other plots are determined primarily by the things like decay kinematics, the shapes and widths of the three misbehaving distributions are determined entirely by pattern-recognition errors, measurement errors, and

multiple-scattering effects. We have examined some possible causes of the differences, and will discuss our findings below. However, we can minimize the effects of the differences in the widths of these distributions by deliberately choosing cut values that are far out in the tails of each of these distributions, so that the fraction of K_s^0 candidates cut is about the same in both real data and simulation. Looking at the χ^2 distribution, we see that the χ^2 cut at 5 is indeed well out in the tail, and the impact-parameter distribution convinces us that the 3-space impact parameter cut at 2 cm is also out in the tail. The mass window for K_s^0 candidates is $\pm 3\sigma$ about the K_s^0 mass, and it was chosen based on the real-data mass resolution, so only the tails of the mass peak are removed.

At present, the cuts used are identical for real data and for simulation. One could attempt to account for the differences in the widths of the real-data and simulation distributions by rescaling the cuts according to the differences in the widths. Thus, one would rescale the impact parameter cut from its usual 2 cm to $(0.6\text{cm})/(0.8\text{cm}) \cdot (2\text{cm}) = 1.5$ cm, and one would rescale the mass windows such that they are based on a σ of 6.8 MeV. It is not so clear how the χ^2 distribution should be scaled, but as a first guess one might rescale it by the same factor of $\sim 3/4$ that one sees in the other distributions; that is, it should be around 3/4 of 5, or 3.75.

This exercise has been done. To get a feeling how much difference the rescaled cuts make, they have been applied to the large sample of simulated K_s^0 that were generated according to our measured p_T spectrum; the number of K_s^0 found went from 625 with the usual cuts to 590 with the rescaled cuts; that is, about a 6%

difference. The cross-section generated by the usual technique (same cuts for data and simulation) is compared in Figure 6.7 to the cross-section generated with corrections derived with the rescaled cuts. The difference is almost invisible in the cross-section plot, thanks to the log-scale. Figure 6.8 compares the K/hadron ratio plots similarly, but on a linear vertical scale, and the difference is somewhat more visible, but is still negligible compared to the statistical errors.

This exercise gives us an estimate of the systematic error induced by differences between the simulation and the real data; it is about 6%.

6.1.4.4 Search for the Cause of the Differences We have investigated a couple of possible causes for the real-data/simulation differences.

First, the value of the CTC setting error used by the simulation is not the same as the setting error derived for the set of tracking code and drift constants (Version 4.3) used to track the real data. In Version 4.3 tracking, the CTC hit resolution was around 300 microns, while in the simulation, it is set to 200 microns. Because the roads used by the track-finding algorithm are of order 1-2 mm wide, this should have little or no effect on the CTC track finding efficiency. The setting error also sets the scale for the calculation of the track parameter errors due to the chamber resolution; however, the errors used in the verticizing algorithm also include contributions due to multiple scattering, which will in general dominate. To make sure the CTC resolution is not the culprit, we have generated a small sample of simulated K^0_s according to our p_T spectrum, as before, but with the simulated CTC hit resolution set to 300 microns. We see no difference in widths in the misbehaving distributions between this sample and the sample generated with

the usual CTC simulation.

Second, because multiple scattering is expected to dominate the errors on the measured track parameters, we have searched for mistakes in either the multiple-scattering algorithm or the amount of material prior to the CTC in the geometry database. The latter was checked [15], by shooting particles through the simulation at various angles and making plots of the number of radiation lengths a particle passed through before it got to the CTC active volume. That plot appears here as Figure 6.9. Figure 2.7 is a copy of the corresponding plot from Ref. [4], which was produced by calculating radiation lengths by hand. In the central region, at least, the plots are very similar. In fact, Fig. 6.9 is somewhat more realistic than Fig. 2.7, because Fig. 6.9 includes the lump near 90 degrees (at $z = 0$) that corresponds to the VTPC walls at the center of the detector. In inspecting the simulation code, however, we have nonetheless found an error which was causing the wrong radiation length to be used for the CTC inner wall; this error changed the total number of radiation lengths before the CTC at 90 degrees to 2.5 %, compared to the true value of 3 %. Since multiple-scattering effects are proportional to the square root of the number of radiation lengths, this error has a negligible effect.

Of course, the study of Ref. [15] study only demonstrates that the amount of material in the simulation geometry is about right, but it does not demonstrate that the simulation actually correctly handles multiple scattering in this material. Inspection of the program reveals no obvious bugs, however.

There are a couple of other known effects that are not modeled by the CTC simulation: It is known that the LeCroy TDCs that are used to read out the CTC

hits have some problems that cause some percentage of hits to be randomly lost. This effect is small. Also, there is a certain amount of cross-talk between wires in the CTC which causes track-associated noise. This effect is also small.

One other possible cause for the differences between simulated and real K_s^0 involves the CTC drift velocity, which is slightly different for each cell. When one extrapolates tracks back into the CTC inner bore, the hits on the innermost CTC wires are quite important. It is quite possible that poor drift constants for the innermost CTC superlayers (an effect that of course is not present in the simulation) are in part responsible for the increased widths of the real-data distributions.

6.2 Efficiency Studies for Λ and $\bar{\Lambda}$

The techniques used to obtain the efficiencies for Λ and $\bar{\Lambda}$ are nearly the same as those used to get the K_s^0 efficiencies, and we will discuss below the few differences. Fewer cross-checks are available for the cross-checks on the Λ efficiency than for the K_s^0 studies, due to the much smaller number of Λ and $\bar{\Lambda}$ candidates. We therefore rely on the K_s^0-efficiency cross-checks to establish the soundness of the technique.

For the lambda/anti-lambda efficiency studies, the samples of simulated events contained nothing but a pair of back-to-back Λ or $\bar{\Lambda}$, or one of each, selected randomly such that the total number of Λ in the sample was approximately equal to the total number of $\bar{\Lambda}$. We expected our efficiency for finding lambdas to be the same as for finding anti-lambdas, and in fact, in each of our simulated samples, after reconstruction and application of the cuts, the number of lambdas that survived was the same, within statistical errors, as the number of anti-lambdas that survived. From here on, then, Λ and $\bar{\Lambda}$ will be treated together. The combined efficiency for

equally-mixed samples of Λ and $\bar{\Lambda}$, as a function of p_T, for fixed values of N_{ch}^{CTC}, is shown in Fig. 6.10, and the efficiency for the same samples, as a function of N_{ch}^{CTC} at fixed p_T is shown in Fig. 6.11. In both figures, the lines are the results of a fit to the factorizing spline fit described below. The average weight applied to a Λ or $\bar{\Lambda}$ candidate was 19. The combined efficiency as a function of the number of proper lifetimes lived is shown in Fig. 6.12.

Because there are so few Λ and $\bar{\Lambda}$ candidates, even relatively small simulated samples will deterimine the efficiency to better statistical accuracy than the statistical errors due to the number of candiates in the real data. The combined number of Λ and $\bar{\Lambda}$ in each fixed-p_T sample was 1000. Because the simulated samples are smaller than in the K_s^0 studies, the complicated form used in the K_s^0 efficiency fits is unnecessary, and we use instead a factorizing form involving 2-knot splines:

$$\epsilon(p_T, N_{ch}^{CTC}) = f(p_T)g(N_{ch}^{CTC}),$$

where $f(p_T)$ is a quadratic spline with 2 knots, at $p_T = x_1$ and x_2:

$$f(p_T) = \begin{cases} a_1 {p_T}^2 + b_1 p_T + c_1, & p_T \leq x_1 \\ a_2 {p_T}^2 + b_2 p_T + c_2, & x_1 \leq p_T \leq x_2 \\ a_3 {p_T}^2 + b_3 p_T + c_3, & x_2 \leq p_T, \end{cases}$$

where a_1, b_1, c_1, c_2, and c_3 are parameters of the fit, the remaining coefficients being fixed by continuity of function and slope at the knots, and

$$g(N_{ch}^{CTC}) = e^{-dN_{ch}^{CTC}}$$

where d is a parameter of the fit. The χ^2 of this fit was 39, and the number of degrees of freedom was 36.

The single cross-check on the combined $\Lambda + \bar{\Lambda}$ efficiency is the corrected lifetime distribution, shown in Fig. 6.13. The line shown was fitted with both normalization and slope as free parameters; the fit yields a slope of -1.0 ± 0.3, and a slope of -1 is exactly what we expect if sample is pure Λ and $\bar{\Lambda}$ and if the efficicency corrections are done properly.

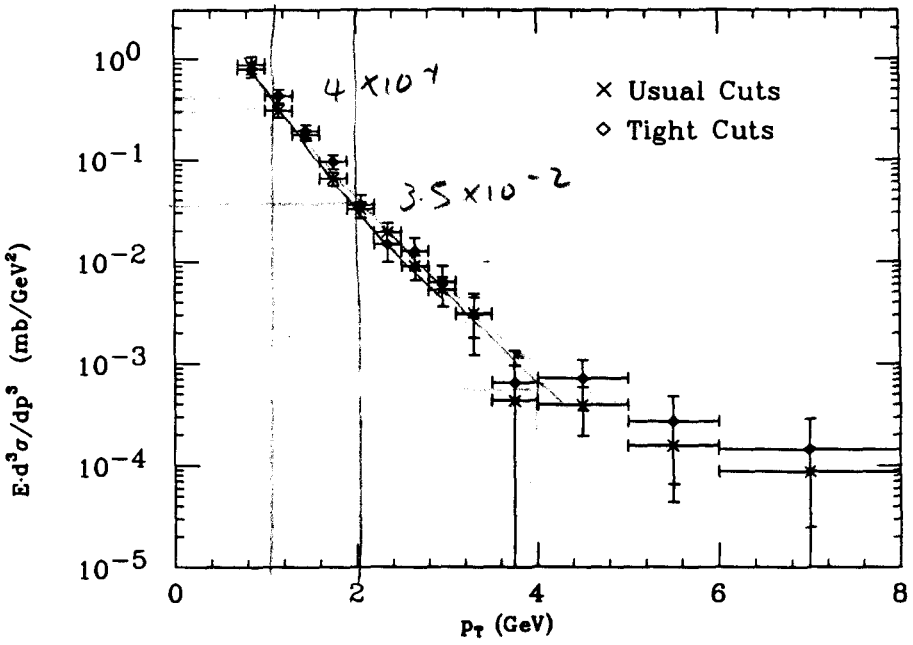

Figure 6.5

K_s^0 spectrum at 1800 GeV, with normal cuts and with tightened cuts.

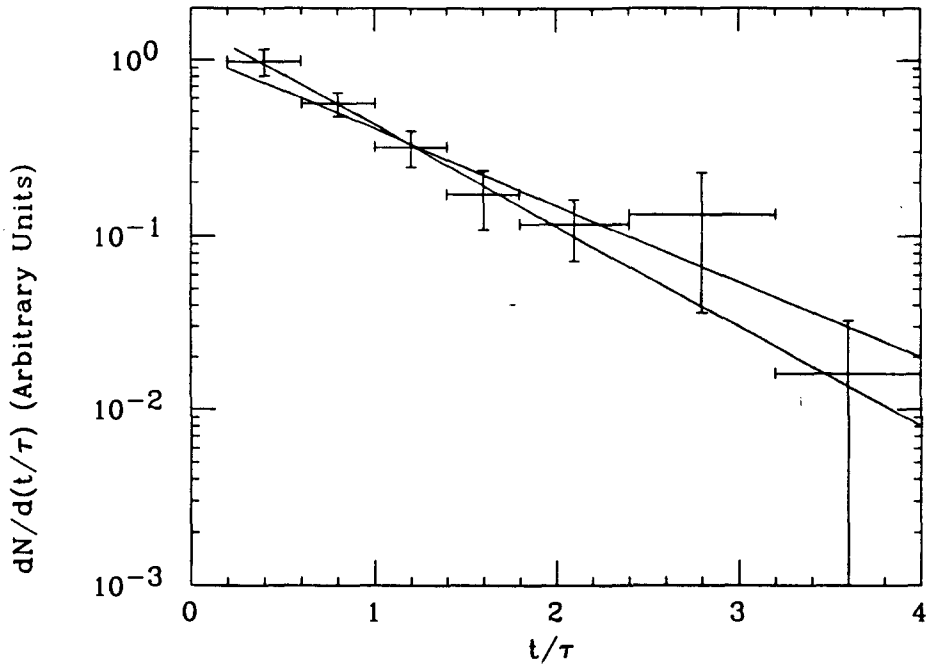

Figure 6.6

Corrected K_s^0 lifetime distribution for the 1800 GeV data, with a line of unit slope and a steeper, fitted line of slope -1.3 ± 0.2.

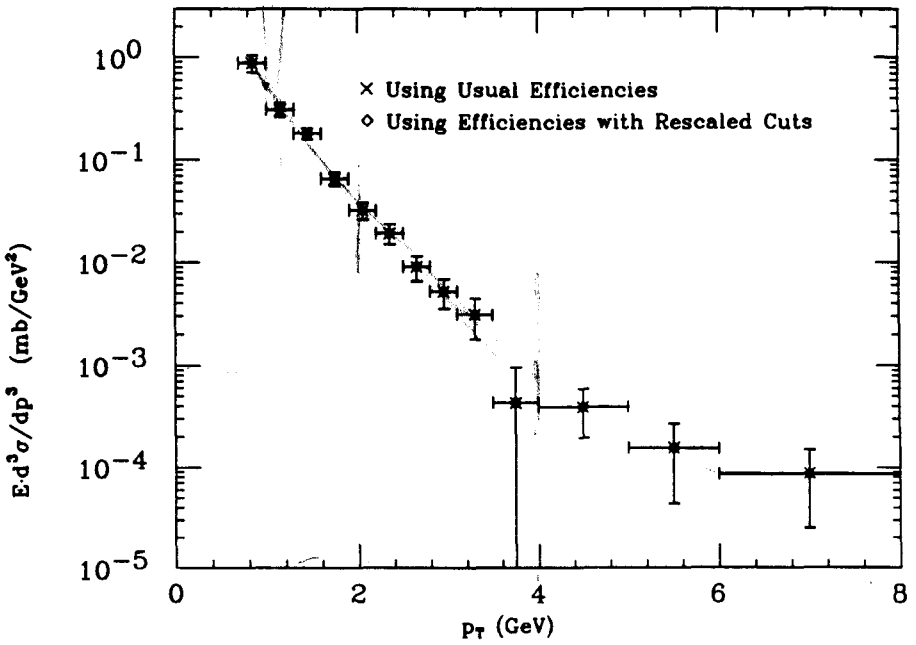

Figure 6.7

K_s^0 cross-section at 1800 GeV, with and without rescaled cuts for simulation.

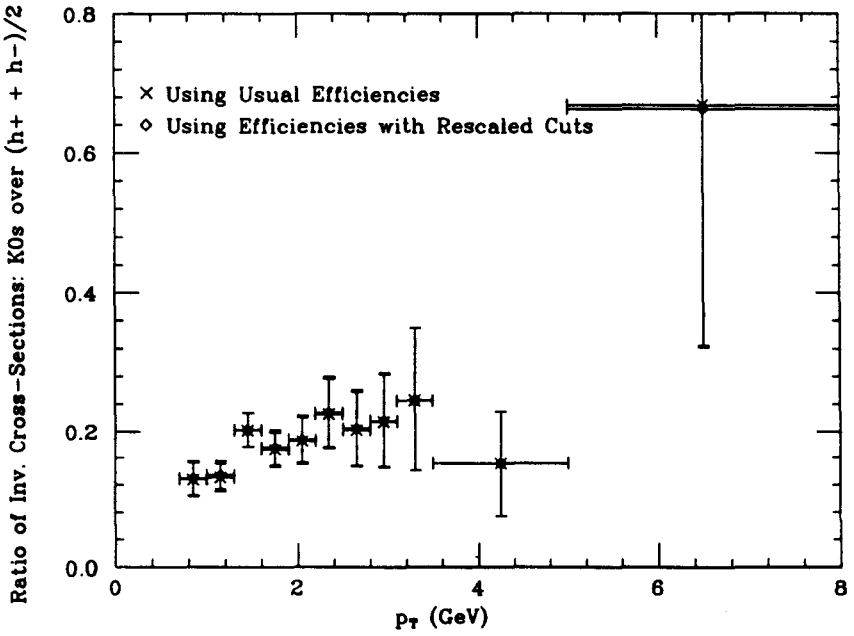

Figure 6.8

K_s^0/hadron ratio at 1800 GeV, with and without rescaled cuts for simulation.

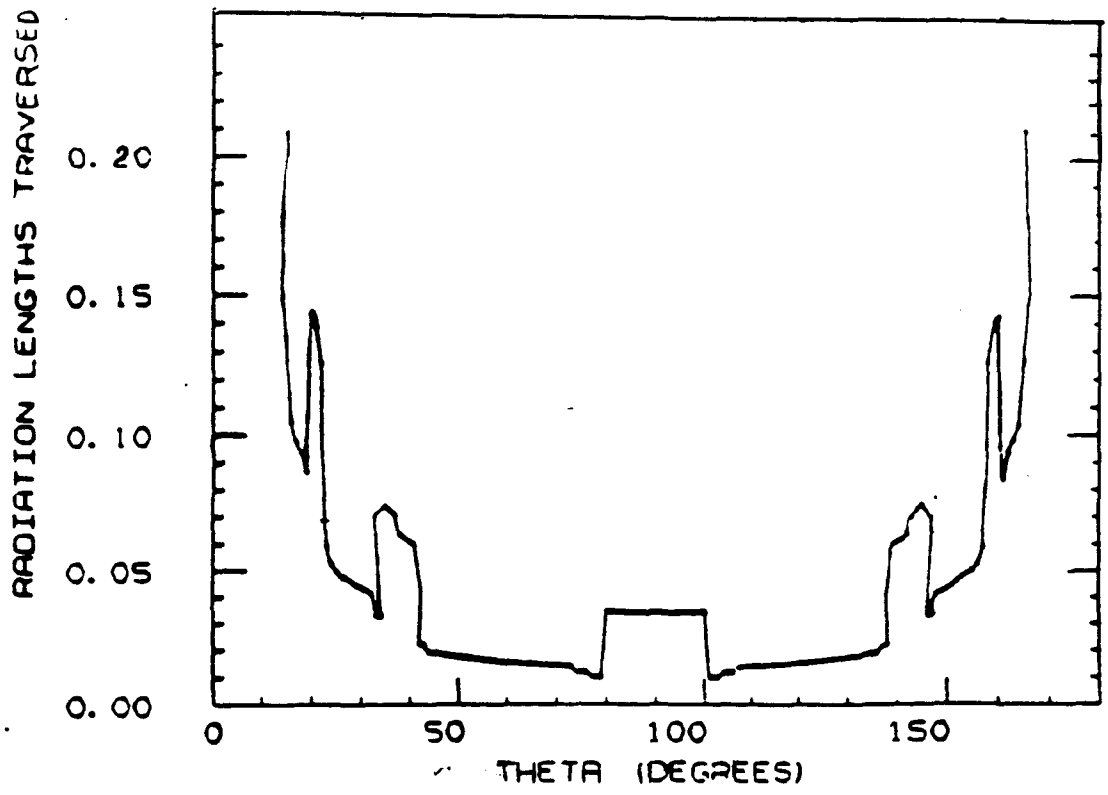

Figure 6.9

Total amount of material between the beam and the CTC vs angle, based on the CDF simulation.

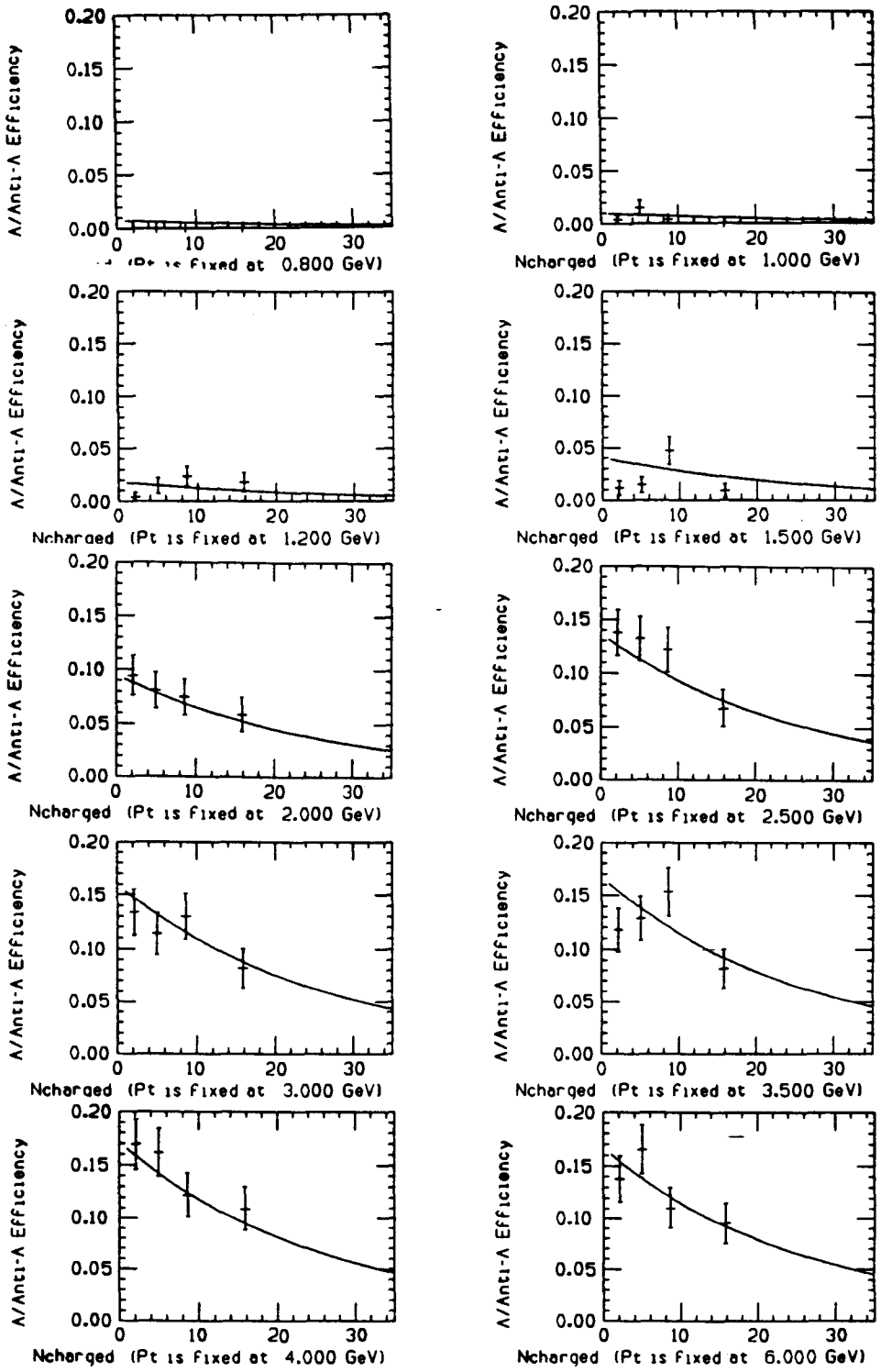

Figure 6.10

Efficiency for equally-mixed samples of Λ and $\bar{\Lambda}$ as a function of N_{ch}^{CTC}, for fixed values of p_T.

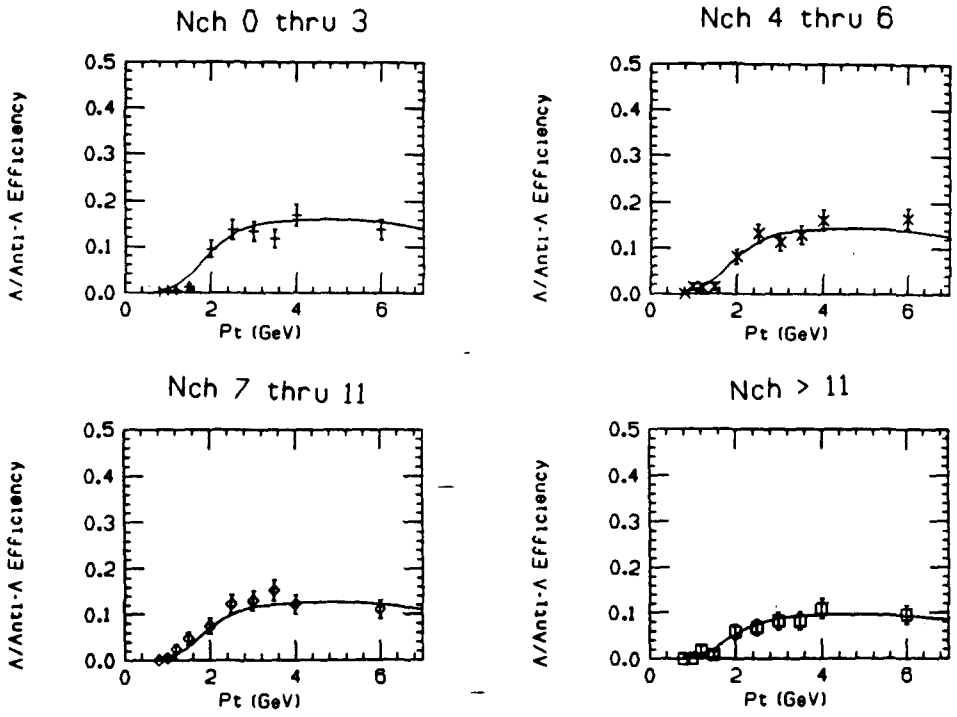

Figure 6.11

Efficiency for equally-mixed samples of Λ and $\bar{\Lambda}$ as a function of p_T, for fixed values of N_{ch}^{CTC}.

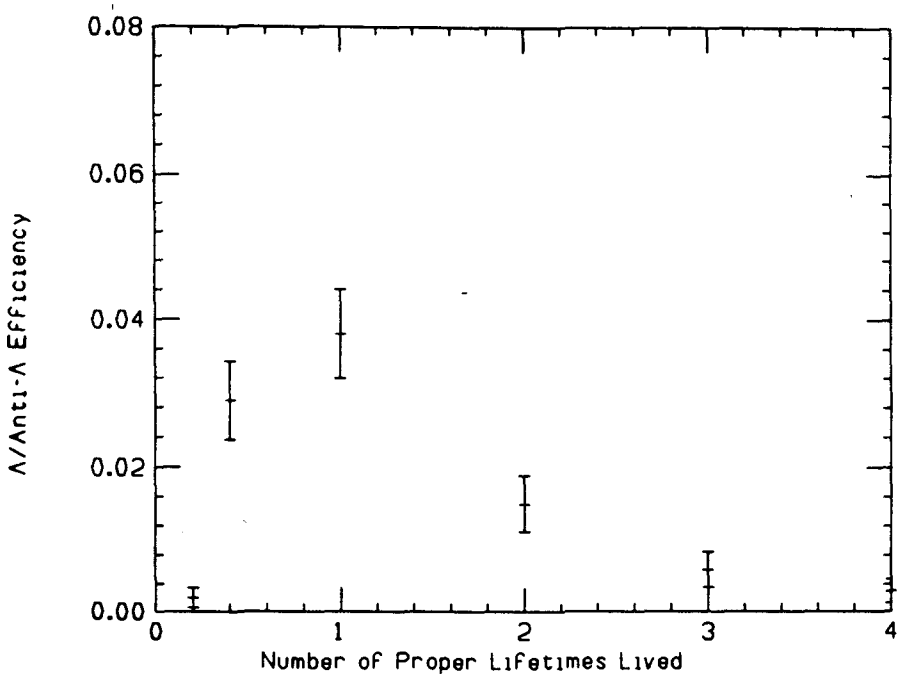

Figure 6.12

Efficiency for equally-mixed samples of Λ and $\bar{\Lambda}$ as a function of t/τ.

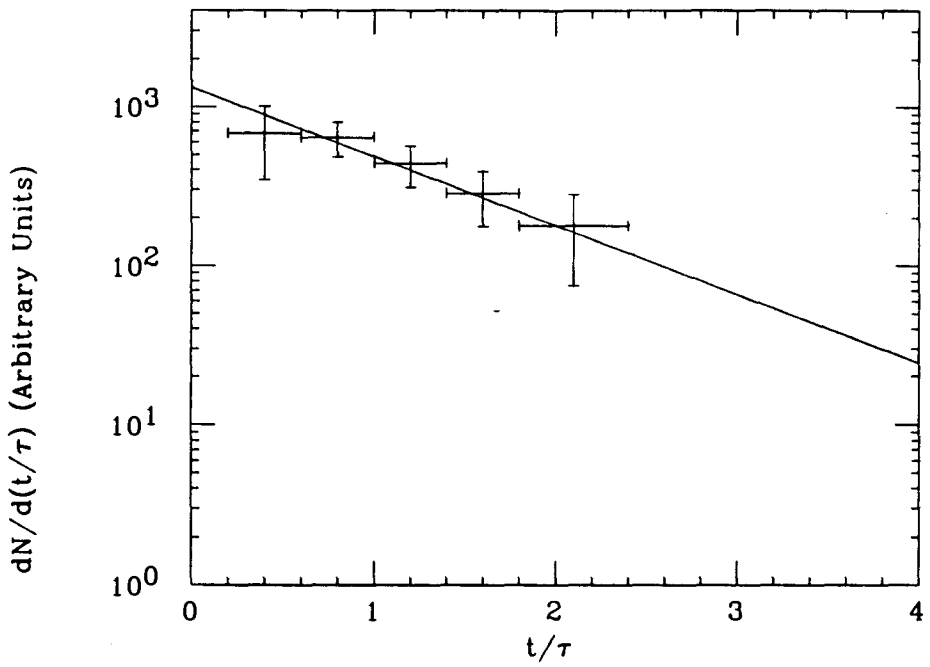

Figure 6.13

Corrected lifetime distribution for $\Lambda + \bar{\Lambda}$ in the 1800 GeV data, showing a fitted line of slope -1 ± 0.3.

7. CALCULATING THE CORRECTED K_s^0 and $\Lambda + \bar{\Lambda}$ SPECTRA

7.1 Background Subtraction

As we have seen in Figure 5.2, even after all the geometrical cuts have been applied, some background is still present, and we must remove its effects from the final physics distributions. Fits performed on the data of Fig. 5.2 and Fig. 5.3 indicate that the backgrounds for K_s^0 and $\Lambda + \bar{\Lambda}$ both rise slowly and very nearly linearly in the vicinity of the respective peaks. We may therefore estimate the background contribution to physics distributions using the average of the distributions for events in the background windows above and below the peaks. The mass values used to define the K_s^0 and Λ peaks and the background windows are listed in Chapter 5.

To subtract the background contribution from the p_T spectrum of K_s^0, we proceed as follows (the procedure for lambdas is the same). We make a histogram of p_T for all pairs falling within the K_s^0 mass-peak window, weighting each K_s^0 according to its p_T and the primary CTC multiplicity of the event in which it was found. We then make the same plot for events that fall in the background mass-windows, weighting each such pair in exactly the same way that the K_s^0 candidates were weighted. For the K_s^0, we then divide the bin contents of the second histogram by 2, to account for the fact that each of the two background windows is exactly as wide as the signal window, while for the lambdas, no division by 2 is necessary

because each background window is 1/2 as wide as the signal window. Finally, we subtract the resulting background histogram, bin by bin, from the histogram for the respective K^0_s or $\Lambda + \bar{\Lambda}$ candidates.

7.2 Turning the p_T Distribution into an Invariant Cross-Section

After the corrections have been applied and the contribution of the background has been subtracted, we have a corrected p_T distribution. The distributions we want, however, are the Lorentz-invariant cross-sections, as functions of p_T, for producing K^0_s and for producing Λ and $\bar{\Lambda}$. The Lorentz-invariant cross-section is the cross-section per unit of Lorentz-invariant phase space, $d^4p\,\delta(p^2 - m^2)$, where p is the 4-momentum of the particle, m is its mass, and and $d^4p \equiv dp_x dp_y dp_z dE$. At fixed p_T, the Dirac delta-function can be removed by integrating over E:

$$\int \delta(p^2 - m^2) dE = \int \delta(\zeta) \frac{dE}{d\zeta} d\zeta,$$

where $\zeta \equiv p^2 - m^2$, so the differential element of phase-space can be written as d^3p/E, where $d^3p \equiv dp_x dp_y dp_z$. The Lorentz-invariant cross-section is then $E d^3\sigma/d^3p$. Since we have a p_T distribution, and we have assumed that K^0_s and Λ are produced uniformly in y, we would like to express the invariant cross-section in terms of these variables. Recall that p_T is defined as $(p_x^2 + p_y^2)^{1/2}$, and that we can use the usual transformation between cartesian and cylindrical coordinates to rewrite $dp_x dp_y$ as $p_T dp_T d\phi$, where ϕ is the azimuth coordinate. We can then write

$$E\frac{d^3\sigma}{d^3p} \equiv E\frac{d^3\sigma}{dp_x dp_y dp_z} = E\frac{d^3\sigma}{p_T dp_T d\phi dp_z}.$$

A little manipulation shows that $dy = dp_z/E$, so

$$E\frac{d^3\sigma}{d^3p} = \frac{d^3\sigma}{p_T dp_T d\phi dy}.$$

Let N be the contents of one bin of the corrected, background-subtracted p_T distribution. To get the invariant cross-section for each p_T bin we have only to relate the differential cross-section to N. N is the total number of particles produced in our y interval ($|y| < 1$), over all ϕ, with transverse momenta between p_T and $p_T + \Delta p_T$. If $\int \mathcal{L}dt$ is the integrated luminosity,

$$N = p_T \Delta p_T \int_{\Delta\phi} d\phi \int_{\Delta y} dy \frac{d^3\sigma}{p_T dp_T d\phi dy} \int \mathcal{L}dt.$$

Because the initial state of the $p\bar{p}$ collision process is azimuthally symmetric, we expect no azimuth-dependence of the cross-section, so the integral over ϕ is just $\Delta\phi$, or 2π. We assume that the p_T, y and ϕ dependences of the cross-section are not interrelated, i.e., that the cross-section "factorizes". Then

$$E\frac{d^3\sigma}{d^3p} = \frac{N}{p_T \Delta p_T \Delta\phi \Delta y \int \mathcal{L}dt}.$$

The integrated luminosity is related to the total number of events N_{ev} that pass our trigger and event-selection criteria and to the effective cross-section to which we are sensitive:

$$N_{ev} = \sigma_{eff} \int \mathcal{L}dt,$$

so now (at last!) we have an expression that allows us to convert each bin of the p_T distribution to an invariant cross-section value:

$$E\frac{d^3\sigma}{d^3p} = \frac{\sigma_{eff}}{N_{ev}} \frac{N}{p_T \Delta p_T \Delta\phi \Delta y}.$$

For p_T and Δp_T we use the bin center and the bin width, respectively. Δy is 2, $\Delta\phi$ is 2π, and the numbers of events and the effective cross-sections for the 630 GeV and 1800 GeV runs were given in Chapter 3.

Finally, it is customary to present cross-sections that reflect the production of all K_s^0, Λ, and $\bar{\Lambda}$, not just those that decay into charged particles. Therefore, we divide all K_s^0 cross-section values by 0.6861, the branching fraction [12] for the decay $K_s^0 \rightarrow \pi^+\pi^-$, and all $\Lambda + \bar{\Lambda}$ cross-section values by 0.641, the branching fraction for the decay $\Lambda \rightarrow p\pi^-$ (which is the same as the branching fraction for $\bar{\Lambda} \rightarrow \bar{p}\pi^+$).

8. SPECTRA AND CROSS-SECTION RATIOS

8.1 The K_s^0 Spectrum

The corrected, background-subtracted inclusive cross-sections for K_s^0 production at $\sqrt{s} = 630$ and 1800 GeV are shown in Fig. 8.1. The solid lines are fits to the cross-section data that will be discussed in Chapter 9. The data points in the figure are tabulated in Tables 8.1 and 8.2, where the units on the cross-section values are mb/(GeV^2/c^3). The statistical uncertainties on the 630 GeV data are large, but it is still reasonable to say that the cross-section is smaller at 630 GeV than at 1800 GeV. Unfortunately, the large uncertainties do not allow us to tell whether there is any difference in shape between the 630 GeV and 1800 GeV data.

Fig. 8.2 shows our 1800 and 630 GeV data along with data taken at lower energies. The dashed line is a fit to the $\sqrt{s} = 546$ GeV data of UA5 [17]. The circular data points are charged kaon data (averaged over positive and negative signs) at $y = 0$ from the Chicago-Princeton (CP) collaboration [16] taken at $\sqrt{s} =$ 27 GeV. The shape of our 630 GeV cross-section agrees reasonably well with the fit to the 546 GeV data of UA5. However, at fixed p_T the cross-section is much higher at Tevatron energies than it is in the $\sqrt{s} = 27$ GeV CP data.

It is also instructive to consider the ratio, as a function of p_T, of the cross-section for K_s^0 to the cross-section for charged hadrons, averaged over positive and negative charges. The CDF measurements of the charged hadron cross-section

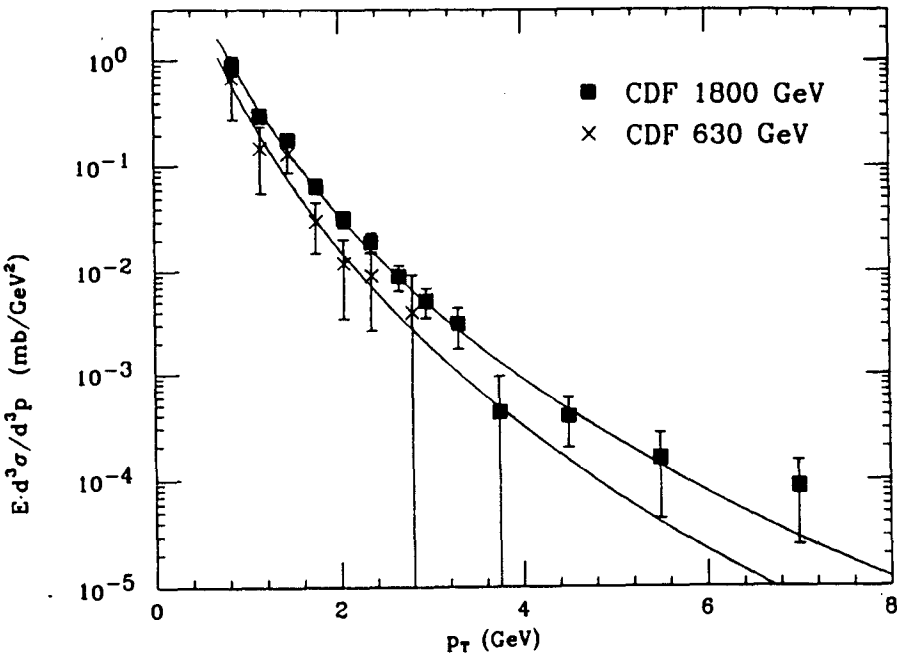

Figure 8.1

Inclusive cross sections for K_s^0 production in rapidity $|y| < 1.0$ in 630 and 1800 GeV proton-antiproton collisions, with fitted curves.

Table 8.1

Inclusive cross-section for K_s^0 in $|y| < 1$ in proton-antiproton collisions at a c.m. energy of 630 GeV, and its statistical uncertainty.

p_T (GeV)	$Ed^3\sigma/d^3p$ (mb/GeV^2)		
0.85	0.7	$\pm$	0.4
1.15	0.15	$\pm$	0.09
1.45	0.13	$\pm$	0.04
1.75	0.03	$\pm$	0.02
2.05	0.012	$\pm$	0.009
2.35	0.009	$\pm$	0.006
2.80	0.004	$\pm$	0.005

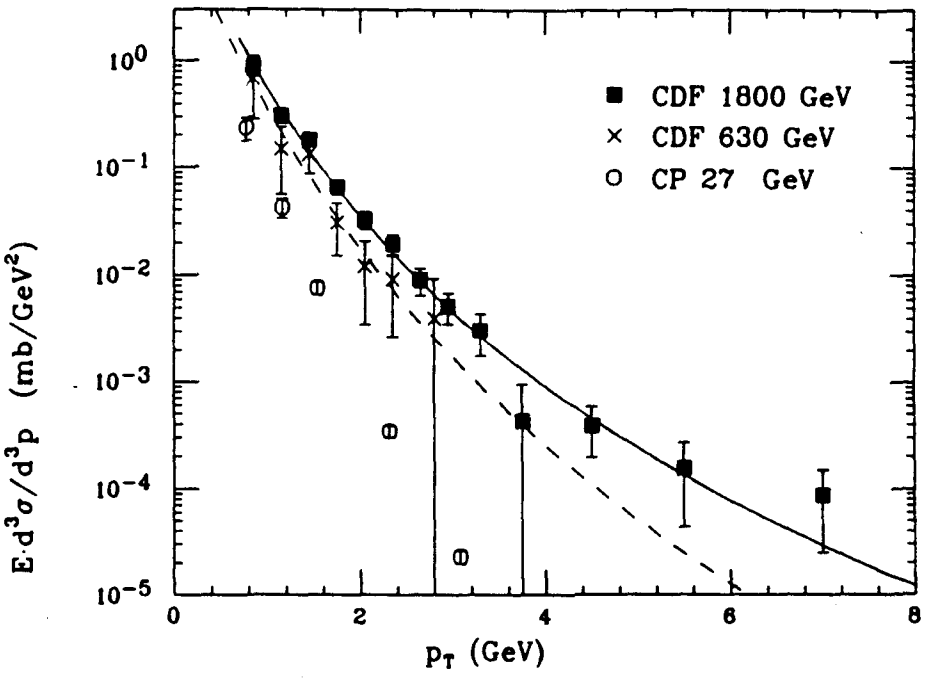

Figure 8.2

Inclusive cross sections for K_s^0 in rapidity $|y| < 1.0$—CDF 1800 GeV, CDF 630 GeV, CP (y=0) charged kaon data, and fits to CDF 1800 GeV data and to UA5 546 GeV data.

Table 8.2

Inclusive cross-section in $|y| < 1$ for K_s^0 in proton-antiproton collisions at a c.m. energy of 1800 GeV, and its statistical uncertainty.

p_T (GeV)	$Ed^3\sigma/d^3p$ (mb/GeV^2)		
0.85	0.9	$\pm$	0.2
1.15	0.31	$\pm$	0.05
1.45	0.18	$\pm$	0.02
1.75	0.065	$\pm$	0.009
2.05	0.032	$\pm$	0.006
2.35	0.019	$\pm$	0.004
2.65	0.009	$\pm$	0.002
2.95	0.005	$\pm$	0.002
3.30	0.003	$\pm$	0.001
3.75	0.0004	$\pm$	0.0005
4.50	0.0004	$\pm$	0.0002
5.50	0.0002	$\pm$	0.0001
7.00	0.00009	$\pm$	0.00006

were published in Ref. [14]. This ratio is shown for our 1800 GeV data in Fig. 8.3, along with data from lower energies. To get the CP data points, as above, we have averaged their charged kaon data over positive and negative signs, and to get a charged hadron cross-section from their data we have added up their pion, kaon, and proton data [16], again averaging over positive and negative charges. Also, we have added charged-kaon/charged hadron data at $\sqrt{s} = 53$ GeV from the British-Scandinavian (BS) collaboration [18]. These data are also for $y = 0$, and we have followed the same procedure as with the CP data to calculate the points shown. The data sets all follow remarkably similar trends, hinting that the shape of this ratio curve may be independent of $\sqrt{s}$.

One would also like to look at the ratio of the K^0_s cross-section to the cross-section for charged pions. We can estimate the charged pion cross-section for each bin using the measured [14] charged hadron cross-section and fits to our K^0_s cross-section, as follows. We know that charged hadrons consist primarily of charged pions, kaons, and protons. Let h be the charged hadron cross-section for a given p_T value, averaged over positive and negative charges, and similarly for π and p. Then

$$h = \pi + K + p.$$

We can naïvely assume that the charged kaon cross-section averaged over charges is the same as the K^0_s cross-section that we measure. For the proton contribution, we will assume that the K/p ratio is 1.48, as estimated from data from the UA2 collaboration [19]. Our estimate of the pion contribution is relatively insensitive to the value we choose for K/p, since kaons typically make up only about 10% of

the charged hadrons, and protons somewhat less. With these assumptions, we may write

$$h = \pi + K + p = \pi + (1 + \frac{1}{1.48})K,$$

or

$$\pi = h - (1 + \frac{1}{1.48})K.$$

Using this formula to estimate the charged pion cross-section in each bin, we obtain Figure 8.4. Data from the CP and BS collaborations (from the same papers cited above) are also shown. Once again, our data are consistent with the ratio growing with p_T in the same way as happens at lower $\sqrt{s}$.

Thermodynamic models [20] [21] predict that particle spectra should follow falling exponentials in transverse mass, $m_T \equiv \sqrt{p_T^2 + m^2}$, where the slope of the exponential is related to the temperature of the hadronic fireball from which particles are emitted. If thermal equilibrium obtains, then, one would expect that the ratios of invariant cross-sections for various species of particles would be constant as a function of m_T. We can check this hypothesis for K_s^0 and pions, using the same ansatz as before to estimate the pion cross-section. (It is easy to show, by the way, that $m_T dm_T = p_T dp_T$, so to get the cross-section as a function of m_T we can use Eq. 7.2 with $p_T dp_T$ replaced by $m_T dm_T$.) The result is shown in Fig. 8.5. Our data are consistent with the ratio $K_s^0/((\pi^+ + \pi^-)/2)$ being constant as a function of m_T.

8.2 The K_s^0 Spectrum in Three Multiplicity Bins

It is interesting to consider the differences betweeen spectra for particles pro-

duced in various ranges of multiplicity. Unfortunately, the largest particle sample we have contains only around 450 K^0_s, and the others contain far too few particles to allow us to subdivide them without losing all statistical significance. We have stretched the statistical power of the 1800 GeV K^0_s spectrum as far as we think prudent by dividing the 1800 GeV event sample roughly into thirds, according to the multiplicity of primary charged tracks as measured by the VTPC in $|y| < 3$. The spectrum for each of the three multiplicity ranges is shown in Fig. 8.6, along with fit results for the three spectra. The data points are given in Table 8.3. Due to the sparseness of the data, not all multiplicity bins have one or more K^0_s in every p_T bins. Note that for clarity in the figure, we have multiplied the spectrum for the middle multiplicity bin by 10 and the spectrum for the high multiplicity bin by 100. The statistical uncertainties prevent us from saying definitively whether the shape of the spectrum is any different for the three bins.

8.3 The $\Lambda + \bar{\Lambda}$ Spectrum

The corrected, background-subtracted inclusive cross-section for Λ and $\bar{\Lambda}$ production at $\sqrt{s} = 1800$ GeV is shown in Fig. 8.7. Note that the cross-section we present is the sum, not the average, of the cross-section for Λ production and that for $\bar{\Lambda}$ production. The solid line in the figure is a fitted exponential; the results of the fit will be discussed in Chapter 9. The data points in the figure are tabulated in Table 8.4. Unfortunately, because of the large statistical uncertainties, we have little information about the shape of the spectrum.

We can plot the ratio of the cross-section for Λ production to that for K^0_s production as a function of p_T or m_T, and these are shown in Figures 8.8 and 8.9.

Table 8.3

Invariant cross-section for K_s^0 in three bands of observed charged multiplicities. Dashes indicate empty bins.

$Ed^3\sigma/d^3p$ (mb/GeV^2)			
p_T (GeV)	$4 \leq N_{ch}^{VTPC} \leq 14$	$15 \leq N_{ch}^{VTPC} \leq 27$	$28 \leq N_{ch}^{VTPC}$
0.85	0.5 ± 0.1	0.9 ± 0.2	1.0 ± 0.4
1.15	0.12 ± 0.03	0.21 ± 0.05	0.5 ± 0.1
1.45	0.04 ± 0.01	0.12 ± 0.02	0.35 ± 0.05
1.75	0.016 ± 0.006	0.05 ± 0.01	0.11 ± 0.02
2.05	0.007 ± 0.003	0.028 ± 0.008	0.05 ± 0.01
2.35	0.007 ± 0.003	0.009 ± 0.004	0.04 ± 0.01
2.65	0.001 ± 0.001	0.006 ± 0.003	0.017 ± 0.006
2.95	—	0.002 ± 0.001	0.013 ± 0.005
3.30	—	—	0.005 ± 0.003
4.25	0.0003 ± 0.0002	0.004 ± 0.002	0.0005 ± 0.0005
6.50	—	0.0005 ± 0.0005	0.0002 ± 0.0001

Note that in these ratio plots, we have averaged the Λ and $\bar{\Lambda}$ cross-sections, so that the ratio plotted is $(\Lambda + \bar{\Lambda})/2/K^0_s$. The average value of the ratio over the p_T range covered is about 0.4, while in the m_T plot the average is about 0.5.

Table 8.4

Inclusive cross-section in $|y| < 1$ for Λ and $\bar{\Lambda}$ in proton-antiproton collisions at a c.m. energy of 1800 GeV.

p_T (GeV)	$Ed^3\sigma/d^3p$ (mb/GeV^2)		
1.45	0.07	$\pm$	0.03
1.75	0.03	$\pm$	0.02
2.05	0.06	$\pm$	0.01
2.35	0.025	$\pm$	0.009
2.65	0.007	$\pm$	0.005
2.95	0.002	$\pm$	0.001
3.3	0.004	$\pm$	0.003
4.25	0.0004	$\pm$	0.0003
6.5	0.00005	$\pm$	0.00005

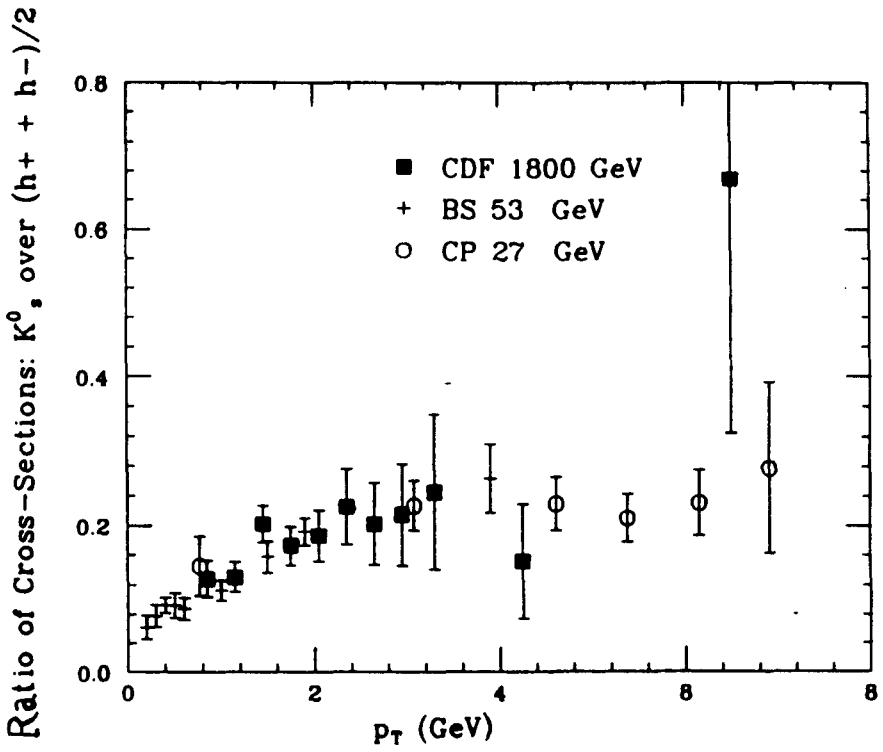

Figure 8.3

Ratio of cross section for K^0_s to that for charged hadrons: CDF, BS, and CP collaborations.

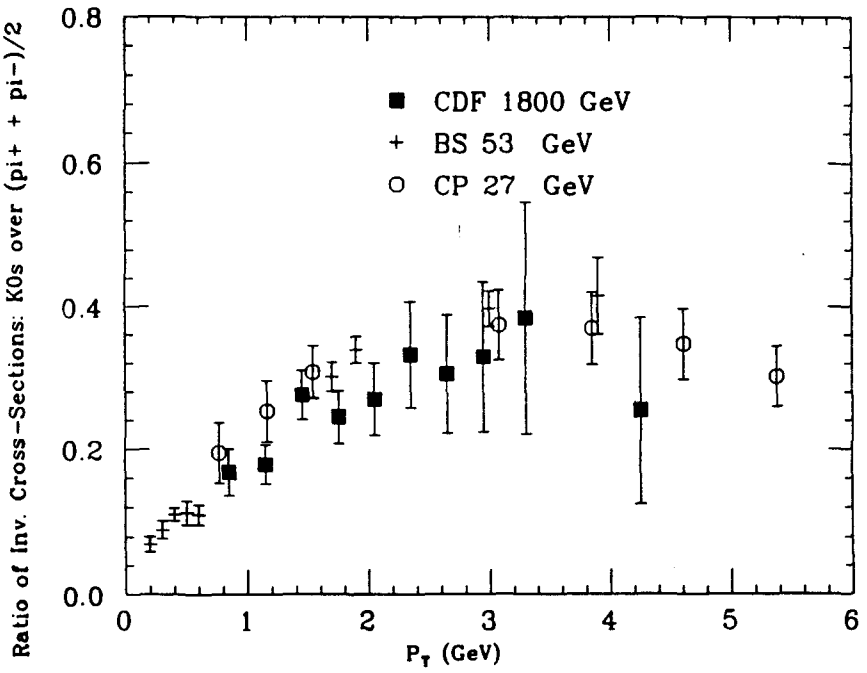

Figure 8.4

Ratio, as a function of p_T, of cross section for K_s^0 to that for charged pions: CDF, BS, and CP collaborations.

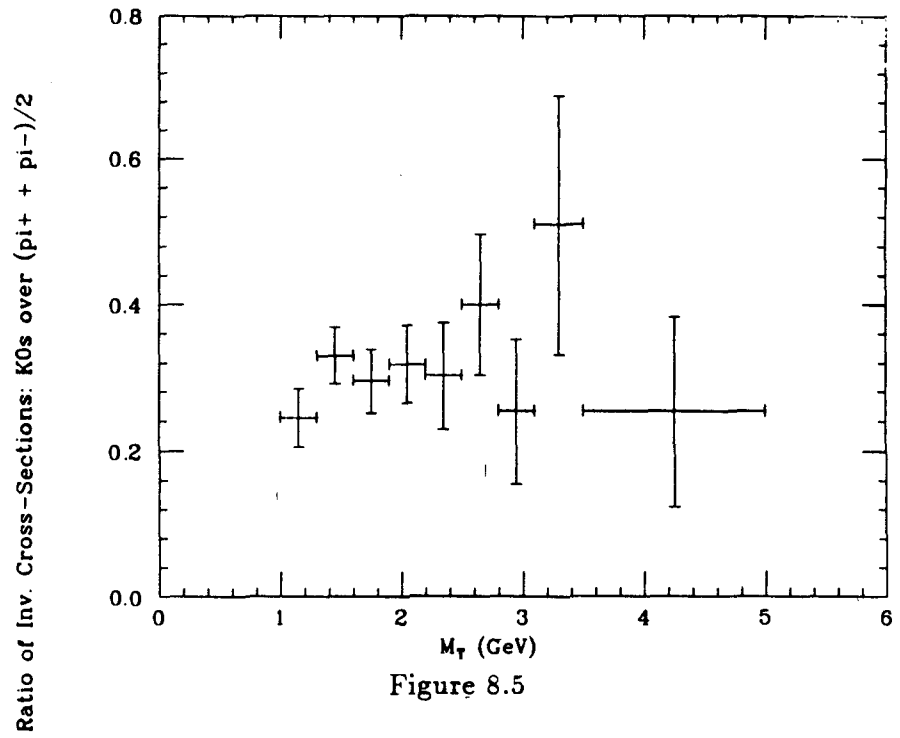

Figure 8.5

Ratio, as a function of m_T, of cross section for K_s^0 to that for charged pions

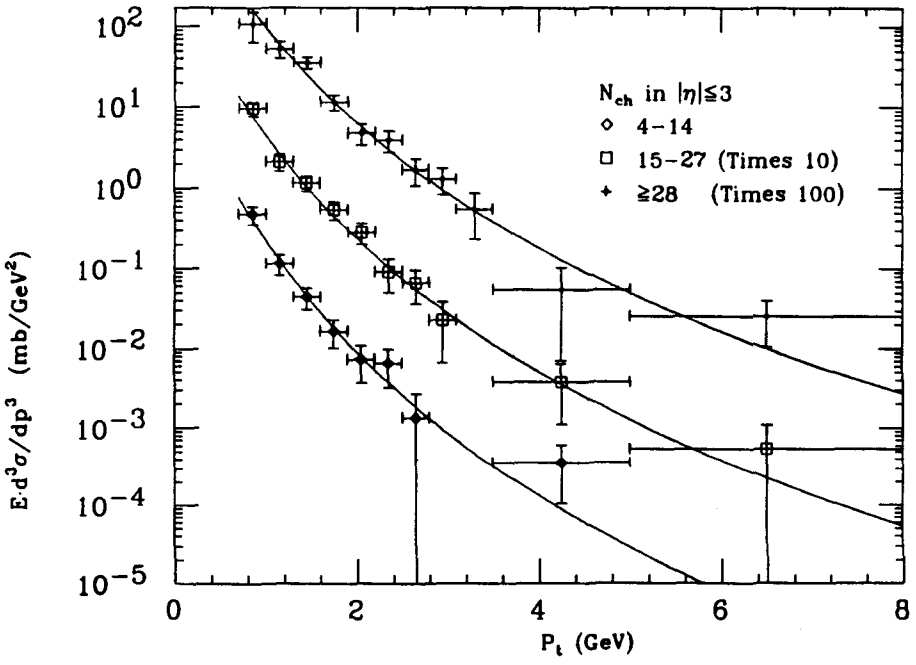

Figure 8.6

Invariant cross-section for K_s^0 in three bands of observed charged multiplicities.

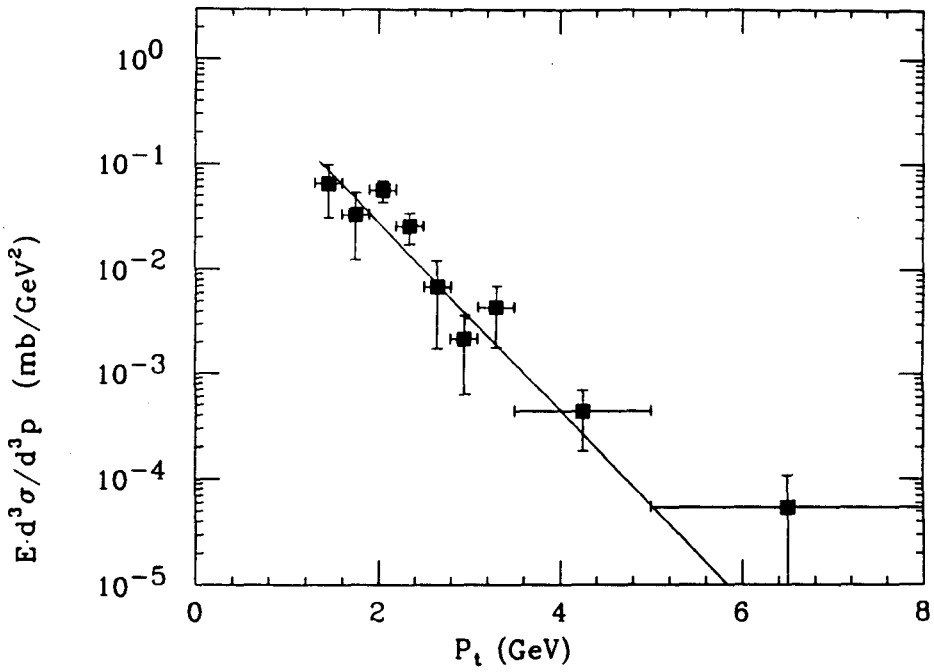

Figure 8.7

Inclusive cross-section in $|y| < 1$ for Λ and $\bar{\Lambda}$ in proton-antiproton collisions at a c.m. energy of 1800 GeV.

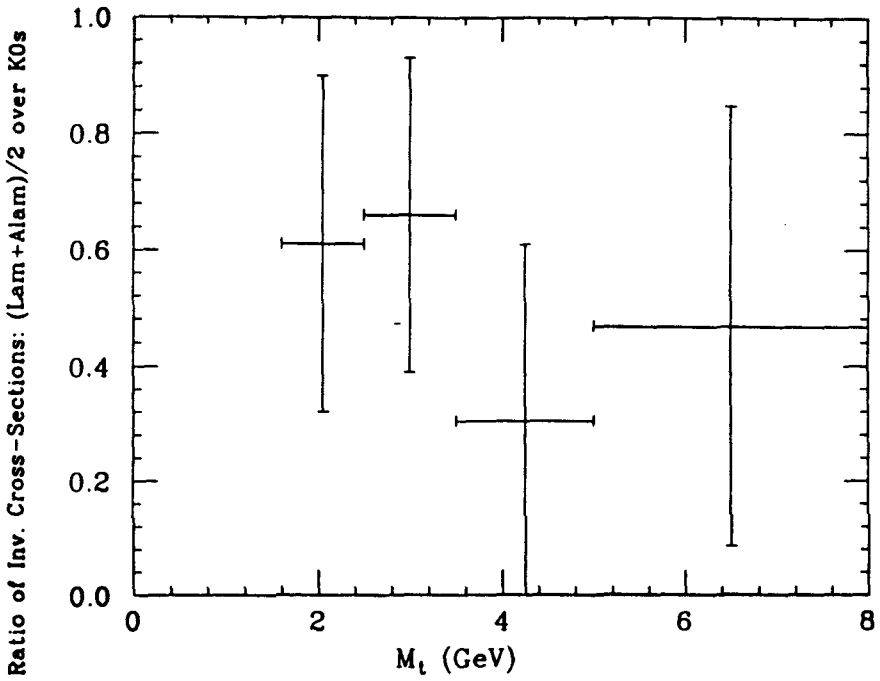

Figure 8.9

Ratio of cross sections: $(\Lambda+\bar{\Lambda})/2$ over K^0_s, as a function of m_T,in proton-antiproton collisions at a c.m. energy of 1800 GeV.

9. FITTING THE SHAPES OF THE SPECTRA

Fitting functions to our spectra provides a simple way to compare our results to those obtained at lower energies. Also, fitted functions allow us to extrapolate the spectrum below the minimum p_T values at which we can find K^0_s and Λ, which is necessary to estimate the mean p_T and the central rapidity density for K^0_s.

A number of functional forms have been used by other experiments; perhaps the most common in the most recent data-is the power-law form used by UA1 [23]:

$$E\frac{d^3\sigma}{d^3p} = A\frac{p_0^n}{(p_T + p_0)^n}.$$

This form works well for various spectra at energies approaching ours (UA1 single-charged-particle data [23], CDF single-charged particle data [14], UA5 K^0_s data [22], etc.), so it is the natural one for comparisons with recent measurements, and it is the form we will focus on. We will also discuss results of fits to several other common forms.

Because of the correction and background-subtraction techniques we employ, it is somewhat tricky to devise a statistically sound fitting algorithm. Three different fitting algorithms have been devised and tested on our 1800 GeV K^0_s data, since it is our largest sample of particles. In the next section, we compare the results from the three and find that they agree well. Next, we discuss fits to alternative functional forms. The fitting algorithms used are detailed in Appendix D.

9.1 Comparison Betweeen the Results of Different Algorithms

Some bins of our K^0_s spectra are sparsely populated, particularly at high p_T, and we want to be sure that we treat these bins in a statistically sound way, so that we get the correct covariance matrix on the fit parameters. We have an algorithm (hereafter called the "naive" fit) that fits the spectrum by minimizing a χ^2 that assumes Gaussian errors. In addition, Virgil Barnes and Franco Bedeschi have devised two algorithms that maximize likelihood functions based on Poisson statistics. The first of these uses distributions of the data in p_T, averaging over the N_{ch}^{CTC} dimension of the efficiency corrections, so we refer to this fit as the "1-dimensional Poisson" fit. The second Poisson fit uses distributions of the data in two dimensions—N_{ch}^{CTC} and p_T. Table 9.1 shows a comparison of the parameters of the above functional form for the various fits for the 1800 GeV K^0_s data, with p_0 fixed at 1.3 GeV (the reason for fixing p_0 is discussed in the next section).

Table 9.1

Comparison of fit results of the various algorithms for the 1800 GeV K^0_s data.

Algorithm	A	n	χ^2	N_{dof}
Gaussian	45 ± 9	7.7 ± 0.2	8.1	11
1-dim Poisson	40 ± 7	7.5 ± 0.2	8.6	11
2-dim Poisson	42 ± 8	7.7 ± 0.2	71	97

It will be seen that the values of the fit parameters and errors are very similar

for all the fits. The errors on the fit parameters from the Gaussian fit are somewhat more conservative than the others, and the Gaussian fit is by far the simplest, so in what follows, we use the Gaussian fitting algorithm exclusively.

9.2 Fit Results for Power-Law Fits to the K_s^0 Spectrum

A common way to compare the sharpness of fall of our spectra to data taken at lower energies is to compare the values of n obtained by fitting the above power-law form to the cross-section data. Because p_0 and n are highly correlated, in order to make such a comparison meaningful, one must fix p_0 to some value. The value of p_0 used by UA1, UA5 and CDF ([23], [22], [14]) is 1.3 GeV, so that is the value we adopt. Also, we have been unable to obtain a stable fit when we allow p_0 to vary, which is probably a consequence of the low-p_T cutoff and the limited statistics of our data.

The results of such a fit for our K_s^0 data are given in Table 9.2. The curves defined by the fit results are shown in Fig. 8.1. Unfortunately, n is poorly determined by the 630 GeV data, and the difference between the n values at 630 and 1800 GeV is not statistically significant. Even for the 1800 GeV data, the uncertainty on n is sufficiently large that the differences between our n values and those obtained by the UA5 collaboration [22] at 200, 546, and 900 GeV, are not statistically significant.

9.3 Fit results for Fits of Other Functional Forms to the 1800 GeV K_s^0 Spectrum

Various theories have predicted a number of functional forms for hadron inclusive p_T distributions. In order to see whether our 1800 GeV K_s^0 data allow us to

Table 9.2

Results of fits of the power-law form for the K_s^0 data.

$\sqrt{s}$ (GeV)	A (mb/GeV^2)	n	χ^2/N_{dof}
630	37 ± 33	8.2 ± 1.1	2.2/6
1800	45 ± 9	7.7 ± 0.2	8.1/11

rule out any particular form, we have used the Gaussian fitting algorithm to fit several of the most popular forms. Table 9.3 compares the quality of the fits, and Figures 9.1-9.3 show the fit parameters and fitted curves. It appears that we can't really distinguish between the power-law and the exponential fits simply on the basis of χ^2.

The last form in Table 9.3 is a prediction of the Constituent Interchange Model (CIM) [24]. In addition to the explicit p_T dependence of the denominator, the numerator contains the variable $x_T \equiv 2p_T/\sqrt{s}$. Because our $\sqrt{s}$ value is so large compared to the p_T range covered by our measurement, our data cover only a small range of x_T, so the fit has essentially no power to determine the exponent m. In fact, if m is a free parameter in the fit, the χ^2 minimization favors very large values of m ($m > 1000$, even!), so we have fixed m at 10, the value predicted by the CIM. The exponents m and n are only very weakly correlated, so we get nearly the same value of n when we leave m free as when we do not. It is interesting to note that n turns out to be 4.4 ± 0.08, in rough agreement with a prediction of the CIM. Naively, one might expect a $1/p_T{}^4$ behavior simply from the Rutherford

scattering formula. In the CP data, typical values of n were more like 8 [16], which is the value predicted by the CIM. The transition between p_T^{-8} behavior and p_T^{-4} behavior is expected in the context of QCD [25]. Given the rather poor quality of the fit, however, ($\chi^2/N_{dof} \approx 3$), one must not take these tempting speculations too seriously.

Table 9.3

Fit quality for fits of alternative functional forms to the 1800 GeV K_s^0 spectrum.

Functional Form	χ^2	N_{dof}
$Ap_0^n/(p_0+p_T)^n$	8.1	11
Ae^{-bp_T}	11.4	11
Ae^{-cm_T}	12.8	11
$A(1-2p_T/\sqrt{s})^{10}/p_T^n$	31	11

9.4 Fit results for 1800 GeV K_s^0 Spectra in Multiplicity Bins

We have fitted the UA1-style power law (with p_0 fixed at 1.3 GeV) to the spectra presented in Section 8.2, and the results are shown in Table 9.4. As expected, the statistical significance of the difference in n between the three spectra is poor.

9.5 Fit results for the $\Lambda + \bar{\Lambda}$ Spectrum

The results of fits of several forms to the $\Lambda + \bar{\Lambda}$ spectrum are shown in Figures 9.4-9.6. Once again, we cannot reasonably rule out any of the forms on the basis of χ^2.

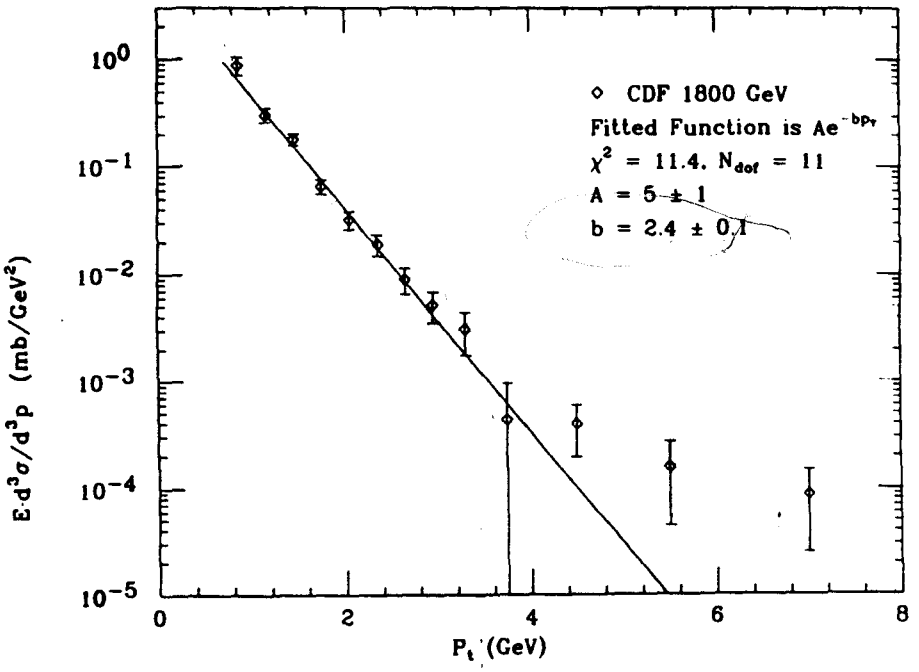

Figure 9.1

1800 GeV K_s^0 data and results of fit to an exponential in p_T.

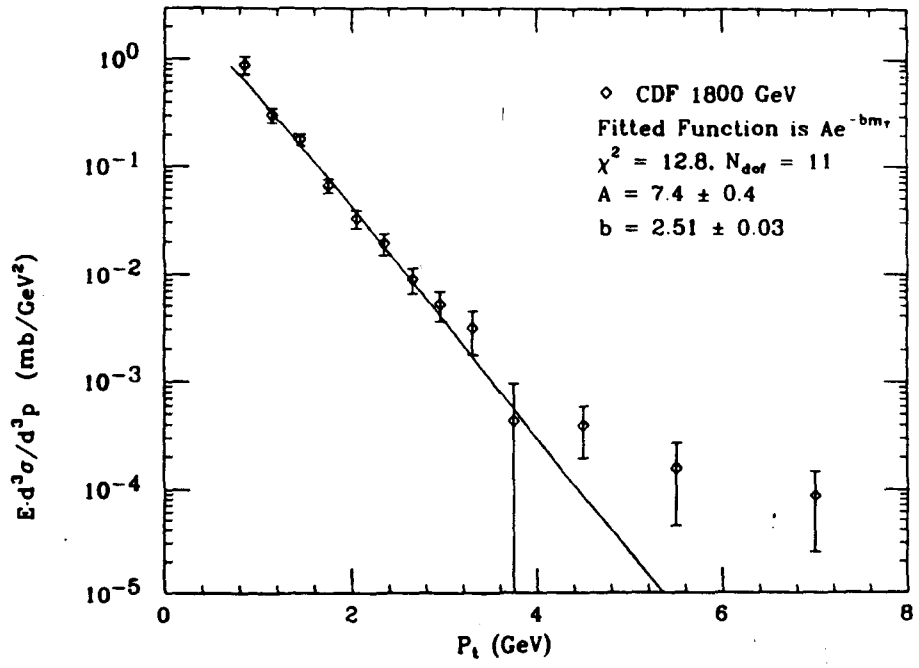

Figure 9.2

1800 GeV K_s^0 data and results of fit to an exponential in m_T.

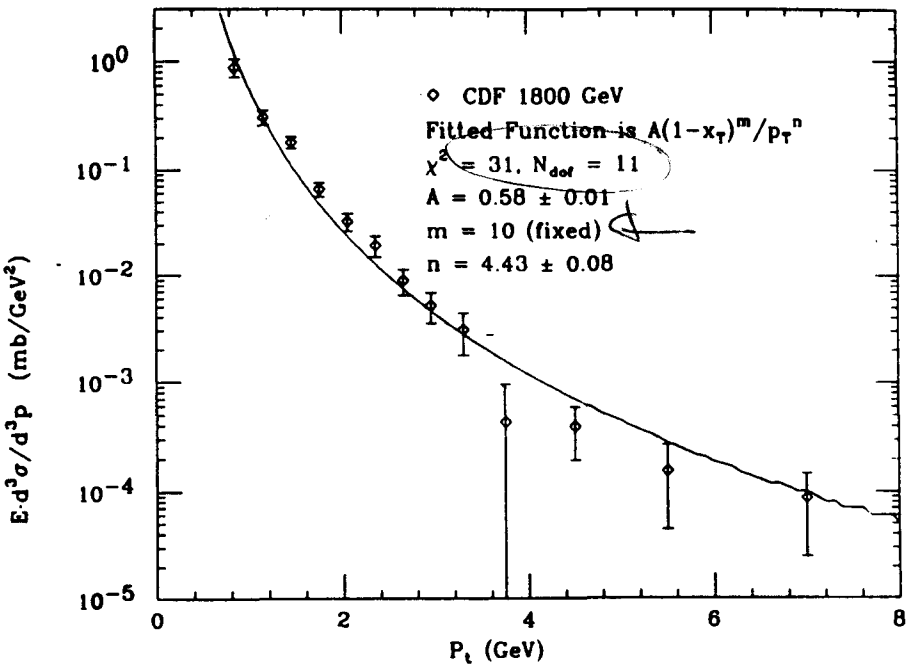

Figure 9.3

1800 GeV K_s^0 data and results of fit to a power-law form predicted by Berman, et al.

Table 9.4

Results of fits of the power-law form for the 1800 GeV K_s^0 data subdivided by VTPC multiplicity.

Charged Multiplicity in Event	A (mb/GeV^2)	n	χ^2/N_{dof}
$4 \leq N_{ch}^{VTPC} \leq 14$	36 ± 10	8.9 ± 0.8	2.4/6
$15 \leq N_{ch}^{VTPC} \leq 27$	45 ± 15	8.1 ± 0.4	4/8
$28 \leq N_{ch}^{VTPC}$	69 ± 20	7.5 ± 0.3	11/9

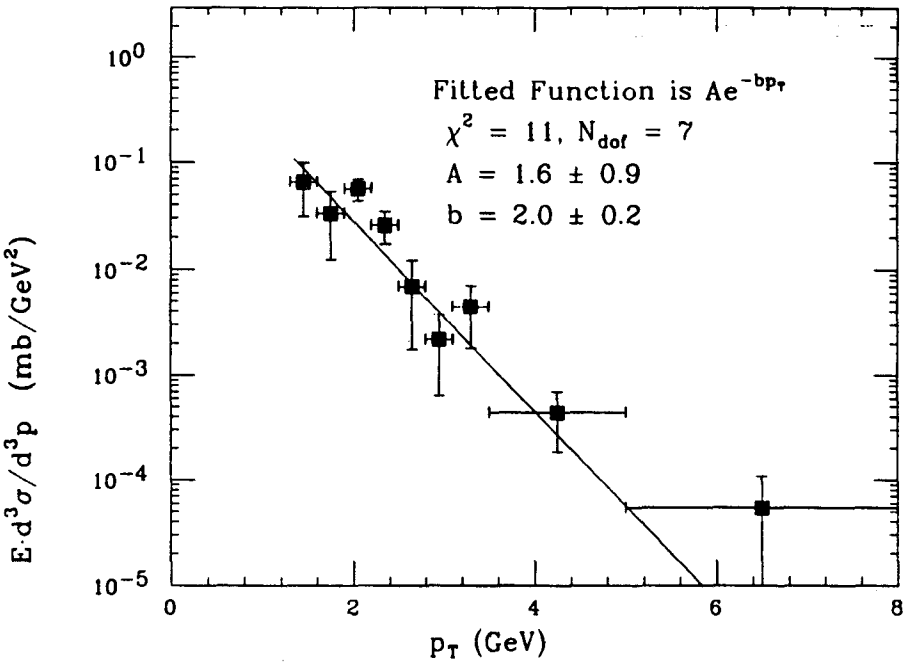

Figure 9.4

1800 GeV $\Lambda + \bar{\Lambda}$ data and results of fit to an exponential in p_T.

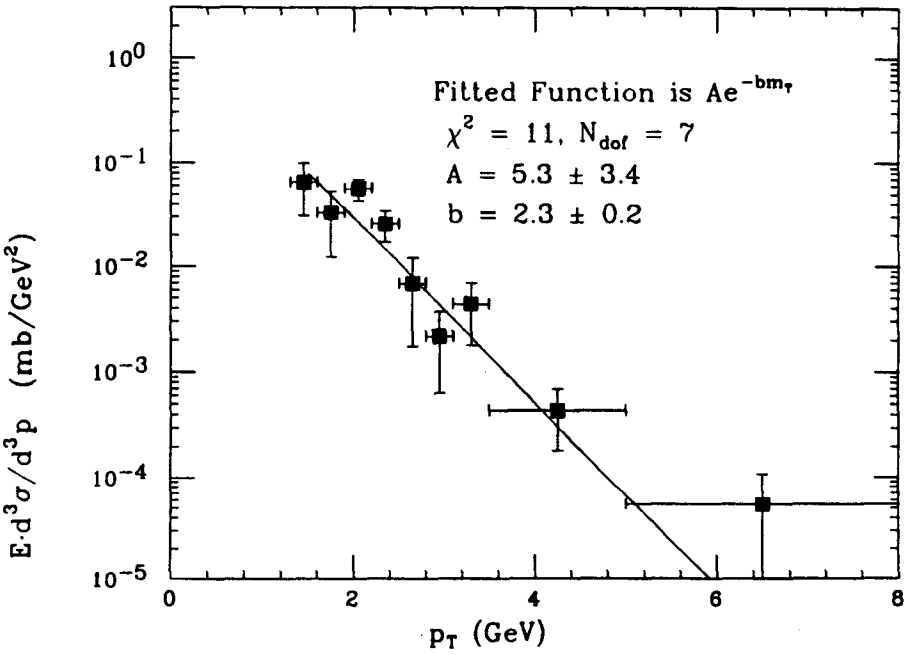

Figure 9.5

1800 GeV $\Lambda + \bar{\Lambda}$ data and results of fit to an exponential in m_T.

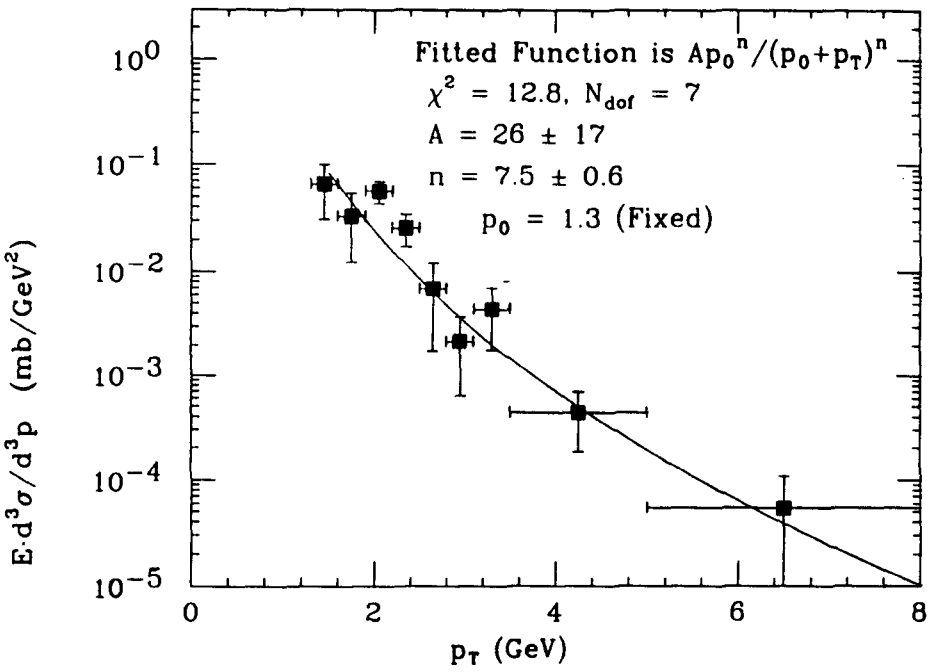

Figure 9.6

1800 GeV $\Lambda + \bar{\Lambda}$ data and results of fit to a UA1-style power-law form.

10. GENERAL CONSIDERATIONS FOR QCD-BASED MODELS OF PROTON-ANTIPROTON COLLISIONS

In the next chapter, we will compare our measured spectra to the predictions of several models. In order to clarify the issues involved in the formulation of such models and to introduce some terminology used in the next chapter, we review here the ingredients of proton-antiproton collisions vis-a-vis the Standard Model.

As mentioned in Chapter 1, in the Standard Model, protons and antiprotons are composite objects. When a proton collides with an antiproton, the collision may be viewed as an interaction among the constituents of the proton with those of the $\bar{p}$. Sometimes these subprocess collisions will be "hard", meaning that they involve a large transfer of momentum among the constituents or "partons" involved in the collision, and sometimes the $p\bar{p}$ collision will be "soft", not involving any hard subprocess. As we have mentioned, the hard subprocesses are calculable in perturbative QCD, while soft collisions are not. Therefore, models of $p\bar{p}$ collisions usually include two components—a pertubative-QCD treatment of the hard scattering processes, and a somewhat more ad-hoc treatment of soft collisions. In addition, these models must include a mechanism for the transition from the partons in the subprocess final state to the hadrons that form the experimentally-observable final state.

Perturbative QCD tells us how to calculate the hard subprocesses, in which

both the inputs and the end products are quarks and gluons. Now, isolated quarks and gluons are never seen in nature, due to a property of the strong force known as "confinement"; instead, most of the particles we see coming out of a $p\bar{p}$ collision are hadrons. Models of $p\bar{p}$ collisions must treat the process by which hadrons are created out of the quarks and gluons coming out of the subprocess collision, known as "hadronization" or "fragmentation". Hadronization, too, is not readily calculable in perturbative QCD.

The partons taking part in the subprocess collision may be quarks, antiquarks, or gluons. The proton is composed of three "valence" quarks (two up quarks and a down quark), and gluons, the particles that mediate the strong force that holds the proton together. Gluons may split into virtual quark-antiquark pairs, so, in addition to the up and down quarks, the proton contains a "sea" of virtual quarks and antiquarks, which may have any of the six flavors. Similarly, the antiproton is made of two anti-up-quarks and one anti-down-quark, plus gluons and a sea of quarks and antiquarks.

The simplest QCD subprocesses are those that have two partons as input and two partons as output, the "2 $\rightarrow$ 2" processes. These include $qq \rightarrow qq$, $q\bar{q} \rightarrow q\bar{q}$, $q\bar{q} \rightarrow gg$, $gq \rightarrow gq$, $g\bar{q} \rightarrow g\bar{q}$, $gg \rightarrow q\bar{q}$, and $gg \rightarrow gg$. The simplest Feynman graphs for these processes have quantum-mechanical amplitudes that are "second order" in α_S, the strong-force coupling constant. Each of these processes may also proceed through any one of an infinite number of more complicated graphs of higher order in α_S. In modeling $p\bar{p}$ collisions, one must decide whether to include only the 2 $\rightarrow$ 2 processes or more complicated processes involving three or more

partons in the final state, and one must decide to what order in α_S to calculate the processes that one does include.

The cross-section for each subprocess depends on the 4-momenta of the partons in the initial state. The momenta of partons in protons and antiprotons are distributed according to functions that are characteristic of the structure of the proton and are therefore known as "structure functions". The proton structure function for a given parton depends on the flavor of the parton, the fraction x of the longitudinal momentum of the proton that is carried by the parton, and Q, the 4-momentum transfer of the subprocess. These functions are measured in deep-inelastic lepton-hadron scattering experiments. It is difficult to measure structure functions at small x, so the measured functions must be extrapolated to very small x. The way that this extrapolation is done may strongly affect predictions for min-bias events, where the typical x is in fact small. A number of parametrizations and fits of structure functions are available.

As mentioned, fragmentation is not calculable in perturbative QCD, because the energy scales involved are of the order of the masses of the light hadrons, and α_S is not small in this regime. So-called fragmentation functions give the probability of producing a hadron of a given species carrying a given fraction of the momentum of a given fragmenting parton. Some fragmentation functions have been measured in e^+e^- collisions and deep inelastic lepton-hadron scattering. Fragmentation functions do not tell the whole story of the hadronization process, though, for a number of reasons—for one thing, they neglect any influence on the fragmentation of one parton due to other partons. For this reason, Monte Carlo

implementations of fragmentation models, like the Lund string model [26] have been developed.

Some of the hadrons produced by the fragmentation process will in general be resonances, short-lived particles that decay via the strong force into lighter hadrons. Many resonances decay into K^0_s or Λ, and in our analysis we have made no attempt to distinguish direct production of K^0_s and Λ from the production due to resonance decays, nor from weak or electromagnetic decays of Ξ, Ω^-, or Σ^0. All the models with which we will compare our measurements take resonance decays into account in one way or another.

The fragmentation process may be thought of as a parton cascade in which quarks undergo bremsstrahlung and emit gluons, which turn into quark-anti-quark pairs, which may emit more gluons, etc. Because the strange quark is heavier than the up and down quarks, and other quarks are heavier still, one might expect the production of strange-anti-strange pairs in the cascade to be suppressed relative to that of up-anti-up or down-anti-down pairs, as discussed in Chapter 1. This suppression may be characterized by a factor λ, which reflects the ratio of the relative probability of a gluon splitting into a strange-anti-strange pair to that for splitting into an up-anti-up or down-anti-down pair, or alternately, the probability of producing a strange quark from the vacuum relative to that of producing an up or down quark. Statistical quark models [27] [28] predict the relative yields of K^0_s and charged pions in terms of λ, including the effects of resonance decays, and we can estimate this ratio from our measured spectra and calculate λ using the models.

11. COMPARING THE SPECTRA TO THE PREDICTIONS OF MODELS

In this chapter, we compare some of our measurements to the predictions of several models of $p\bar{p}$ collisions, including a simple QCD-based model by Ellis and Stirling and two of the Lund Monte-Carlo programs—Pythia and Fritiof. All the models we discuss here have been implemented as computer programs. Two of them, Pythia and Fritiof, have many adjustable parameters, and we will note in each case the values to which the most important variables were set. The data set with the most statistical power to make such comparisons meaningful is our 1800 GeV K_s^0 data.

11.1 The QCD-based Model of Ellis and Stirling

S.D. Ellis and W.J. Stirling have prepared a program [29] that implements a very simple QCD-based model of $p\bar{p}$ interactions. This program does a Monte-Carlo integration convolving first-order QCD $2 \rightarrow 2$ cross sections with structure functions and fragmentation functions to produce inclusive hadron spectra. We have run the program with $\Lambda_{QCD} = 0.2$ GeV, with the q^2 scale set to the p_T^2 of the parton subprocess, MRS set 2 structure functions (BCDMS fit, $\Lambda_{QCD} = 0.2$ GeV, "soft" gluon structure functions) [30] and Owens fragmentation functions [31]. In Fig. 11.1, the solid curve is the power-law fit to our 1800 GeV K_s^0 data, and the stars are the results from the program. The vertical scatter of points from the Ellis/Stirling program gives an indication of the statistical uncertainties involved

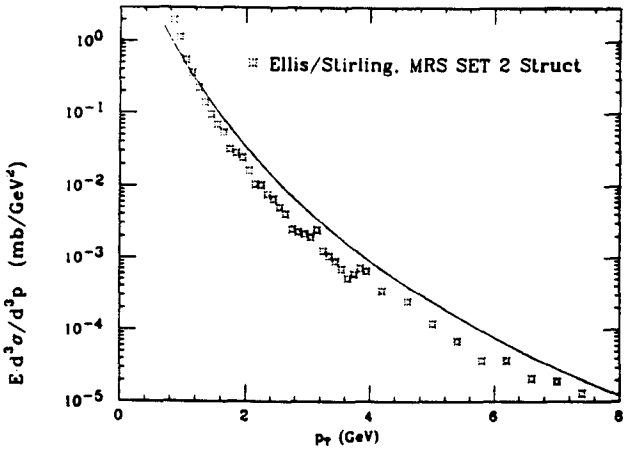

Figure 11.1

A fit to our 1800 GeV K_s^0 spectrum and predictions of a QCD-based model of Ellis and Stirling with MRS set 2 structure functions.

in the Monte Carlo integration. The program gives results that are systematically lower than our data at high p_T, which in part may be attributed to the fact that first-order QCD matrix elements are used, but, except perhaps at low p_T, the shape is predicted rather well. We have run the program with several different sets of structure functions; the results of using MRS set 1 (EMC fit, $\Lambda_{QCD} = 0.1$ GeV) and EHLQ set 1 [32] are representative and are shown in Figures 11.2 and 11.3.

Figure 1.4 shows the ratio $K_s^0/((h^+ + h^-)/2)$ as a function of p_T for our 1800 GeV data and for the Ellis/Stirling program run with MRS set 2 structure functions. Again, the vertical scatter of the Ellis/Stirling points can give us a feeling for the size of the statistical errors. The Ellis/Stirling program predicts that the ratio should be fairly constant with p_T, with an average value of 0.15 or so, which is not inconsistent with our data.

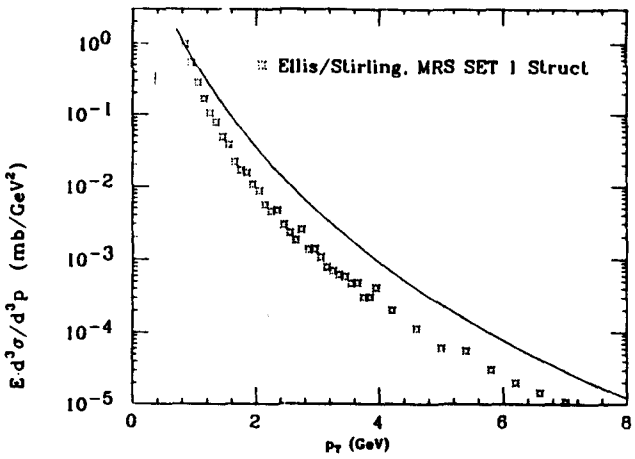

Figure 11.2

A fit to our 1800 GeV K_s^0 spectrum and predictions of a QCD-based model of Ellis and Stirling with MRS set 1 structure functions.

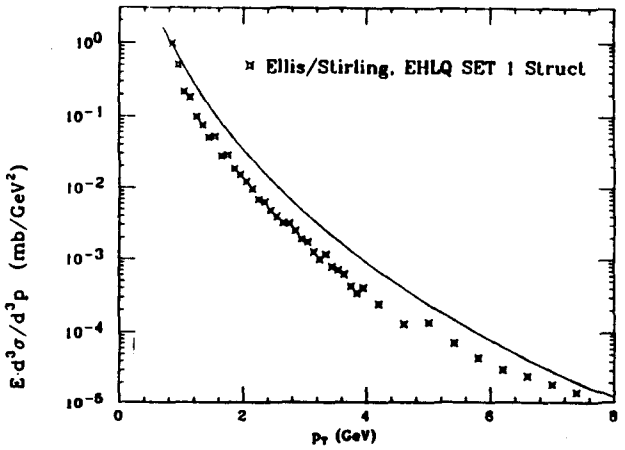

Figure 11.3

A fit to our 1800 GeV K_s^0 spectrum and predictions of a QCD-based model of Ellis and Stirling with EHLQ set 1 structure functions.

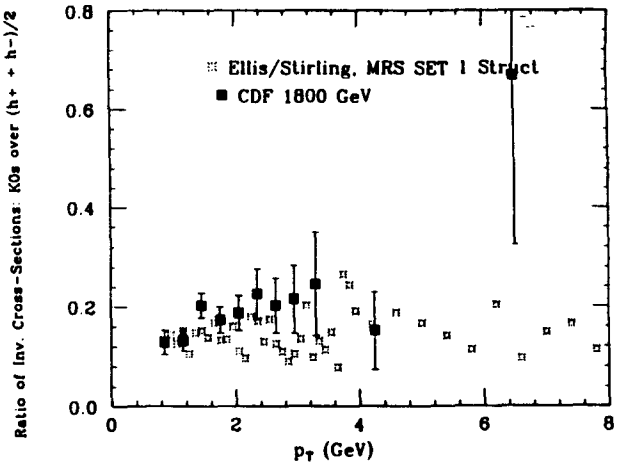

Figure 11.4

Comparison of our 1800 GeV K^0_s-to-charged-hadron ratio versus predictions of a QCD-based model of Ellis and Stirling.

Unfortunately, the program as supplied to us did not include fragmentation functions for Λ, so we are unable to make a comparison to our Λ data.

11.2 The Pythia Monte Carlo Program

Rather than doing a Monte Carlo integration to calculate inclusive cross sections, the Pythia [33] program uses Monte Carlo techniques to generate individual events. The output for an individual event consists of a list of the particles produced, including their species and momenta. Short-lived resonances produced are decayed randomly according to correct branching fractions and kinematic distributions, so that the output particle list includes both directly- and indirectly-produced K^0_s and Λ. We select events that pass the same trigger and event-selection applied to our real data sample.

Pythia uses the lowest-order QCD $2 \rightarrow 2$ cross-sections, and includes initial- and final-state radiation using a parton-cascade approach. Fragmentation is modeled via the Lund String Model [26], as implemented by the JETSET fragmentation routines [34]. Pythia includes a framework [35] for generating collisions where more than one parton-parton collision takes place. In addition to hard-scattering processes, Pythia can also generated single-diffractive and double-diffractive events.

The Pythia program has many options for the user to chose from. We have chosen a set recommended in Ref. [35], as follows: We have set the p_T lower limit for hard-scattering processes at 2.0963 GeV for $\sqrt{s}$ = 1800 GeV and 2.0123 GeV for $\sqrt{s}$ = 630 GeV, as recommended in Ref. [35]. These same values were used for the p_T cutoff for multiple interactions. In order to simulate the effects of higher-order QCD subprocesses, a prescription of Ellis and Sexton [36] was used, in which α_S is evaluated at a q^2 value that is a constant fraction of the actual subprocess q^2. For the multiple-interaction scenario, we selected a double-Gaussian matter distribution inside the proton and antiproton.

The K^0_s spectrum generated in this way is shown in Fig. 11.5, along with a fit to our 1800 GeV data. In this and the next several figures, the error bars on the Pythia predictions indicate statistical uncertainties due to the finite size of the Pythia event sample used. Pythia predicts the shape of the spectrum rather well, but predicts a somewhat higher cross-section at high p_T than is indicated by the fit. Referring to Fig. 8.1, however, we note that the error bars in our data at high p_T are considerably larger than the differences between Pythia results and the fit. Figure 11.6 shows the Pythia prediction for the sum of the Λ and

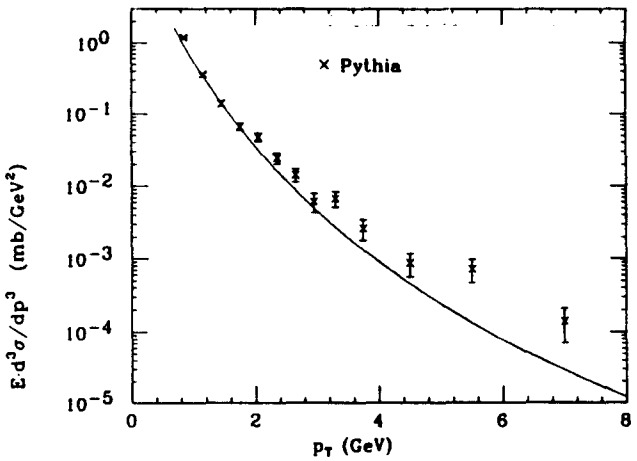

Figure 11.5

Comparison of our 1800 GeV K_s^0 cross section to the predictions of the Pythia Monte Carlo program.

$\bar{\Lambda}$ cross-sections, along with our 1800 GeV data. Again, the Pythia predictions match the data fairly well. Figure 11.7 shows the K_s^0-to-charged-hadron ratio as a function of p_T. Near $p_T = 1$ GeV, the Pythia results are higher than our data by several standard deviations, both because the Pythia prediction for the K_s^0 cross section in this region is somewhat higher than in our data and because the Pythia charged-hadron cross section is somewhat lower than the CDF result of Ref. [14].

11.3 The Fritiof Monte Carlo Program

The Fritiof Monte Carlo program [37] [38] [39] [40] is based on the similarity between the confined color force field of QCD and a vortex line in a Type II superconductor. In this picture, when hadrons collide, the overlap of the color fields generates many disturbances and excitations, and the hadrons exchange momenta

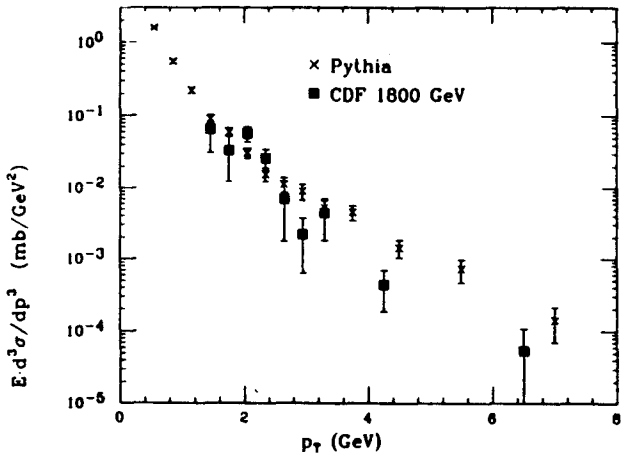

Figure 11.6

Comparison of our 1800 GeV Λ and $\bar{\Lambda}$ cross section to the predictions of the Pythia Monte Carlo program.

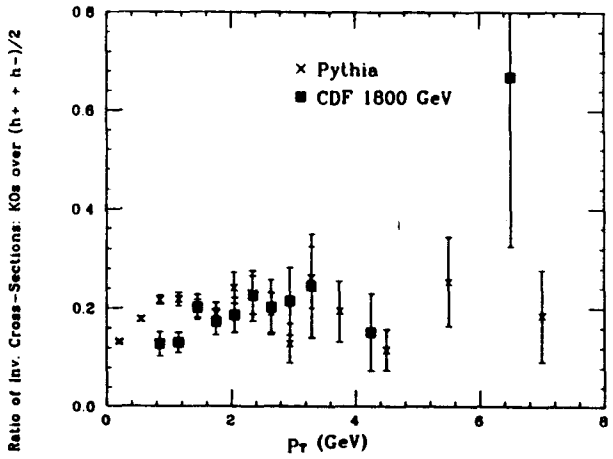

Figure 11.7

Comparison of our 1800 GeV K^0_s-to-charged-hadron ratio to the predictions of the Pythia Monte Carlo program.

through many low-energy collisions between field quanta. The version of the Fritiof program that we use has been extended to treat hard interactions by treating the largest of the momentum transfers as conventional parton-parton collisions, which are then treated as in Pythia. Fritiof has no user-adjustable parameters.

The predictions of the Fritiof program are compared to a fit to our 1800 GeV K_s^0 spectrum in Fig. 11.8. We see that Fritiof predicts cross-section values that are as much as a factor of 2 higher than our fit, and that the shape of the Fritiof prediction diverges from our fit even at moderate p_T values. In Figure 11.9, we see that Fritiof predicts a much larger Λ plus $\bar{\Lambda}$ cross sections than our data indicate. Figure 11.10 shows the ratio, as a function of p_T, of the K_s^0 cross section to that for charged hadrons. Like Pythia, near $p_T = 1$ GeV Fritiof predicts ratio values higher than our data by several standard deviations, both because the Fritiof prediction for the K_s^0 cross section in this region is somewhat higher than in our data and because the Fritiof prediction for the charged-hadron cross section is somewhat lower than the CDF result of Ref. [14].

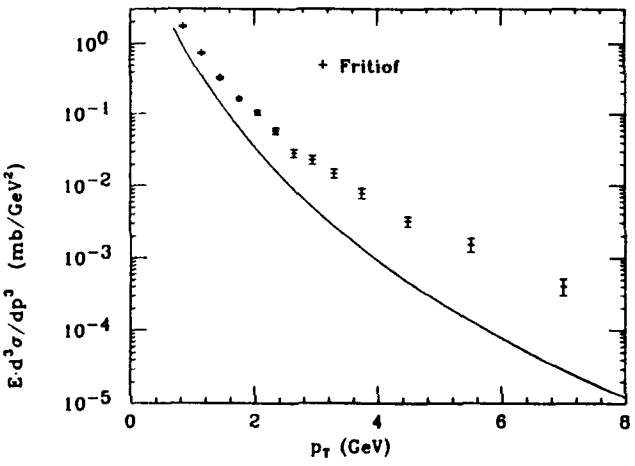

Figure 11.8

Comparison of our 1800 GeV K^0_s cross section to the predictions of the Fritiof Monte Carlo program.

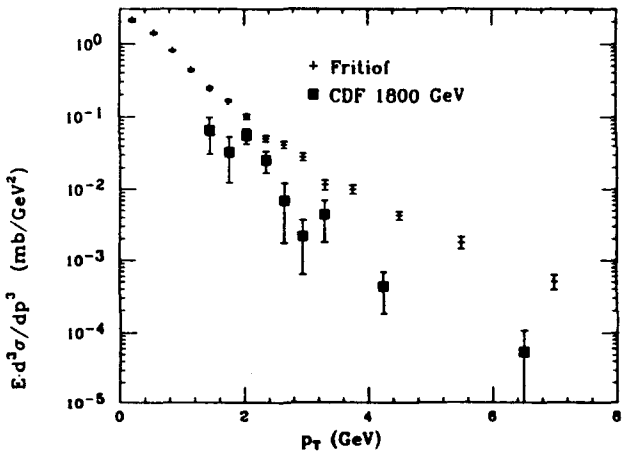

Figure 11.9

Comparison of our 1800 GeV Λ and $\bar{\Lambda}$ cross section to the predictions of the Fritiof Monte Carlo program.

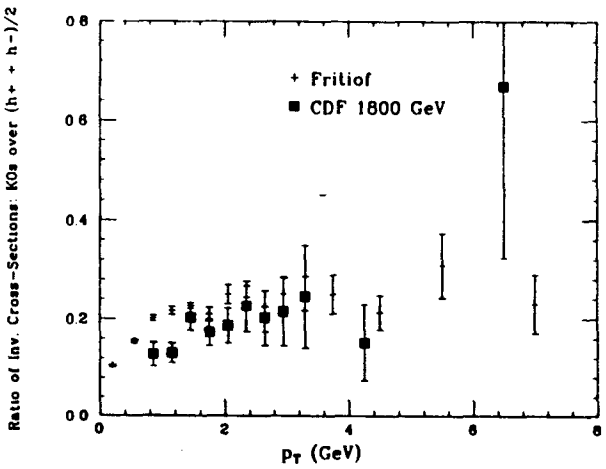

Figure 11.10

Comparison of our 1800 GeV K^0_s-to-charged-hadron ratio to the predictions of the Fritiof Monte Carlo program.

12. MEAN p_T, CENTRAL RAPIDITY DENSITIES, AND THE STRANGENESS-SUPRESSION FACTOR

There are several quantities of physical interest that must be computed by evaluating integrals involving the p_T spectra over all p_T. These include the the central rapidity densities $\rho_K(0) \equiv dN_{K^0_s}/dy \mid_{y=0}$ and $\rho_{\Lambda\bar{\Lambda}}(0) \equiv dN_\Lambda/dy \mid_{y=0} + dN_{\bar{\Lambda}}/dy \mid_{y=0}$ and the mean value of transverse momentum $< p_T >$ for K^0_s and for Λ. In addition, particle ratios like K/π may be derived from the rapidity densities, and the strangeness-suppression factor λ may be derived from particle ratios, as described in Appendix E.

Since we do not measure the spectrum below 0.7 GeV, we must extrapolate. While we cannot distinguish among the several functional forms that we have fit to our 1800 GeV K^0_s data based on χ^2 alone, CDF data on charged-particle production at 1800 GeV [14] favor the power-law form. We will thus assume that the spectrum behaves according to our fitted power-law above some p_T value, and according to some function of our choice below this value, and we will demand continuity of function and of slope at the transition point. We have a great deal of freedom in our choice of the function to use below the cutoff. For that matter, the transition between the power-law and the other functional form need not be precisely at the edge of our measurement range.

Measurements of inclusive particle spectra in hadron collisions usually do not

extend to very low p_T. One ISR experiment [41] that did study spectra at low p_T found that functional form that best described the spectra was an exponential in transverse mass, e^{-bm_T}, where $m_T \equiv \sqrt{{p_T}^2 + m^2}$; also, UA5 data [17] on charged kaon production at low p_T are compatible with this form. Statistical thermodynamic models of hadron production [20] [21] also suggest that spectra should follow this form, which is similar to a thermal Boltzmann distribution. It is reasonable to guess that the transition between e^{-bm_T} behavior and the power-law occurs at a p_T comparable to the mass of the particle involved.

12.1 Extrapolating the K_s^0 Spectrum

For the 1800 GeV data fitted with the Gaussian fitting algorithm, Table 12.1 shows values of $< p_T >$ and $\rho_K(0)$ calculated using various extrapolations. Table 12.2 shows values of λ calculated in two different models (see Appendix E) using these extrapolations. The tables include values of $< p_T >$, $\rho(0)$, and λ obtained when we assume an exponential in p_T below 0.4 GeV and when we assume that the power-law itself holds all the way to $p_T = 0$. λ_1 denotes the strangeness-suppression factor calculated in the model of Anisovich and Kobrinsky [27], while λ_2 indicates the result of the model of Shekhter and Shchlegova [28]. We have deliberately not rounded any of the numbers to the proper number of significant figures, so that trends are more obvious. Moving the transition point over the fairly generous range 0.1 GeV to 0.7 GeV changes $< p_T >$ by roughly 3σ and $\rho(0)$ by roughly 2σ, where σ is the statistical error. If instead we look at a range centered at the K_s^0 mass and extending 200 MeV to either side, we find that $< p_T >$ changes by about 1.5σ and $\rho(0)$ changes by roughly 1σ. These variations can be taken as an estimate of

the systematic errors due to the extrapolation.

One way to convince ourselves that a transverse-mass extrapolation with a transition point near the K_s^0 mass is valid is to look at the spectrum from some Monte-Carlo program. We have generated some $\sqrt{s}$ = 1800 GeV minimum-bias events using Pythia, with parameters set up as recommended in [35] and described in Section 11.2. We selected events according to the same criteria used in the real-data analysis, and generated a spectrum for K_s^0 with $|y| < 1$ for all p_T. We then derive $< p_T >$ and $\rho(0)$ directly from the complete Pythia kaon data, and compare the result with what we get when we cut the spectrum at 0.7 GeV, fit it with the power-law form, and use the m_T extrapolation with various values for the transition. Table 12.3 shows the results. It appears that our analysis, when applied to Pythia events, gives values for $< p_T >$ and $\rho(0)$ that are consistent with their "true" values, within errors.

UA5 uses the m_T extrapolation, with the transition point at 0.4 GeV. If we choose that extrapolation, too, comparisons with UA5 results will be more direct.

12.2 Extrapolating the 630 GeV K_s^0 Spectrum

The statistical uncertainties on our K_s^0 spectrum at $\sqrt{s}$ = 630 GeV are large enough that statistical uncertainties on extrapolated quantities are much larger than systematic errors. Therefore, we use the m_T exponential form below p_T = 0.4 GeV for the results shown in Table 12.4.

12.3 Extrapolating the K_s^0 Spectra for Different Multiplicity Ranges

Using the fit results of Table 9.4 for the K_s^0 spectra in the three multiplicity

Table 12.1

Effects of Choice of Extrapolation on $< p_T >_{K^0_s}$, $\rho_K(0)$, and K/π.

Extrapolation	$< p_T >_{K^0_s}$ (GeV)	$\rho_K(0)$	K/π
e^{-bm_T} below 0.1 GeV	0.557 ± 0.028	0.290 ± 0.039	0.123 ± 0.019
e^{-bm_T} below 0.2 GeV	0.566 ± 0.028	0.285 ± 0.038	0.131 ± 0.018
e^{-bm_T} below 0.3 GeV	0.583 ± 0.028	0.275 ± 0.036	0.125 ± 0.018
e^{-bm_T} below 0.4 GeV	0.603 ± 0.027	0.262 ± 0.033	0.119 ± 0.016
e^{-bm_T} below 0.5 GeV	0.625 ± 0.027	0.248 ± 0.030	0.112 ± 0.015
e^{-bm_T} below 0.6 GeV	0.648 ± 0.027	0.233 ± 0.028	0.105 ± 0.014
e^{-bm_T} below 0.7 GeV	0.672 ± 0.025	0.219 ± 0.025	0.0979 ± 0.0123
power law for all Pt	0.555 ± 0.029	0.292 ± 0.039	0.135 ± 0.019
e^{-bp_T} below 0.4 GeV	0.568 ± 0.028	0.283 ± 0.037	0.130 ± 0.018

Table 12.2

Effects of Choice of Extrapolation on λ_1 and λ_2.

Extrapolation	λ_1	λ_2
e^{-bm_T} below 0.1 GeV	0.43 ± 0.07	0.40 ± 0.05
e^{-bm_T} below 0.2 GeV	0.42 ± 0.07	0.39 ± 0.05
e^{-bm_T} below 0.3 GeV	0.39 ± 0.06	0.38 ± 0.05
e^{-bm_T} below 0.4 GeV	0.38 ± 0.06	0.35 ± 0.05
e^{-bm_T} below 0.5 GeV	0.35 ± 0.05	0.33 ± 0.04
e^{-bm_T} below 0.6 GeV	0.33 ± 0.05	0.31 ± 0.04
e^{-bm_T} below 0.7 GeV	0.31 ± 0.04	0.28 ± 0.03
power law for all Pt	0.43 ± 0.07	0.41 ± 0.05
e^{-bp_T} below 0.4 GeV	0.41 ± 0.06	0.39 ± 0.05

Table 12.3

m_T Extrapolation vs Direct "measurement" for Pythia K^0_s at 1800 GeV

Direct "measurement"	$< p_T >_{K^0_s}$ (GeV	$\rho_K(0)$
	0.606 ± 0.009	0.233 ± 0.003
Extrapolation		
e^{-bm_T} below 0.1 GeV	0.579 ± 0.027	0.309 ± 0.015
e^{-bm_T} below 0.2 GeV	0.589 ± 0.025	0.304 ± 0.014
e^{-bm_T} below 0.3 GeV	0.605 ± 0.025	0.294 ± 0.013
e^{-bm_T} below 0.4 GeV	0.625 ± 0.025	0.281 ± 0.012
e^{-bm_T} below 0.5 GeV	0.647 ± 0.025	0.266 ± 0.011
e^{-bm_T} below 0.6 GeV	0.671 ± 0.025	0.252 ± 0.009
e^{-bm_T} below 0.7 GeV	0.694 ± 0.025	0.237 ± 0.008
power law for all Pt	0.578 ± 0.026	0.311 ± 0.015
e^{-bp_T} below 0.4 GeV	0.591 ± 0.025	0.302 ± 0.014

Table 12.4

Results of extrapolating the K^0_s spectrum at 630 GeV using an exponential in transverse mass below $p_T = 0.4$ GeV and the power-law above.

$< p_T >_{K^0_s}$ (GeV)	$\rho_K(0)$	K/π	λ
0.5 ± 0.1	0.2 ± 0.1	0.06 ± 0.03	0.17 ± 0.09

ranges, we have applied the m_T extrapolation with the transition at 0.4 GeV to compute $< p_T >$, $\rho(0)$, the K/π ratio and the strangeness-suppression factor. Tables 12.5 and 12.6 show the results.

Table 12.5

Extrapolated quantities for 1800 GeV K^0_s data from various VTPC multiplicity ranges

VTPC multiplicity range	$< p_T >_{K^0_s}$ (GeV)	$\rho_K(0)$	K/π
4-14	0.49 ± 0.06	0.14 ± 0.04	0.18 ± 0.05
15-27	0.57 ± 0.04	0.20 ± 0.05	0.12 ± 0.03
≥ 28	0.63 ± 0.04	0.46 ± 0.08	0.12 ± 0.02

Table 12.6

λ for 1800 GeV K^0_s data from various VTPC multiplicity ranges.

VTPC multiplicity range	λ_1	λ_2
4-14	0.6 ± 0.2	0.6 ± 0.2
15-27	0.4 ± 0.1	0.39 ± 0.08
≥ 28	0.36 ± 0.07	0.35 ± 0.06

12.4 Extrapolating the Λ plus $\bar{\Lambda}$ Spectrum

Tables 12.7 and 12.8 show the results of a number of possible extrapolations of the Λ plus $\bar{\Lambda}$ spectrum. The ratio Λ/K is defined as $\rho_{\Lambda\bar{\Lambda}}(0)/(2\rho_K(0))$, where we use the value of $\rho_K(0)$ obtained using the power-law above, and the m_T exponential extrapolation below, $p_T = 0.4$ GeV. The quantitity $\rho_{h^+} + \rho_{h^-}$ in the denominator of the lambda-to-charged-hadron ratio $\rho_{\Lambda\bar{\Lambda}}/\rho_{h^+} + \rho_{h^-}$ is the sum of the central rapidity densities for positive and for negative charged hadrons, as determined from the CDF single-charged-particle data [14], and is equal to 4.86 ± 0.08. λ_3 is the strangeness-suppression factor calculated from the ratio $\rho_{\Lambda\bar{\Lambda}}/\rho_{h^+} + \rho_{h^-}$ in the model of Anisovich and Kobrinsky [27]. In the table, the power-law fit to the $\Lambda/\bar{\Lambda}$ is used above the p_T transition, except where noted.

12.5 Comparison with Lower-Energy Data

Clearly, the values of $< p_T >$, $\rho(0)$, and λ are depend on the ways that the spectra are extrapolated. In what follows, the K^0_s results we will present will assume that the cross-section follows the fitted power-law above $p_T = 0.4$ GeV, and follows the form e^{-bm_T} below this point; the transition point is chosen at 0.4 GeV because putting it there gave a good fit to UA5 kaon data [17]. The Λ results we will present will make the same assumptions, except that we will assume that the transition between power-law and e^{-bm_T} behavior occurs at $p_T = 1.1$ GeV; we have placed the transition point arbitrarily, guessing that the transition point should be near the Λ mass, since UA5 found that putting the transition point in the neighborhood of the K^0_s mass gave acceptable fits.

We find that for the 1800 GeV data, with the extrapolation described above,

Table 12.7

Effects of choice of extrapolation on $< p_T >_{\Lambda\bar{\Lambda}}$, and $\rho_{\Lambda\bar{\Lambda}}(0)$.

Extrapolation	$< p_T >_{\Lambda\bar{\Lambda}}$ (GeV)	$\rho_{\Lambda\bar{\Lambda}}(0)$
e^{-bm_T} below 0.8	0.72 ± 0.07	0.13 ± 0.05
e^{-bm_T} below 0.9	0.74 ± 0.07	0.12 ± 0.05
e^{-bm_T} below 1.0	0.77 ± 0.07	0.11 ± 0.05
e^{-bm_T} below 1.1	0.79 ± 0.08	0.11 ± 0.04
e^{-bm_T} below 1.2	0.82 ± 0.09	0.09 ± 0.04
e^{-bm_T} below 1.3	0.84 ± 0.08	0.09 ± 0.03
e^{-bm_T} below 1.4	0.86 ± 0.08	0.09 ± 0.03
power-law for all p_T	0.58 ± 0.07	0.18 ± 0.08
e^{-bp_T} for all p_T	1.0 ± 0.1	0.06 ± 0.02

Table 12.8

Effects of choice of extrapolation on the ratios $(\Lambda+\bar{\Lambda})/(2K^0_s)$ and $(\Lambda+\bar{\Lambda})/(h^++h^-)$.

Extrapolation	Λ/K	$(\Lambda+\bar{\Lambda})/(h^++h^-)$	λ_3
e^{-bm_T} below 0.8	0.25 ± 0.10	0.027 ± 0.010	0.19 ± 0.07
e^{-bm_T} below 0.9	0.23 ± 0.09	0.025 ± 0.010	0.17 ± 0.06
e^{-bm_T} below 1.0	0.21 ± 0.09	0.023 ± 0.010	0.16 ± 0.06
e^{-bm_T} below 1.1	0.21 ± 0.08	0.023 ± 0.008	0.16 ± 0.05
e^{-bm_T} below 1.2	0.17 ± 0.08	0.019 ± 0.008	0.13 ± 0.05
e^{-bm_T} below 1.3	0.17 ± 0.06	0.019 ± 0.006	0.13 ± 0.04
e^{-bm_T} below 1.4	0.17 ± 0.06	0.019 ± 0.006	0.13 ± 0.04
power-law for all p_T	0.35 ± 0.16	0.037 ± 0.016	0.04 ± 0.02
e^{-bp_T} for all p_T	0.12 ± 0.04	0.012 ± 0.004	0.08 ± 0.02

31% of the cross-section for K_s^0 lies above 0.7 GeV, which is where our K_s^0 candidates are. In other words, about 1/3 of our $\rho(0)$ value comes from the part of the cross-section that we can actually measure. Similarly, with the extrapolation described for the Λ spectrum, the portion of the total Λ cross section in $|y| < 1$ that lies above $p_T = 1.3$ GeV, which is where our Λ candidates lie, is 21%.

12.5.1 Mean Transverse Momenta for K_s^0 and Λ

Figure 12.1 shows the behavior of $< p_T >$ for K_s^0 as a function of $\sqrt{s}$. The UA5 points shown are from Refs. [17] and [22]. Our 1800 GeV point is similar to the UA5 result at 900 GeV, and combined with the UA5 and CERN Intersecting Storage Rings (ISR) results, it strongly suggests that $< p_T >$ for K_s^0 increases more rapidly than linearly in $\ln s$.

Figure 12.2 shows the behavior of $< p_T >$ for Λ and $\bar{\Lambda}$ versus $\sqrt{s}$. The lower-energy data shown are from Refs. [42], [43], [44], and [45], and the other point at 1800 GeV is from Ref. [46]. Our result is very close to the result from the C0 experiment [46] at the Tevatron Collider.

12.5.2 Particle Production Ratios

We calculate the particle production ratios based on the central rapidity densities of the particles in question. The central rapidity density $\rho_K(0)$ for K_s^0 is shown as a function of $\sqrt{s}$ in Fig. 12.3, where the UA5 data are from Refs. [17] and [22]. The data shown are consistent with a rise in $\rho_K(0)$ that is linear in $\ln s$.

The K/π ratio is shown versus $\sqrt{s}$ in Fig. 12.4. The lower-energy data shown are from Refs. [47], [17], and [22]. It should be noted that the lower-energy

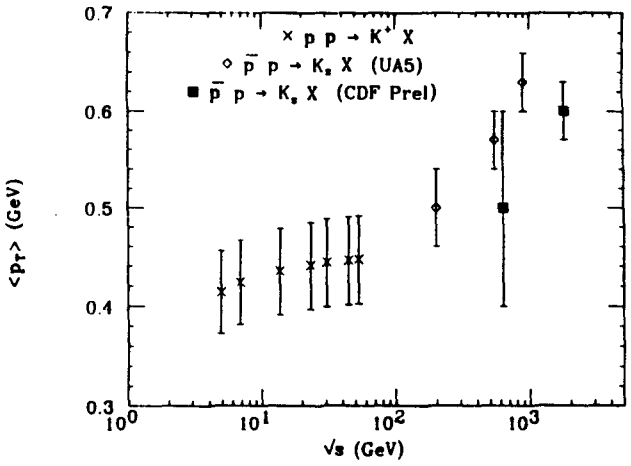

Figure 12.1

$< p_T >$ for K_s^0 versus c.m. energy.

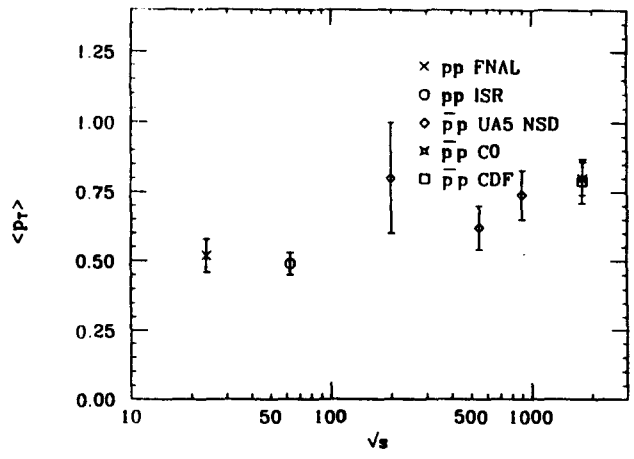

Figure 12.2

$< p_T >$ for Λ and $\bar{\Lambda}$ versus c.m. energy.

results are based on particle yields in all phase space, while ours are based only on production in the central region, as outlined in Appendix E. The data shown suggest a slow linear rise of K/π with $\sqrt{s}$, but they are also consistent with no rise at all.

Figure 12.5 shows the Λ-to-charged-hadron ratio as a function of $\sqrt{s}$. The lower-energy data are from Refs. [48], [44], and [45], while the other 1800 GeV point is from Ref. [46]. Here again, the data shown suggest a slow rise but are also consistent with no rise at all. The ratio $(\Lambda + \bar{\Lambda})/(2K^0_s)$ is shown versus $\sqrt{s}$ in Figure 12.6, along with data from Refs. [42], [43], [44], and [45]. In both figures, the reader must bear in mind that the systematic error on our value of $\rho_\Lambda(0)$ is very large, implying large systematic errors on both particle ratios.

12.5.3 The Strangeness-Suppression Factor

Our value for λ, the strangeness-suppression factor calculated from our K/π ratios using the model of Ref. [27] (see also Appendix E) is shown in Figure 12.7. The lower-energy data also shown are from Refs. [17], [22], and Ref. [49] and references therein. Above $\sqrt{s} \sim 10$ GeV or so, the data are consistent with λ being constant. Malhotra and Orava [49] have done an extensive study of the strangeness-suppression factor in many types of high-energy interactions, over a large range of effective subprocess energies $\sqrt{s_{\rm eff}}$. In Figure 12.8 we have plotted their data for hadron collisions, along with our own data and UA5 results from Refs. [17] and [22]. For our data and UA5's, we have calculated $\sqrt{s_{\rm eff}}$ using the relation used by Malhotra and Orava for $p\bar{p}$ collisions, $\sqrt{s_{\rm eff}} = 0.11\sqrt{s}$. Again, after a rapid turn-on below $\sqrt{s_{\rm eff}} \sim 1$ GeV, the data are consistant with λ having a constant value,

independent of $\sqrt{s}$. Malhotra and Orava, using a somewhat different data set than that shown, obtain a "world value" of $\lambda = 0.29 \pm 0.02$. When we calculate λ from the K/π ratio that we get with the e^{-bm_T} extrapolation with the transition point at $p_T = 0.4$ GeV, we find $\lambda = 0.38 \pm 0.06$, which is 1.5σ higher than the world value. On the other hand, while when we calculate λ using the value of the ratio $(\Lambda + \bar{\Lambda})/(h^+ + h^-)$ that we get with the e^{-bm_T} extrapolation with the transition at $p_T = 1.1$ GeV, we find $\lambda = 0.16 \pm 0.05$, which is lower than the world value by roughly 3σ.

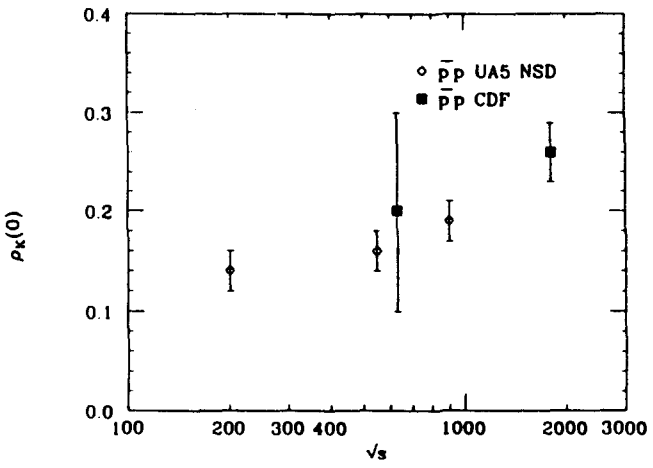

Figure 12.3

The central rapidity density $\rho_K(0)$ versus c.m. energy.

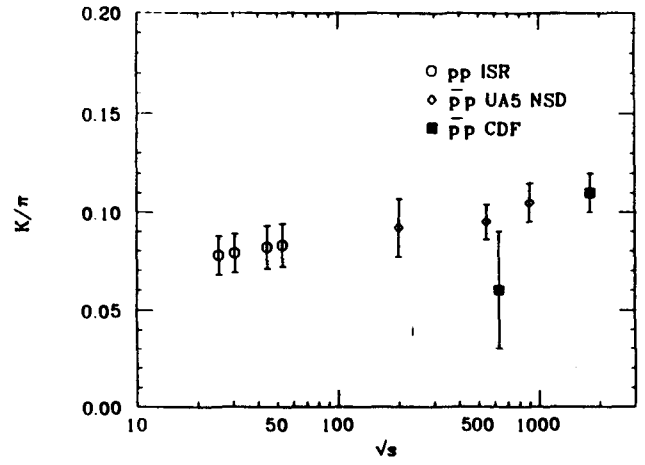

Figure 12.4

The K/π ratio versus c.m. energy.

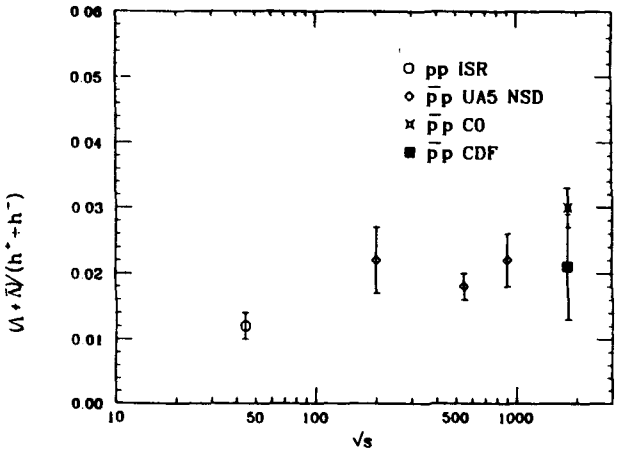

Figure 12.5

The Λ to charged hadron ratio versus c.m. energy.

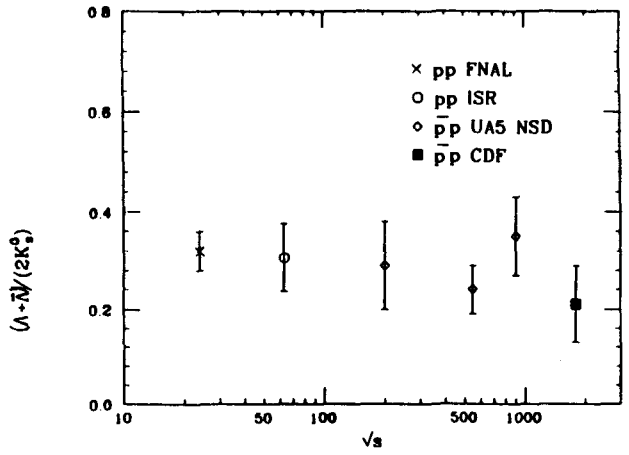

Figure 12.6

The Λ/K ratio versus c.m. energy.

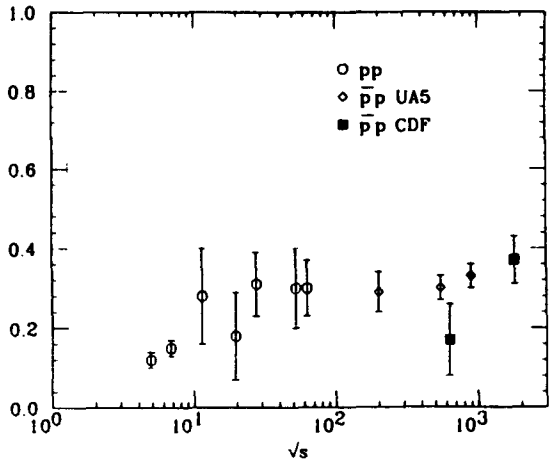

Figure 12.7

The strangeness-suppression factor λ versus c.m. energy.

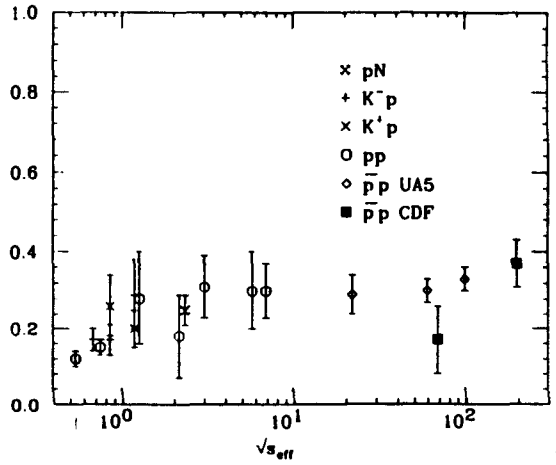

Figure 12.8

The strangeness-suppression factor λ versus effective c.m. energy of subprocesses.

13. SUMMARY OF CONCLUSIONS

We summarize here some highlights of the results presented in the preceding chapters.

- We have measured the inclusive p_T spectra for K_s^0 in $p\bar{p}$ collisions at $\sqrt{s}$ = 630 and 1800 GeV, and of $\Lambda/\bar{\Lambda}$ at $\sqrt{s}$ = 1800 GeV.
- At $\sqrt{s}$ = 1800 GeV, the ratio, as a function of p_T, of the invariant cross section for K_s^0 production to the invariant cross section for charged hadron production is very similar to results obtained at much lower $\sqrt{s}$, suggesting that the shape of this ratio curve may be independent of $\sqrt{s}$.
- We have estimated $< p_T >_{K_s^0}$= 0.5±0.1 GeV at $\sqrt{s}$ = 630 GeV and 0.60±0.03 GeV at $\sqrt{s}$ = 1800 GeV, values which are consistent with the ones obtained by the UA5 collaboration [17] [22] at $\sqrt{s}$ = 546 and 900 GeV, respectively. Our estimate of $< p_T >_{\Lambda\bar{\Lambda}}$= 0.79 ± 0.08 at $\sqrt{s}$ = 1800 GeV is very close to the result obtained by the C0 collaboration [46] at the same c.m. energy.
- We have determined $\rho_K(0)$ = 0.2 ± 0.1 at $\sqrt{s}$ = 630 GeV and $\rho_K(0)$ = 0.26 ± 0.03 at $\sqrt{s}$ = 1800 GeV, values which are also similar to UA5 results [17] [22] at $\sqrt{s}$ = 546 and 900 GeV, respectively. We have calculated the K/π ratio to be 0.06 ± 0.03 at $\sqrt{s}$ = 630 GeV and 0.11 ± 0.01 at $\sqrt{s}$ = 1800 GeV.
- Using our K_s^0 data, we have estimated the strangeness-suppression factor

$\lambda = 0.17 \pm 0.09$ at $\sqrt{s} = 630$ GeV and $\lambda = 0.38 \pm 0.06$ at $\sqrt{s} = 1800$ GeV, values which are consistent with the "world value" of Malhotra and Orava [49] of 0.29 ± 0.02. The value $\lambda = 0.16 \pm 0.05$ that we calculate from our $(\Lambda + \bar{\Lambda}/(h^+ + h^-)$ ratio at $\sqrt{s} = 1800$ GeV, is, however, about three standard deviations smaller than the world value.

BIBLIOGRAPHY

BIBLIOGRAPHY

1. Design Report: Tevatron I Project, Fermi National Accelerator Laboratory, Sept. 1984.

2. F. Abe et al., Nucl. Inst. and Meth. A271, 487 (1988).

3. F. Snider et al., Nucl. Inst. and Meth. A268, 75 (1988).

4. F. Bedeschi et al., Nucl. Instr. and Meth. A268, 50 (1988).

5. M. Sekiguchi, *Multiplicity and Transverse Momentum Distributions of Charged Particles in Proton-Antiproton Collisions at* $\sqrt{s}$ *= 630 and 1800 GeV*, PhD Thesis, University of Tsukuba, June 1988.

6. G.P. Yeh, *Event Selection and ZVTFLT*, CDF Note CDF/MIN_BIAS/ANAL-/CDFR/596 (unpublished), January 1988.

7. K. Goulianos and S. Belforte, *A "Complete" Minimum-Bias Event Generator*, CDF Note CDF/DOC/PUBLIC/256 (unpublished), 1985.

8. Franco Bedeschi, *A Vertex Fitting Method Without Steering of Track Parameters*, CDF/MEMO/SEC_VTX/GROUP/818 (unpublished), May 1986.

9. M. Schub and F. Bedeschi, *Revised Specification of Vertex-Fitting Routines*, CDF/MEMO/SEC_VTX/GROUP/823 (unpublished), September 1986.

10. Aesook Byon, *Track Expansion Routines*, CDF Note CDF/MEMO/-SEC_VTX/GROUP/822 (unpublished), August 1986.

11. P. Billoir, R. Fruhwirth, and M. Regler, *Track element merging strategy and vertex fitting in complex modular detectors*, Nucl. Inst. and Meth. A241:115–131, 1985.

12. Particle Data Group (G.P. Yost, et al.), *Review of Particle Properties*, Phys. Lett. B204, 1 (1988).

13. J. Freeman, *CDF Detector Simulation*, Fermilab Publication Fermilab-Conf-87/230, December 1987.

14. F. Abe et al., Phys. Rev. Lett. 61, 1819 (1988).

15. John Skarha, *Secondary Interaction Background to the Single Particle Inclusive p_T Spectrum*,CDF Note CDF/MEMO/MIN_BIAS/CDFR/575 (unpublished), December, 1987.

16. D. Antreasyan et al., Phys. Rev. D19, 764 (1979).

17. G.J. Alner et al., Nucl. Phys. B258, 505 (1985).

18. B. Alper et al., Nucl. Phys. B100, 237 (1975).

19. M. Banner et al. (UA2 Collaboration), Phys. Lett. 122B, 322 (1983).

20. R. Hagedorn, in *Cargèse Lectures in Physics*, edited by E. Schatzmann (Gordon and Breach, New York, 1973), Vol. 6, p. 643.

21. R. Hagedorn, Riv. Nuovo Cim. 6, No. 10 (1983).

22. R.E. Ansorge, et al., Phys. Lett. B 199 (1987), 311.

23. G. Arnison et al., Phys. Lett 118B, 167 (1982).

24. S. Berman, J. Bjorken, and J. Kogut, Phys. Rev. D 4, 3388.

25. D. Jones and J.F. Gunion, Phys. Rev. D19 (1979), 867.

26. B. Andersson, G. Gustafson, G. Ingelman and T. Sjöstrand, Phys. Rep. 97, 33 (1983).

27. V.V Anisovich and M.N. Kobrinsky, Phys. Lett. 52B, 217 (1974).

28. V.M. Shekhter and L.M. Shchlegova, Sov. J. Nucl. Phys. 27, 567 (1978).

29. S.D. Ellis, private communication (to A. Para).

30. A.D. Martin, R.G. Roberts, W.J. Stirling, Phys. Lett. 206B, 327 (1988).

31. J. Owens, Phys. Rev. D19, 3279 (1979).

32. E. Eichten, I. Hinchliffe, K. Lane, and C. Quigg, Rev. Mod. Phys. 56, 579 (1984).

33. H-U. Bengtsson and T. Sjöstrand, Comp. Phys. Comm. 46, 43 (1987).

34. T. Sjöstrand, Comp. Phys. Comm. 39, 347 (1986).

35. T. Sjöstrand and M. van Zijl, Phys. Rev. D36, 2019 (1987).

36. R.K. Ellis and J.C. Sexton, Nucl. Phys. B269, 445 (1986).

37. B. Nilsson-Almqvist, *High Energy Hadronic Interations*, PhD. Thesis, University of Lund, 1987.

38. B. Nilsson-Almqvist. *The Lund Monte Carlo Programme for High Energy Interactions Between Hadrons and Nuclei*, University of Lund Preprint LU-TP 85-7 LUIP 8507, July 1985.

39. B. Nilsson-Almqvist, *The Lund Model for Low-p_T Hadronic Reactions*, University of Lund Preprint LU-TP 86-13, August 1986.

40. B. Nilsson-Almqvist, *The Lund Low-p_T Fritiof Extended to High-p_T Events*, University of Lund Preprint LU-TP 86-13, August 1986.

41. K. Guettler et al., Nucl. PHys. B116, 77 (1976).

42. A. Sheng, et al., Phys. Rev. D11, 1733 (1975).

43. D. Drijard, et al., Z. Phys. C12, 317 (1982).

44. G.J. Alner, et al., Phys. Lett. 167B, 476 (1986).

45. R.E. Ansorge, et al., *Hyperon Production at 200 and 900 GeV c.m. Energy*, CERN report CERN-EP/89-41, (submitted to Z. Phys. C.), March 1989.

46. S. Banerjee, et al., Phys. Rev. Lett. 63, 12 (1988).

47. A.M. Rossi, et al., Nucl. Phys. B84, 269 (1984).

48. F.W. Büsser, et al., Phys. Lett. 61B, 309 (1976).

49. P.K. Malhotra and R. Orava, Z. Phys. C17, 84 (1983).

50. F. James and M. Roos, *MINUIT Manual–CERN Computer Centre Program Library*, CERN Scientific Information Service, Geneva, Switzerland, 1983.

APPENDICES

Appendix A: Vertex Algorithm Pseudo-Code

```
        NTRY = 1            ! count the number of iterations
        CHIOLD = 999999.    ! initialize for later convergence check
        RV = 0.             ! starting vertex radius is 0

TOP:    Do Non-Steering Fit, get CHI2 and NEWRV
        IF (CHI2.GT.1000) THEN    ! fit obviously not converging
          GOTO OUT_OF_LOOP
        ENDIF
        NTRY = NTRY + 1
        IF (NTRY.GT.10) THEN      ! limit number of iterations
          GOTO OUT_OF_LOOP
        ENDIF
        DLTCHI = CHIOLD - CHI2    ! check change in chi**2
                                  ! vs last pass
        IF (DLTCHI.LT.0.1) THEN ! convergence criterion
          GOTO OUT_OF_LOOP
        ELSEIF (DLTCHI.LT.0.) THEN        ! fit may be oscillating
          RV = 0.5*(NEWRV+OLDRV)          ! damp by averaging radii
                                          ! with that of last iter.
C
C         Protect from cases where pair appears to intersect
```

```
C   at a point outside the chamber, which is a symptom
C   of a diverging fit
C
          IF (RV.GT.(CHAMBER RADIUS)) THEN
            GOTO OUT_OF_LOOP
          ENDIF
          CHIOLD = CHI2
          GOTO TOP      ! do another iteration
        ELSE
          OLDRV = NEWRV
          IF (NEWRV.GT.(CHAMBER RADIUS)) THEN
             GOTO OUT_OF_LOOP
          ENDIF
          CHIOLD = CHI2
          GOTO TOP      ! do another iteration
        ENDIF
```

```
OUT_OF_LOOP:IF((CHI2/NDOF).LE.5.).AND.(RV.LT.(CHAMBER RADIUS)))THEN
                Do Steering Fit, get CHI2_STEERING
                IF ((CHI2_STEERING/NDOF).GT.5) THEN
                   NOT an acceptable vertex
                ELSE
                   Acceptable Vertex
                ENDIF
             ELSE
               NOT an acceptable vertex
             ENDIF
```

Appendix B: Comparison Plots—Real Data vs. Simulation

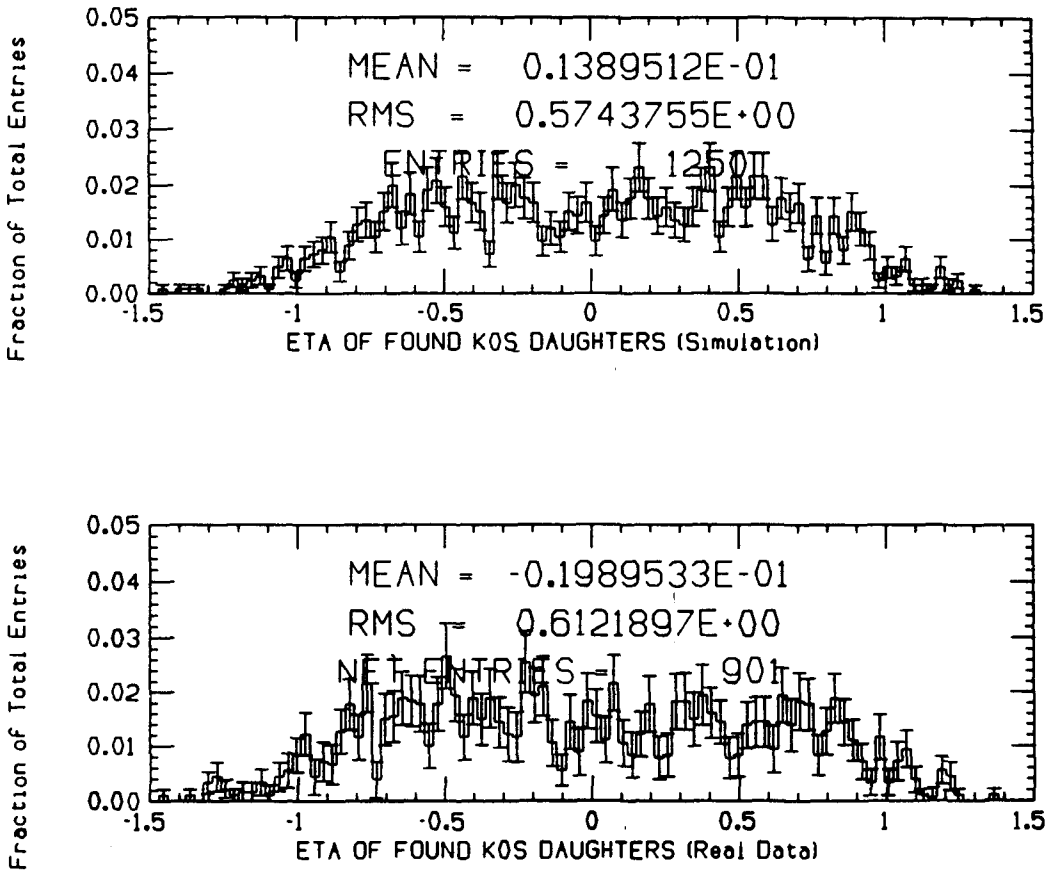

Figure B.1

η of found K_s^0 daughters—simulation (top) versus real data (bottom).

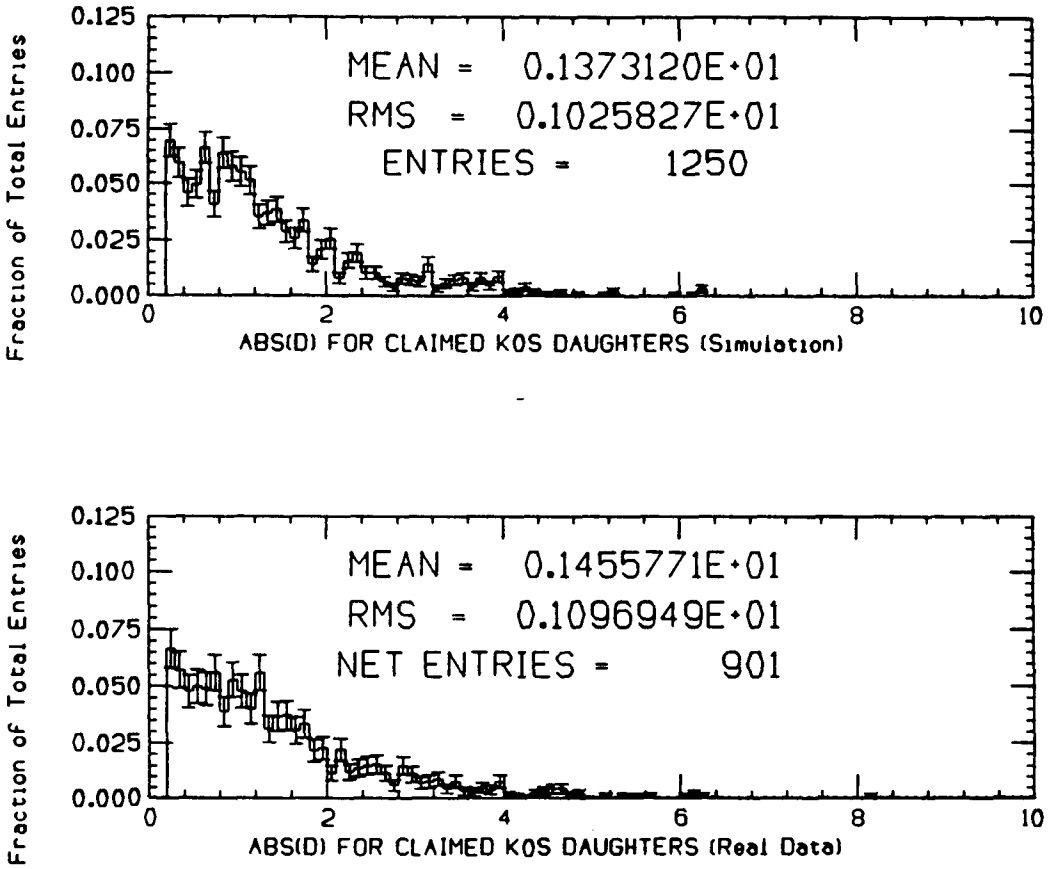

Figure B.2

Absolute value of impact parameter (in cm) for found K_s^0 daughters—simulation (top) versus real data (bottom). The distributions have been cut off at 0.2 cm.

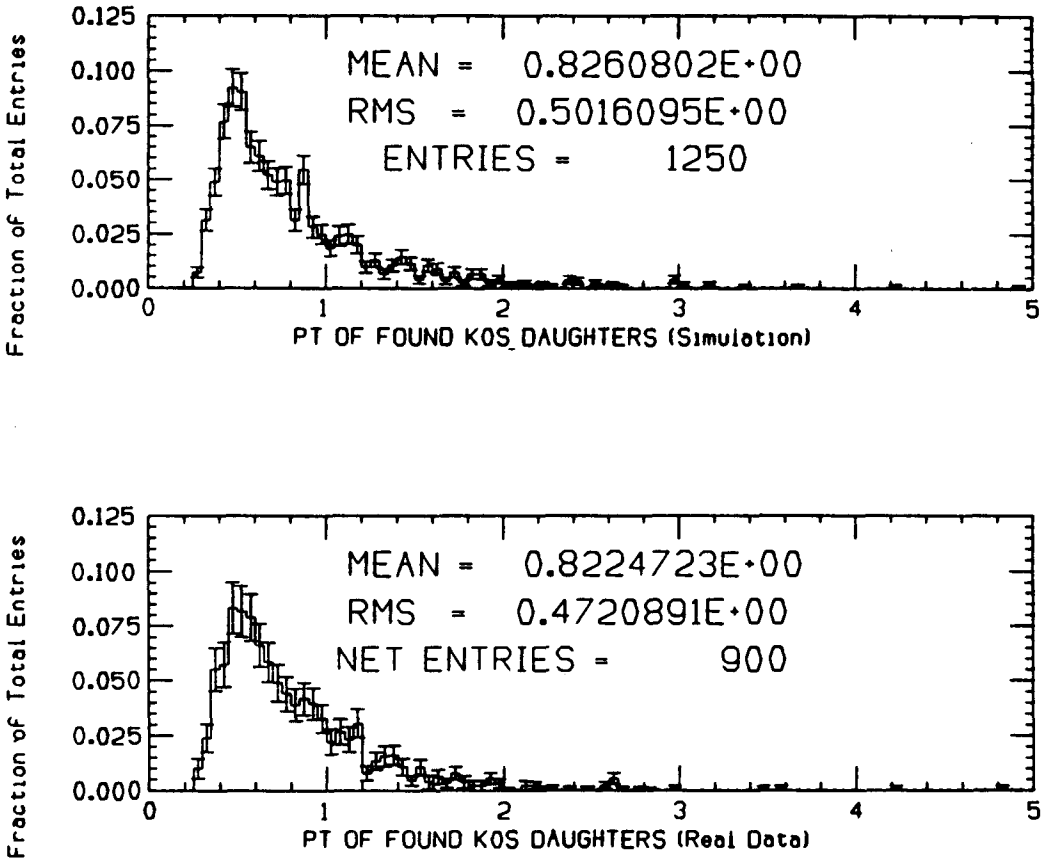

Figure B.3

p_T of found K_s^0 daughters—simulation (top) versus real data (bottom).

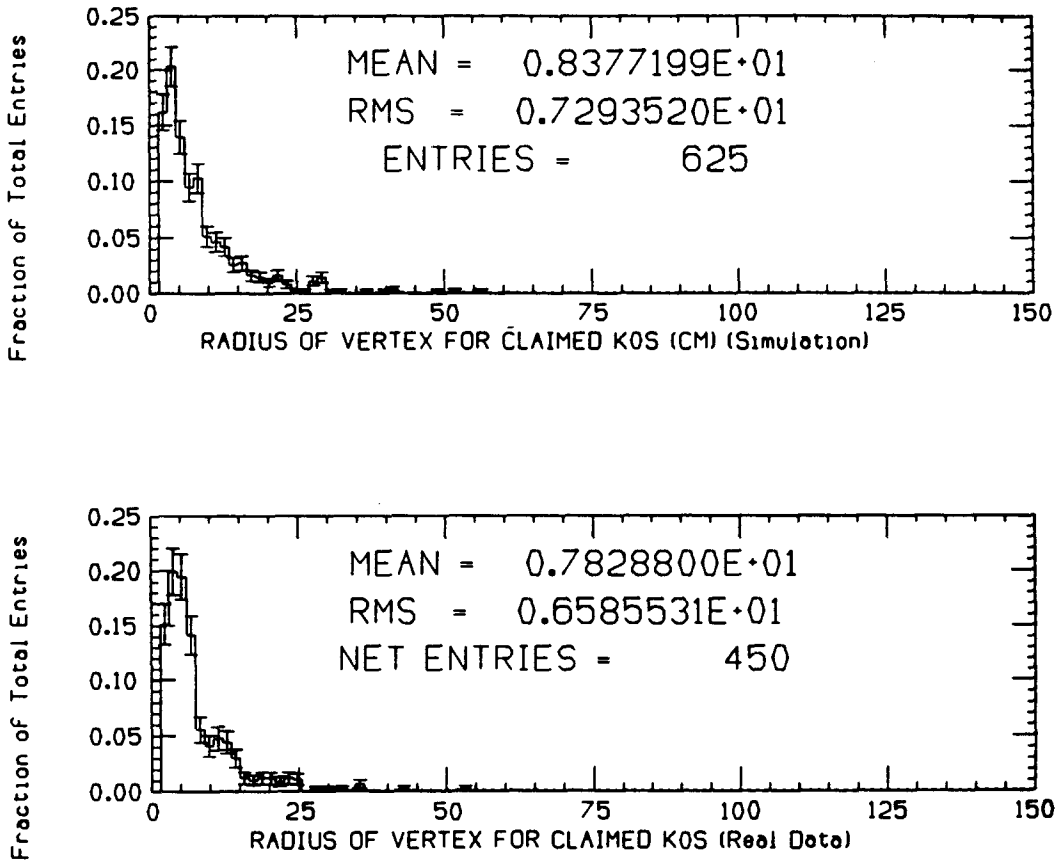

Figure B.4

Radius of vertex (in cm) for K_s^0 candidates—simulation (top) versus real data (bottom). The distributions have been cut off at 2 cm.

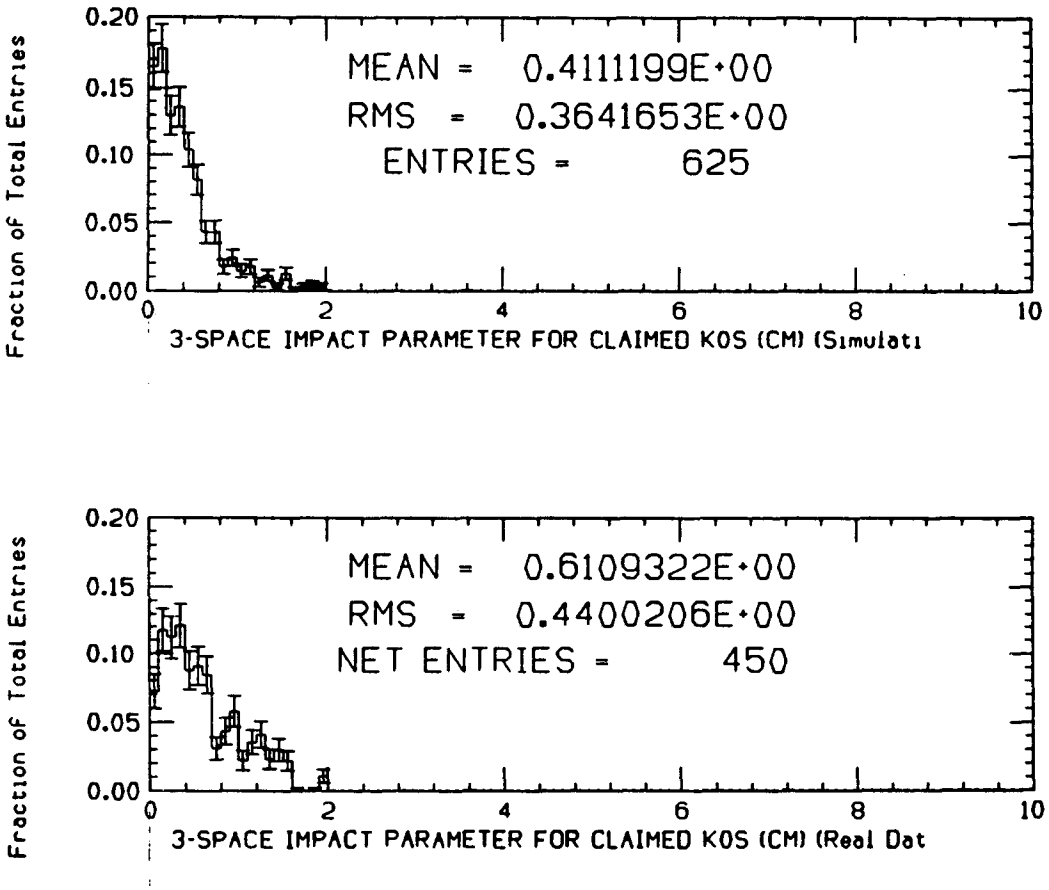

Figure B.5

Pointing impact parameter (in cm) for K_s^0 candidates—simulation (top) versus real data (bottom). The distributions have been cut off at 2 cm.

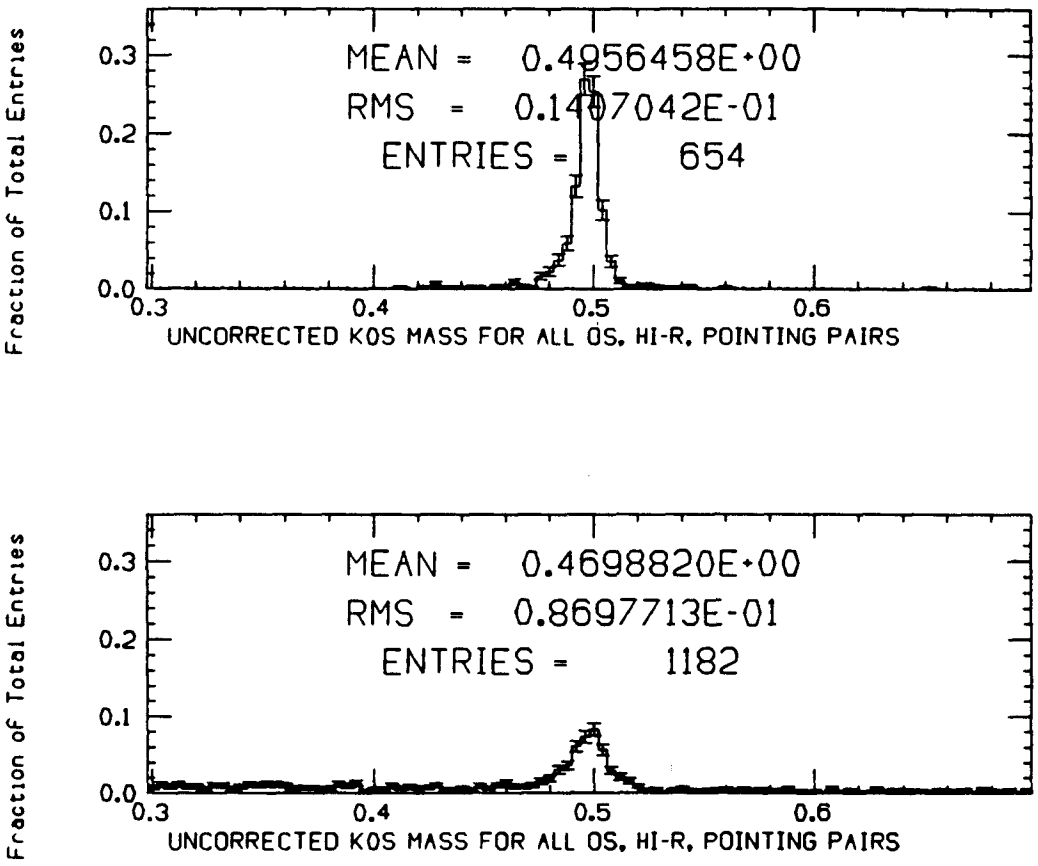

Figure B.6

Uncorrected K_s^0 mass (in GeV) for found simulated K_s^0 (top) versus all real-data track pairs passing cuts (bottom).

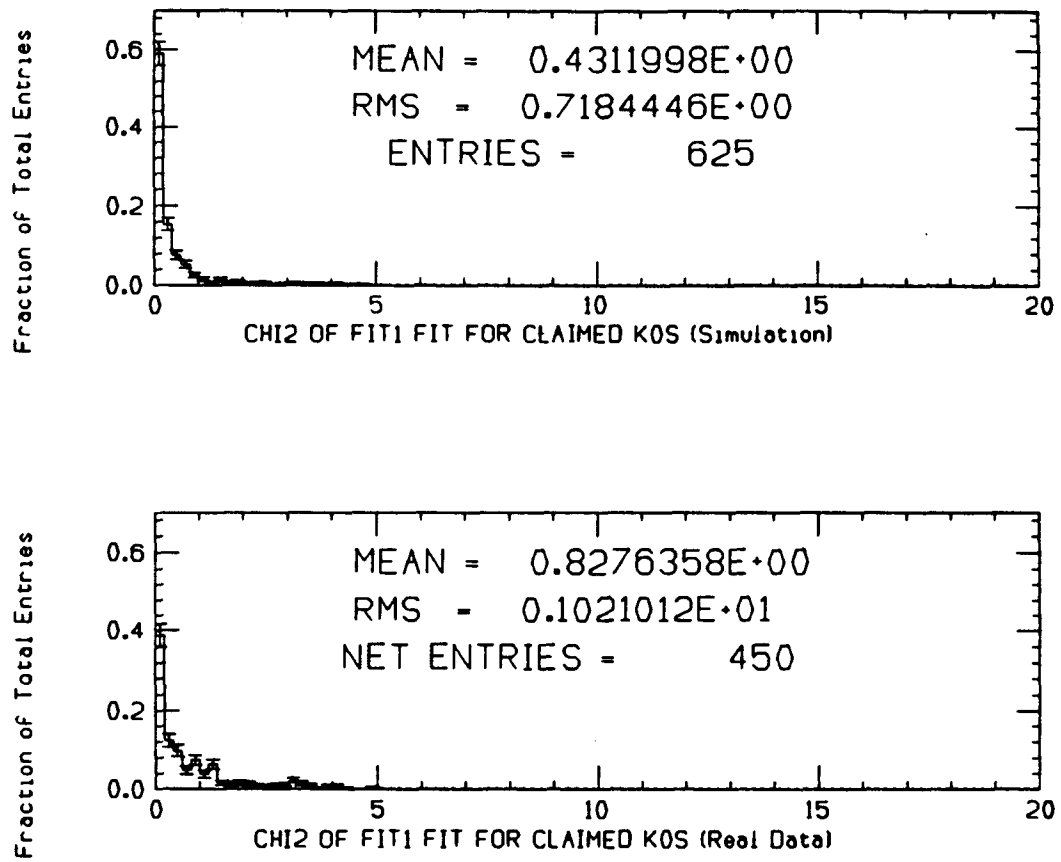

Figure B.7

χ^2 of vertex fit for K_s^0 candidates—simulation (top) versus real data (bottom). The distributions have been cut off at 5.

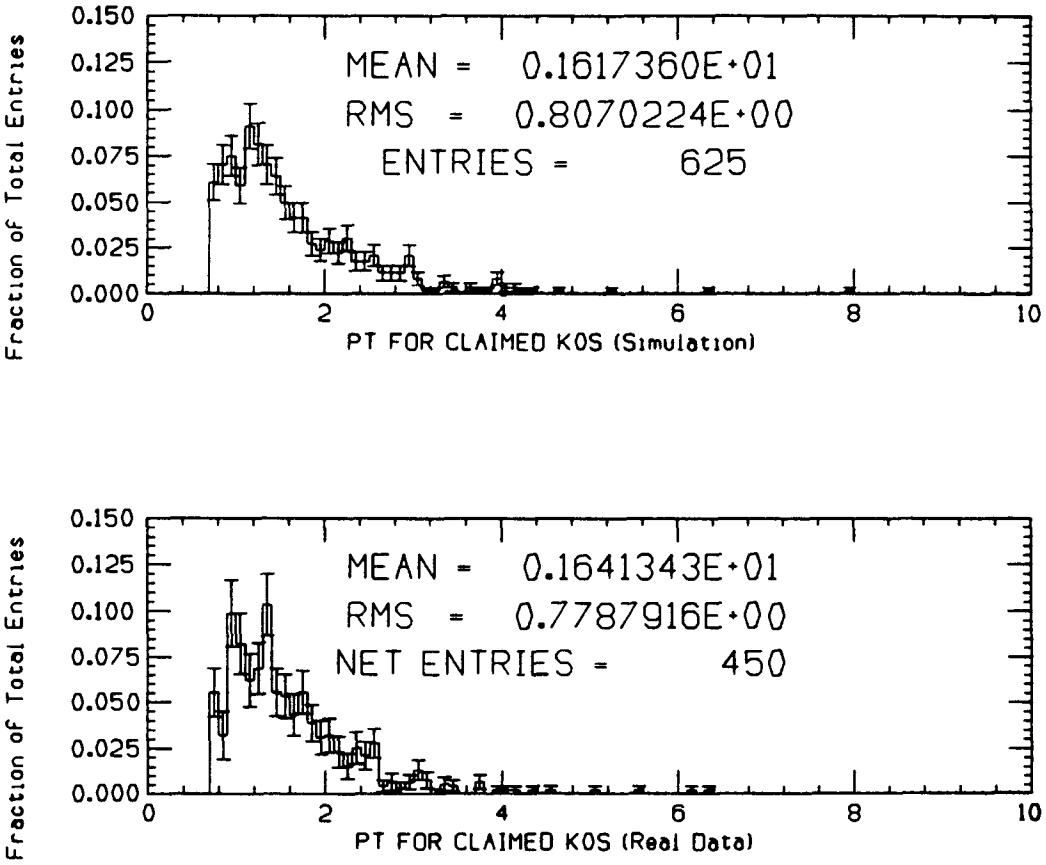

Figure B.8

p_T for K_s^0 candidates—simulation (top) versus real data (bottom).

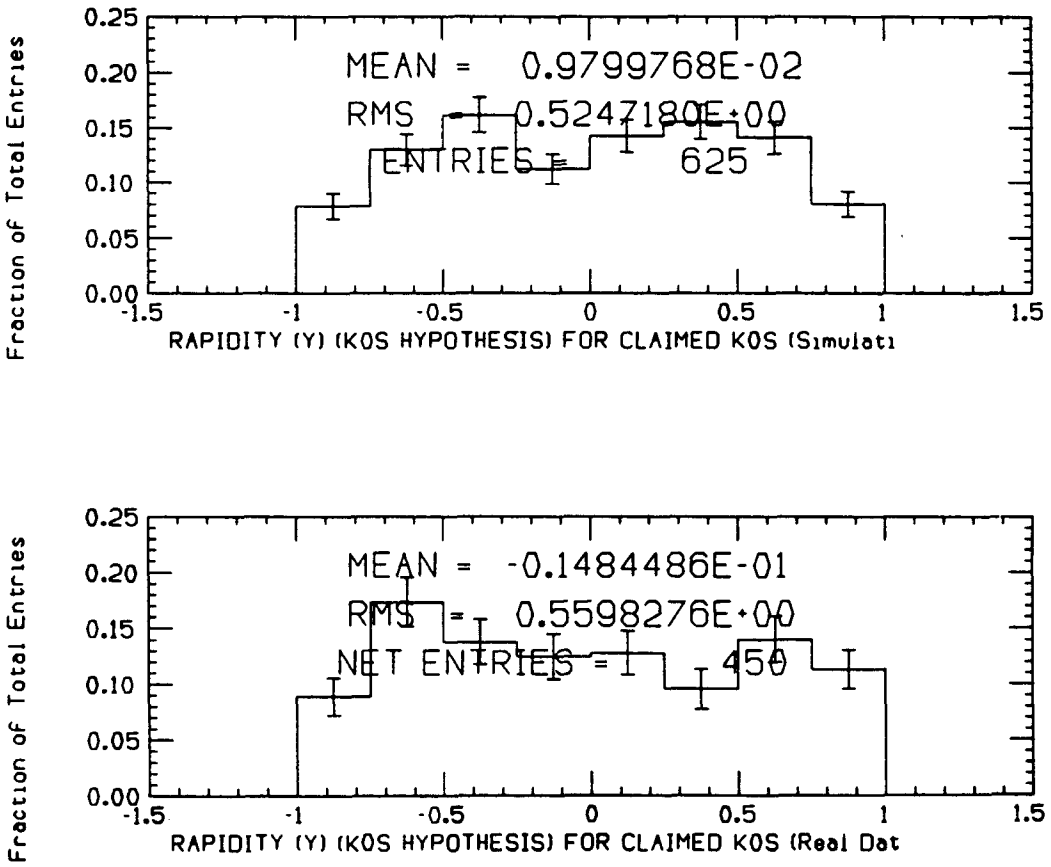

Figure B.9

Rapidity (y) of K^0_s candidates—simulation (top) versus real data (bottom). The distributions have been cut off at ± 1.

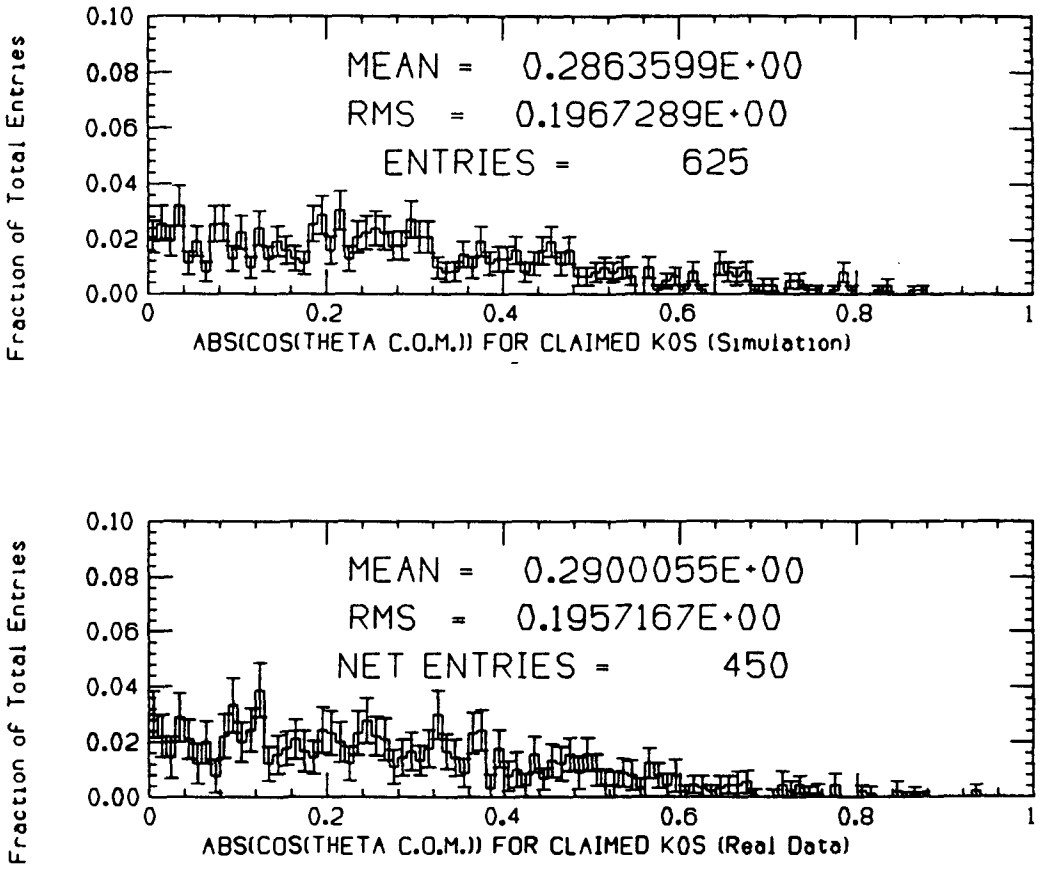

Figure B.10

Center-of-mass decay angle ($\cos(\theta^*)$) for K_s^0 candidates—simulation (top) versus real data (bottom).

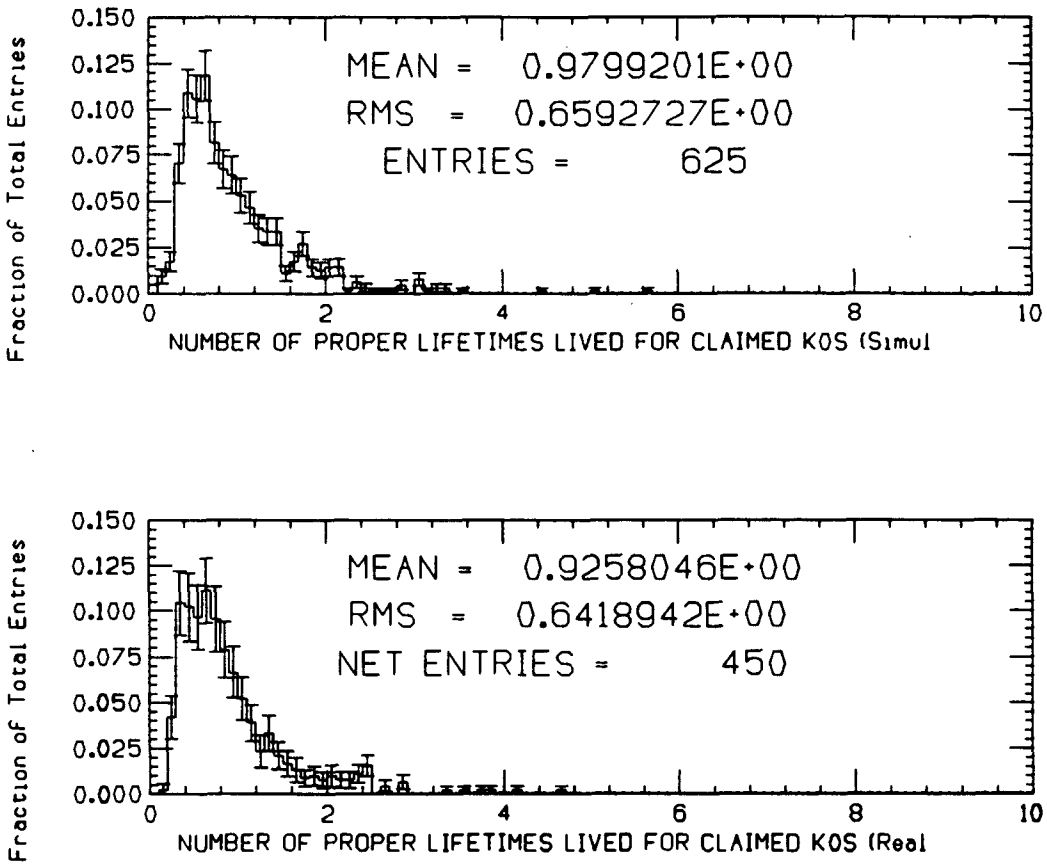

Figure B.11

Number of proper lifetimes lived (t/τ) for K_s^0 candidates—simulation (top) versus real data (bottom).

Appendix C: Error Propogation

This appendix describes and provides formulae for the propogation of errors for various stages of the K_s^0 analysis. The same techniques and formulae were applied in the $\Lambda/\bar{\Lambda}$ analysis.

C.1 Calculating Errors for the p_T Spectrum

As described in 6, every K_s^0 candidate is assigned a weight which is the reciprocal of the efficiency evaluated at the p_T of the candidate and the CTC charged multiplicity of the event in which the candidate was found. Weights are also assigned to each background track-pair in the same way.

Consider a single bin in p_T. Let a be the sum of the weights for all the pairs in the bin that meet all the geometrical cuts and fall within the K_s^0 mass window; schematically,

$$a \equiv \sum w_{SB},$$

where the subscript SB indicates that the K_s^0 mass window includes some signal and also some background. Let b be the sum of the weights for all pairs that meet all the geometrical cuts but fall within one of the background mass windows:

$$b \equiv \sum w_B.$$

The number of K_s^0 in the bin, corrected for efficiency and for background contamination, is

$$N_{corr} \equiv a - \frac{1}{2}b,$$

where the 1/2 reflects the fact that each of the two background windows is just as wide as the K_s^0 mass window.

The squared error on a is

$$\sigma_a^2 = \sum w_{SB}^2,$$

and the squared error on b is

$$\sigma_b^2 = \sum w_B^2.$$

The squared error on N_{corr} is then

$$\sigma_{N_{corr}}^2 = \sigma_a^2 + \frac{1}{4}\sigma_b^2.$$

To get from N_{corr} to the value of the invariant cross-section for the bin, we need to multiply by a number of constant factors:

$$E\frac{d^3\sigma}{dp^3} = \frac{1}{BR}\frac{\sigma_{eff}}{N_{ev}}\frac{1}{\Delta y}\frac{1}{\Delta\Phi}\frac{1}{p_T dp_T}N_{corr},$$

where BR is the branching ratio for $K_s^0 \rightarrow \pi^+\pi^-$, σ_{eff} is the effective cross-section value we normalize to, N_{ev} is the number of events in the data sample that meet our event-selection requirements, Δy is the rapidity interval to which we restrict ourselves, $\Delta\Phi$ is 2π, p_T is the center of the bin, and dp_T is the bin width. To get the error on the cross-section value, we multiply σ_N by the same constants:

$$\sigma(E\frac{d^3\sigma}{dp^3}) = \frac{1}{BR}\frac{\sigma_{eff}}{N_{ev}}\frac{1}{\Delta y}\frac{1}{\Delta\Phi}\frac{1}{p_T dp_T}\sigma_{N_{corr}}.$$

C.2 Lifetime Plot Corrected via Fixed-Lifetime Simulation Files

C.2.1 The Correction Technique To correct the lifetime distribution, one may simulate samples of K_s^0 whose lifetime is fixed and whose p_T is randomly distributed according to the spectrum we measure; one then fits the efficiency as a function of t/τ and N_{ch}^{CTC}, and assigns a weight separately to each pair in the K_s^0 mass window and to each pair in the background windows. As in the p_T case, the weighted background is subtracted from the weighted signal.

C.2.2 Error Propogation Since the correction technique is essentially similar to the method used for the p_T spectrum, the error propogation proceeds along similar lines. Let a, b, and N_{corr}, be defined as above, where it is understood that the bin we're talking about is now a bin of the t/τ histogram, rather than the p_T histogram. Then the above expressions for σ_a, σ_b, and $\sigma_{N_{corr}}$ still hold. Now, in order to convert N_{corr} into $\Delta N/\Delta(t/\tau)$, we must divide by the bin width, $\Delta(t/\tau)$:

$$\frac{\Delta N}{\Delta(t/\tau)} = \frac{1}{\Delta(t/\tau)} N_{corr},$$

so the error on the above quantity is simply

$$\sigma\left(\frac{\Delta N}{\Delta(t/\tau)}\right) = \frac{1}{\Delta(t/\tau)} \sigma_{N_{corr}}.$$

C.3 Lifetime Plot Corrected via Spectrum Simulation Files

C.3.1 The Correction Technique In another technique for correcting the lifetime plot, we base the corrections on a single large sample of simulated K_s^0 with p_T distributed randomly according to our measured spectrum. After pattern-recognition and cuts have been applied to these simulated K_s^0, the number in each t/τ bin is, apart from a normalization factor, the efficiency for finding K_s^0 that fall in that bin. In this case, we generate 3 UNweighted histograms of t/τ: one for pairs in the K_s^0 mass window, one for pairs in the background windows, and one for the simulated K_s^0. We subtract, bin by bin, the background histogram from the signal-plus-background histogram, and divide the result, bin by bin, by the histogram for the simulated K_s^0.

To see how this method works, consider the following argument. Let N_S be the corrected number of K_s^0 in a given t/τ bin, after background-subtraction. Then

the corrected number of K_s^0 in that bin is

$$N_{corr} \equiv \frac{N_S}{\epsilon},$$

where epsilon is the efficieny for that bin. If N_{sim} is the number of K_s^0 that were simulated that fell in this bin, and N_{fnd} is the number of the simulated K_s^0 in this bin that were found, then

$$\epsilon = \frac{N_{fnd}}{N_{sim}},$$

and

$$N_{corr} = \frac{N_S}{\frac{N_{fnd}}{N_{sim}}} = N_{sim}\frac{N_S}{N_{fnd}}.$$

Now, since the simulated sample was generated according to the correct lifetime distribution, N_{sim} is, apart from statistical fluctuations, simply related to N_{sim}^{TOT}, the number of K_s^0 in the entire simulated sample:

$$N_{sim} = N_{sim}^{TOT} e^{-(t/\tau)},$$

so

$$N_{corr} = N_{sim}^{TOT} e^{-(t/\tau)} \frac{N_S}{N_{fnd}}.$$

Now, if the technique we use to get efficiencies is correct, N_S/N_{fnd} should be the same in all bins, and the corrected lifetime distribution ought to follow an exponential in t/τ. For simplicity, in generating the lifetime plot, we drop the overall normalization N_{sim}^{TOT}.

C.3.2 Error Propogation In this case, we are dealing with unweighted histograms. Again, consider a single bin in the t/τ histogram. Let N_{SB} be the number of real-data V^0's in the bin that meet all geometrical cuts and fall in the

K^0_s mass window; then

$$\sigma^2_{N_{SB}} = N_{SB}.$$

Let N_B be the number of pairs in the bin that meet all geometrical cuts and fall in the background bins; then

$$\sigma^2_{N_B} = N_B.$$

Let N_S be the of K^0_s after background subtraction (but before correction for efficiency); then

$$N_S = N_{SB} - \frac{1}{2}N_B,$$

and

$$\sigma^2_{N_S} = \sigma^2_{N_{SB}} + \frac{1}{4}\sigma^2_{N_B}.$$

Let N_{sim} be the number of simulated K^0_s in the bin that met all cuts. Then the number of K^0_s in the bin, corrected for efficiency and background contamination, is

$$N_{corr} \equiv \frac{N_S}{N_{sim}},$$

and the squared error on N_{corr} is

$$\sigma^2_{N_{corr}} = N^2_{corr}\left(\frac{\sigma^2_{N_S}}{N^2_S} + \frac{\sigma^2_{N_{sim}}}{N^2_{sim}}\right).$$

Again, we must divide by the bin width to convert to $dN/d(t/\tau)$:

$$\frac{\Delta N}{\Delta(t/\tau)} = \frac{1}{\Delta(t/\tau)}N_{corr},$$

so the error on the above quantity is simply

$$\sigma\left(\frac{\Delta N}{\Delta(t/\tau)}\right) = \frac{1}{\Delta(t/\tau)}\sigma_{N_{corr}}.$$

Appendix D: Fitting Algorithms

D.1 The Fit Using Gaussian Errors

In this algorithm, we treat the errors on the cross-section points as if they were Gaussian. The derivation of the errors on the cross-section points is described in Appendix C. However, if we were to compare the invidual cross-section values with the trial function, we'd have to correct the bin centers to account for the fact that the spectrum falls steeply. In order to avoid this, we define our χ^2 in terms N_i^{corr}, the number of corrected K_s^0 in each bin. We compare this number with the number of K_s^0 in the bin predicted from $f(p_T)$, the trial function that's supposed to represent $Ed^3\sigma/d^3p$:

$$N_i^{expected} = \frac{BRN_{ev}\Delta y \Delta\Phi}{\sigma_{eff}} \int_i f(p_T) p_T dp_T,$$

where BR is the branching ratio for $K_s^0 \rightarrow \pi^+\pi^-$, σ_{eff} is the effective cross-section value we normalize to, N_{ev} is the number of events in the data sample that meet our event-selection requirements, Δy is the rapidity interval to which we restrict ourselves, $\Delta\Phi$ is 2π, and the subscript i on the integral is understood to indicate integration over the i^{th} bin.

The χ^2 is then

$$\chi^2 = \sum_i \left[\frac{N_i^{expected} - N_i^{corr}}{\sigma_i^{N_i^{corr}}} \right]^2,$$

where $\sigma_i^{N_{corr}}$ is determined as discussed in Appendix C. As in the other fitting algorithms, we use the MINUIT minimization package [50] to minimize the χ^2.

D.2 The One-Dimensional Poisson Fit

This algorithm is due to Virgil Barnes.

There are a number of compromises that must be faced if one wants to do a fit with a Poisson likelihood function. In the Gaussian fit, we compare N_i^{corr} to the number of K_s^0 expected based on the trial function, but N_i^{corr} is the result of subtracting a weighted background from a weighted signal, so it obviously doesn't fluctuate according to Poisson statistics. The quantities that do fluctuate Poissonianly are N_i^{SB}, the raw, uncorrected number of K_s^0 candidates found in each bin (including both signal and background) and N_i^B, the raw, uncorrected number of pairs in the background windows in a each bin of the p_T distribution.

Because we have no way of defining a Poisson mean for the background, we neglect statistical fluctuations on the background. Also, in order to get to a number that follows Poisson statistics, we must remove the effects of the weighting; this requires averaging somehow over the multiplicity-dependent part of the weighting function. In this algorithm, this averaging is done by dividing the amount of expected signal+background in each bin by the contents of the corresponding bin of the weighted signal+background histogram. The algorithm proceeds as follows:

1. We obtain an average weight (let's call it W_i^{SB}) for each bin by dividing the weighted signal+background histogram by the unweighted version.
2. We integrate the cross-section function over the bin, and multiply by the necessary constants to get the expected number of K_s^0 in that bin. We'll call this number $N_i^{expected}$.
3. We get the number of background events expected in each bin, weighted according to the K_s^0 efficiency function, directly from the weighted background histogram. We'll call this number N_i^{WB}, and in what follows, we'll assume

that the division by 2 (to account for the relative size of the background window) hasn't been done yet.

4. We define a likelihood function which is the following product of probabilities:

$$L = \prod_i P(N_i^{exp} = W_i^{SB} N_i^{SB} - \frac{N_i^{WB}}{2}).$$

We can rewrite this as follows:

$$L = \prod_i P(N_i^{SB} = \frac{(N_i^{exp} + \frac{N_i^{WB}}{2})}{W_i^{SB}}).$$

We then assume that N_i^{SB} fluctuates according to Poisson statistics, with mean

$$\mu_i^{SB} \equiv \frac{(N_i^{exp} + \frac{N_i^{WB}}{2})}{W_i^{SB}},$$

and write a log-likelihood function

$$\mathcal{L} \equiv \ln L = \sum_i \ln \frac{\mu_i^{SB N_i^{SB}} e^{-\mu_i^{SB}}}{N_i^{SB}!}$$

or

$$\mathcal{L} = \sum_i N_i^{SB} \ln \mu_i^{SB} - \mu_i^{SB} - \ln N_i^{SB}!,$$

and we use MINUIT to maximize it (by minimizing its negative).

In order to derive something resembling a χ^2 for this fit, we must multiply the likelihood function by 2, and we must insure that our "χ^2" is 0 when the trial function passes exactly through all the points, so we define our χ^2 as follows:

$$\chi^2 = \mathcal{L} - (\mu_i^{SB} \ln \mu_i^{SB} - \mu_i^{SB} - \ln \mu_i^{SB}!).$$

Since μ_i^{SB} is not necessarily an integer, we replace $\mu_i^{SB}!$ by $\Gamma(\mu_i^{SB} + 1)$.

D.3 The Two-Dimensional Poisson Fit

This algorithm and its description are due to Franco Bedeschi.

This algorithm uses the distribution of K_s^0 candidates in two dimensions: N_{ch}^{CTC}, the CTC multiplicity of the underlying event, and p_T. Rather than getting the weighted background estimate directly from the weighted background histogram, as in the 1-dimensional fit, we fit the background separately from the cross-section fit in order to smooth out statisical fluctuations. In this algorithm, the variation in the efficiency as a function of N_{ch}^{CTC} is taken into account by defining separate efficiency functions $\epsilon_i(p_T)$, for each multiplicity bin, and convoluting them with the trial spectrum function.

First, lest us specify some common notation which will be used in the the rest of this Appendix. Since our measurements are broken into p_T bins and multiplicity bins it is convenient to distinguish them. In the following the subscript a will be used for p_T bins and the subscript i for multiplicity bins.

a. $d\sigma_i/dp_t$ is the differential cross section for a given associated multiplicity i;

b. $d\sigma/dp_t$ is the overall differential cross section;

c. μ_{ai}^{SB} is the expected average content of bin ai of the signal plus background histogram; a similar definition holds for μ_{ai}^{B}.

d. N_{ai}^{SB} is the content of bin ai of the signal plus background histogram; a similar definition holds for N_{ai}^{B}.

e. W_{ai}^{SB} is the average weight of bin ai of the signal plus background histogram; a similar definition holds for W_{ai}^{B}.

f. $\vec{\theta}$ will in general represent a set of unknown parameters to be determined with the fit.

g. In the following whenever referring to histogram contents summed over one index that index will be dropped in the notation (e.g. $\sum_i N_{ai}^{SB} = N_a^{SB}$).

h. The symbol $\int_a f dp_t$ will indicate the integral of f, the trial function for the spectrum, over the a^{th} p_T bin.

i. $\epsilon_i(p_t)$ will indicate the efficiency function for the i^{th} multiplicity bin.

We will assume that our input data are the uncorrected contents of two 2-dimensional histograms: that of signal plus background data and that of background only, as a function of p_T and associated CTC multiplicity. It is worth noting that the contents of the two histograms are totally uncorrelated, since they contain data relative to two different mass windows.

What we intend to do is to fit the differential cross section without making any special assumption about its dependence on the associated CTC track multiplicity. We would also like to do it in a way which is statistically sound. We will start with a simpler example to prove that our first assumption cannot be met, and that however the problem can be reduced to that of finding a suitable averaging scheme. After this is clarified we will show the natural way to do our fit.

D.3.1 Simplest Case Let us assume we have no background and efficiency 100% over the whole range of p_T and multiplicity. Then the only histogram we need is that of the signal, with N_{ai}^{S} as contents. In this case we would know what to do without any problems: we would fit the contents summed over the multiplicity

index, with the following expected averages:

$$\mu_a^S = A\sum_i \int_a \frac{d\sigma_i}{dp_t} dp_t = A\int_a \frac{d\sigma}{dp_t} dp_t$$

We will show that this is formally equivalent to fitting each $d\sigma_i/dp_t$ with the same functional form except for the normalization constant.

D.3.2 Global fit Let $\mu_a^S = A\int_a f(\vec{\theta}, p_t)dp_t$, and $\lambda = -2\log L = 2\sum_a(\mu_a^S - N_a^S \log \mu_a^S)$ be the log-likelihood function, where the factorial terms have been neglected since they affect neither the determination of the parameters nor that of their errors. By simple differentiation we can now determine the equations to be solved for the parameters:

$\partial\lambda/\partial A = 0$ yields:

$$A = \frac{\sum_a N_a^S}{\sum_a \int_a f(\vec{\theta}, p_t)dp_t} \tag{D.1}$$

while $\partial\lambda/\partial\vec{\theta} = 0$ yields:

$$\sum_a \left(\int_a \frac{\partial f}{\partial\vec{\theta}} dp_t\right)\left(A - \frac{N_a^S}{\int_a f dp_t}\right) = 0 \tag{D.2}$$

D.3.3 Fitting both p_T and multiplicity bins According to our previous assumptions about the functional form, we will define $\mu_{ai}^S = A_i\int_a f(\vec{\theta}, p_t)dp_t$ and, just for convenience of notation, $A = \sum_i A_i$. We can now write a similar loglikelihood function to that of the previous case with the sum extended over both p_T and multiplicity bins and calculate the derivatives with respect to the parameters $\vec{\theta}$ and A_i.

$\partial\lambda/\partial A_i = 0$ yields:

$$A_i = \frac{\sum_a N_{ai}^S}{\sum_a \int_a f(\vec{\theta}, p_t)dp_t} \tag{D.3}$$

therefore

$$A = \sum_i A_i = \frac{\sum_a N_a^S}{\sum_a \int_a f(\vec{\theta}, p_t) dp_t} \tag{D.4}$$

which is formally identical to the result obtained in the previous case. Differentiating λ with respect to $\vec{\theta}$ yields too the same equations as in the previous case.

We can therefore state the following conclusion:
fitting the p_T dependence on a 1-D histogram obtained by summing over the multiplicity bins is formally equivalent to fitting the 2-D histogram with the same functional form for each multiplicity bin with a different constant factor for each multiplicity bin. The sum of these constant factors yields the same factor as that obtained in the 1-D fit.

So, even if the differential cross section had a different shape for different multiplicity bins, the above conclusion gives us a prescription on how to average these different shapes in order to obtain the overall p_T dependence from the fit.

D.3.4 Our case We can now apply what we've learned to our case. In the following we list the various steps needed for the fit:

1. A fit to the background is made with any arbitrary function which gives a reasonable χ^2; let it be $g_i(\vec{\alpha_i}, p_t)$ and $\mu_{ai}^B = \int_a g_i(\vec{\alpha_i}, p_t) dp_t$ be our estimate of N_{ai}^B. As in the past the fitting function with the most limited number of parameters will be preferred.

2. A maximum likelihood fit to the signal plus background histogram is made with the following expectation value for N_{ai}^{SB}:

$$\mu_{ai}^{SB} = \int_a \left(A_i f(\vec{\theta}, p_t) \epsilon_i(p_t) + \frac{1}{2} g_i(\vec{\alpha_i}, p_t) \right) dp_t$$

3. A global maximum likelihood fit to both histograms can then be performed after suitable starting points have been determined from steps 1. and 2.

Appendix E: Calculating K/π and the Strangeness-Suppression Factor

E.1 The K/π Ratio

The "K/π ratio" quoted above is the ratio

$$\frac{K^0_s}{\frac{(\pi^+ + \pi^-)}{2}},$$

where K^0_s stands for $\rho(0)$ for K^0_s and $\pi^\pm$ stands for $\rho(0)$ for $\pi^\pm$. Since CDF has not directly measured $\rho(0)$ for pions, we must calculate it from quantities that we have measured. We start from the CDF estimate [14] of $dN/d\eta$ for charged hadrons: $dN/d\eta = 4.19 \pm 0.09$ at 1800 GeV and $dN/d\eta = 3.2 \pm 0.3$ at 630 GeV. For simplicity, in what follows, we will use $dN_h/d\eta$ to represent HALF of $dN_{ch}/d\eta$; that is, $dN_h/d\eta$ is the pseudo-rapidity density for $(h^+ + h^-)/2$.

Charged hadrons consist primarily of pions, kaons and protons:

$$\frac{dN_h}{d\eta} = \frac{dN_\pi}{d\eta} + \frac{dN_K}{d\eta} + \frac{dN_p}{d\eta}.$$

The number we want to calculate is dN_π/dy, not $dN_\pi/d\eta$, so we must figure out how to convert one to the other. Let us define the ratio

$$a_\pi \equiv \frac{\frac{dN_\pi}{d\eta}}{\frac{dN_\pi}{dy}},$$

and a_K and a_p similarly. Then

$$\frac{dN_h}{d\eta} = a_\pi \frac{dN_\pi}{dy} + a_K \frac{dN_K}{dy} + a_p \frac{dN_p}{dy}.$$

We may assume that $(K^+ + K^-)/2$ is the same as K^0_s. We don't know what fraction of charged hadrons are protons and anti-protons, but we can guess (as do UA5 [22], based on UA2 particle-ID data [19]) that the K/p ratio is 1.48. Changing

this number over a reasonable range will affect the K/π result little, since protons form only a few percent of the charged hadrons. With these assumptions, we may write

$$\frac{dN_h}{d\eta} = a_\pi \frac{dN_\pi}{dy} + a_K \frac{dN_{K^0_s}}{dy} + a_p \frac{1}{1.48} \frac{dN_{K^0_s}}{dy},$$

or

$$\frac{dN_\pi}{dy} = \frac{1}{a_\pi} \left[\frac{dN_h}{d\eta} - a_K \frac{dN_{K^0_s}}{dy} - a_p \frac{1}{1.48} \frac{dN_{K^0_s}}{dy} \right].$$

Plugging this result into our expression for the K/π ratio, we find

$$\frac{K}{\pi} = \frac{a_\pi \frac{dN_{K^0_s}}{dy}}{\frac{dN_h}{d\eta} - \frac{dN_{K^0_s}}{dy} \left(a_K + a_p \frac{1}{1.48} \right)}.$$

To get $dN_{K^0_s}/dy$, we use the m_T extrapolation with transition at 0.4 GeV. We get $dN_h/d\eta$ from numbers published in [14] for $dN_{ch}/d\eta$ at 630 GeV and the ratio of $dN_{ch}/d\eta$ at 1800 GeV to that at 630 GeV.

Now we must calculate a_π, a_K, and a_p. Each of these numbers depends on the spectrum of the particles and the rapidity interval of interest, which is $|y| < 1$. Note that the difference between y and η is most pronounced in the low-momentum part of the spectrum. We'll assume that all the particle spectra follow an exponential in transverse mass below $p_T = 0.4$ GeV. We will assume that shape of the pion spectrum is the same as that for charged hadrons, that the shape of the charged kaon spectum is the same as that for K^0_s, and that the shape of the proton spectrum is the same as that for K^0_s. The assumption about the proton spectrum probably isn't right, but again, the proton contribution is small enough that a ballpark number for the correction is sufficient. In fact, varying the K/p ratio between 1 and 2 changes the K/π ratio estimate by 0.03 and the strangeness-suppression factor

by 0.01. Given the spectra, we use a small Monte-Carlo program to determine a_π, a_K and a_p. The program generates pions according to their assumed p_T spectrum and flat in y, calculates the y value for each pion, and finally calculates the ratio between the number of pions that fall within η of ± 1 and the number of pions that we generated in $|y| < 1$. The same calculation is also done for kaons and protons.

E.2 The Strangeness-Suppression Factor

The strangeness-suppression factor λ represents the ratio of the probability of producing a strange quark from the vacuum to that of producing an up or down quark from the vacuum. We have used two models to calculate λ; in the tables above, λ_1 indicates the value from the model of Anisovich and Kobrinsky [27], while λ_2 indicates the value from the model of Shekhter and Shchlegova [28].

E.2.1 The Model of Anisovich and Kobrinsky In [27], Anisovich and Kobrinsky give formulas in terms of λ for relative probabilities for production of various hadrons in the central region. They use a statistical quark model, and their calculations include the effects of resonance production and decay. In this model, the relative probability of producing π^+ or π^- is

$$31 + 12\lambda + 3\lambda^2 + \gamma(\frac{16}{3} + 4\lambda + \frac{8}{3}\lambda^2),$$

where

$$\gamma \equiv \frac{4 + 4\lambda + \lambda^2}{5 + 5\lambda + 3\lambda^2 + \lambda^3},$$

while the relative probability of producing K^0 or $\overline{K^0}$ is

$$12\lambda + 3\lambda^2.$$

Thus, we can set

$$\frac{K^0 + \overline{K}^0}{\pi + \pi -}$$

equal to the ratio of the above expressions for the relative production probabilities, and solve the equation for λ. The resulting equation is quite complicated, so we solve it numerically. The error on λ may be readily calculated from the error on K/π.

The model also predicts the relative probability for producing Λ or $\bar{\Lambda}$, which is $8\lambda\gamma$. Using this expression and the relative probability for producing K^0 or $\overline{K}^0$ above, we can in principle calculate λ from our measured Λ/K ratio. However, since both the Λ and the K_s^0 contain a strange quark, the model's prediction of this ratio is only weakly dependent on λ, and the dependence comes entirely from the contribution of resonances to the production of Λ and K_s^0. Thus, this ratio does not provide a very sensitive way to determine λ.

On the other hand, the ratio $(\Lambda + \bar{\Lambda})/(h^+ + h^-)$ is more sensitive to the value of λ, since the denominator is dominated by pions, which of course are not strange. As noted above, in the model, the relative probability for producing Λ is $8\lambda\gamma$. We will treat the relative probability of producing charged hadrons as the sum of the probabilities for producing charged pions, charged kaons, and protons. This sum is:

$$31 + 12\lambda + 3\lambda^2 + \gamma(\frac{16}{3} + 4\lambda + \frac{8}{3}\lambda^2) + 12\lambda + 4\lambda^2 + 5\gamma.$$

E.2.2 The Model of Shekhter and Shchlegova In [28], Shekhter and Shchlegova use a somewhat more sophisticated statistical quark model than that of Anisovich and Kobrinsky. In particular, their model includes a parameter α which is the

ratio of production of S-wave and P-wave $q\bar{q}$ meson states. They recommend using the value $\alpha = 0.13$, based on the experimental numbers of the day, and that is the value that we use to compute the numbers for λ_2 shown in the tables.

In this model, the relative probability of producing π^+ is

$$9.8 + 4\lambda + 0.7\lambda^2 + (47.3 + 27.4\lambda + 2.7\lambda^2)\alpha,$$

while the relative probability of producing K^0 is

$$\lambda(4 + \lambda) + (0.4 + 12\lambda + 5.5\lambda^2)\alpha.$$

Again, given our value of the K/π ratio, we can solve numericaly for λ.

Unfortunately, the model does not include formulas for baryon production, so we cannot calculate λ from our $(\Lambda + \bar{\Lambda})/(h^+ + h^-)$ or Λ/K ratios.

VITA

VITA

Martin Henry Schub [redacted] received a Bachelor of Science degree in Engineering Physics from the University of Illinois at Urbana-Champaign in 1984. He was a Teaching Assistant at Purdue University from Jan. 1984 through May 1985, and a Research Assistant in high-energy physics at Purdue from June 1985 through August 1989. He received a Ph.D. in Physics from Purdue in August 1989, with a thesis titled, "Strange Particle Production in Proton-Antiproton Collisions at Center-of-Mass Energies of 630 GeV and 1800 GeV", under faculty advisor Virgil Barnes.